EUROPEAN COMMISSION
Community Research

TIMODAZ

Thermal Impact on the Damaged Zone Around a Radioactive Waste Disposal in Clay Host Rocks

(Contract Number : FI6W-CT-2007-036449)

Deliverable D13 – Annex 4
In situ heating test ATLAS in Mol

Editor(s): **Robert Charlier**

Authors : Suzanne Chalindar, Robert Charlier, Frédéric Collin, Arnaud Dizier, Bertrand François, Jan Fokkens, Benoît Garitte, Antonio Gens, Chen Guangjing, Jaap Hart, Lyesse Laloui, Xavier Sillen

Laboratories: CIMNE, ESV EURIDICE GIE, EPFL, ULg, NRG

Reporting period: **01/10/2009 - 31/03/2010**

Date of issue of this report: **30/08/2010**

Start date of project: **01/10/2006** Duration : **48** Months

Project co-funded by the European Commission under the Euratom Research and Training Programme on Nuclear Energy within the Sixth Framework Programme (2002-2006)		
Dissemination Level		
PU	Public	PU
RE	restricted to a group specified by the partners of the TIMODAZ project	
CO	confidential, only for partners of the TIMODAZ project	CO

DISTRIBUTION LIST

Name	Number of copies	Comments
Mr. Christophe Davies (European Commission)	One electronic copy on CIRCA One paper copy	
All consortium members	One electronic copy available on the restricted area of the TIMODAZ web portal	

1 Introduction

The aim of this benchmark exercise is the modelling of a small scale in-situ experiment ATLAS (Admissible Thermal Loading for Argillaceous Storage). The goal of this experiment is to better understand and quantify the thermal impact on the thermo-hydro-mechanical (THM) behaviour and the sealing capacity of clays. This benchmark concerns the modelling of the third phase of this experiment.

The ATLAS experiment consists of a small scale in-situ heater test realised in the underground laboratory HADES of Mol. This experiment has been developed, by SCK-CEN as part of the Interclay II benchmark exercise launched by the EC in the early 1990s, to allow the comparison between field measurements and blind predictions. In the scope of the TIMODAZ project, the heaters have been re-activated, between April 2007 and April 2008, to have better assessment of the THM characteristics of Boom Clay. This part of the experiment is called ATLAS III and will be modelled within this benchmark.

The main idea of this benchmark is to reproduce the heating and the cooling phase of the ATLAS III experiment with a coupled thermo-hydro-mechanical model. This modelling may be considered as a one-dimensional problem or a two-dimensional problem in axisymmetric condition or a three dimensional problem. This last geometry allows taking into account the effect of the anisotropy of the clay. This report content is the following: after an executive summary, the ATLAS experiment is described. Then the benchmark exercise is presented. The general form of the numerical results is exposed based the results obtained by ULg because a general agreement is obtained with the different teams. The comparison with the different partners of this benchmark (EPFL, EURIDICE, NRG and UPC) is finally presented.

2 Executive summary

2.1 Introduction

Within the TIMODAZ project, a small-scale in situ test named ATLAS III has been performed in order (1) to obtain a more accurate and extended field of the temperature and pore water pressure by recently drilling two additional boreholes equipped with more sensors, which enables to check the possible thermal anisotropy. (2) To test a new data acquisition system which has a higher data acquisition rate and is fully automatic instead of a low-rate and manual data acquisition system used in ATLAS I and II. (3) To have better assessment of THM characterisation of Boom clay at larger scale and at different temperature levels. (4) To serve as preparation for Praclay Heater Test, which is a large scale heater test in Boom clay intending to simulate a disposal gallery at real scale, and to provide a good link with Praclay heater test by up-scaling. (5) To provide data for a modeling benchmark in the European project TIMODAZ (2006~2010).

Withing the work package WP5.2, it has been decided to perform a modelling benchmark based on this in situ test. In a first step, the benchmark has been defined as a blind prediction test with three different geometries, enabling the participating teams to consider different levels of complexity. A one-dimensional axisymmetric model is easy to handle and gives first insights of the relevant physical phenomena. A 2D axisymmetric geometry helps to reproduce better the experiment, in the radial direction and the axial as well. Finally, as far as anisotropy was suspected to play an important role, a fully 3D model has been also proposed for the benchmark exercise. Of course, all the teams were let free to select the geometry they want to deal with for this benchmark.

In a second step, in addition to the benchmark exercise, series of additional computations have been carried out in order to study some more specific features of behaviour that have been underlined during the experiment. Those simulations consist, for most of them, in an analysis and a constitutive interpretation of in situ results in order to validate and calibrate the used numerical models and materials parameters. For this step of the work, the liberty was given to use the constitutive models, the geometry of the mesh and the boundary conditions that each team considers as the most appropriate regarding to the features of behaviour that they expected to observe.

This executive summary presents the main concepts and results that have been obtained in the framework of the numerical modelling of the ATLAS III in situ test. It is divided in three parts: the in situ test brief description, the benchmark exercise and the additional computations.

2.2 Test setup and field data

The original set-up was developed in 1992 by SCK-CEN within the framework of the European project Interclay II (1990~1994). The test was re-activated from June 1996 to May 1997 (ATLAS II). In 2006, the set-up has been refurbished; the heater was activated from April 2007 to April 2008. This was thus the third life of ATLAS test and therefore named ATLAS III.
One of the objectives of ATLAS III test is to provide data for a modelling benchmark in the European project TIMODAZ (2006-2010); that’s why it is now briefly described.

Test set-up

The test setup is composed of a central borehole with heater and of four boreholes with instrumentation. To obtain measurement over a larger range in ATLAS III than that in ATLAS I and ATLAS II, to test the piezometer design and installation envisaged for Praclay gallery, to serve as a far field piezometer for the future large scale Praclay Heater Test, and to get a better picture of the possible thermal anisotropy, the two additional boreholes AT97E and AT98E have been drilled. The main borehole (AT89E) with heater and three other boreholes (AT85E, AT93E, and AT98E) are in the same horizontal plane while a last borehole (AT97E) is slightly inclined towards the heater borehole. The inclination is about 10° down and 10° towards the heater borehole. Figure 1 illustrates the layout of the ATLAS III test.

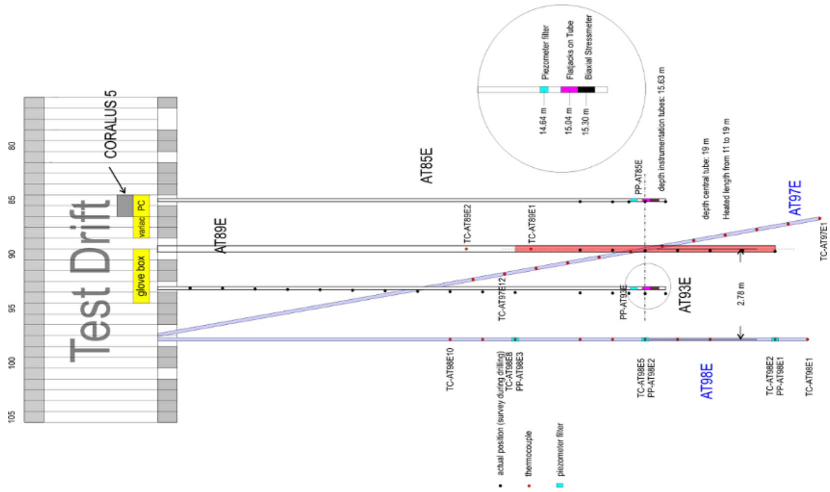

Figure 1: Layout and instrumentation of ATLAS III in situ test

The heater has been re-activated on April 2, 2007 starting with a relatively low heating power of 400 W, the power has been increased step wisely to 900 W then to 1400 W and was finally shut off instantaneously on April 17, 2008 to observe the effects of the cooling transient. Until Nov. 2, 2009, ATLAS III test has lasted for 945 days, with heating for 381 days and cooling for 564 days.

Field data

ATLAS III test yielded a large amount of good-quality data on the thermal, hydraulic and mechanical perturbations. Some interesting phenomena are revealed by the measurements of temperature, pore water pressure and total stress.

Measured temperature

As indicated in Figure 1, there is one temperature sensor in AT85E, one temperature sensor in AT93E, twelve temperature sensors in AT97E, and ten temperature sensors in AT98E. The measured temperature are displayed in Figure 2, where the vertical dashed lines indicate the times of increasing power or shutting down the power. The experimental measurements of temperature can be summarized as follows. First, the temperature increase is inversely proportional to the distance from the heater (Figure 2): the shorter the distance is, the larger the increase of temperature is. Secondly, the successive heating steps are well visible at all the sensors (Figure 2). Thirdly, all measured temperatures by sensors show a delay of the temperature decrease after switching off the heater. This delay is proportional to the distance from the heater.

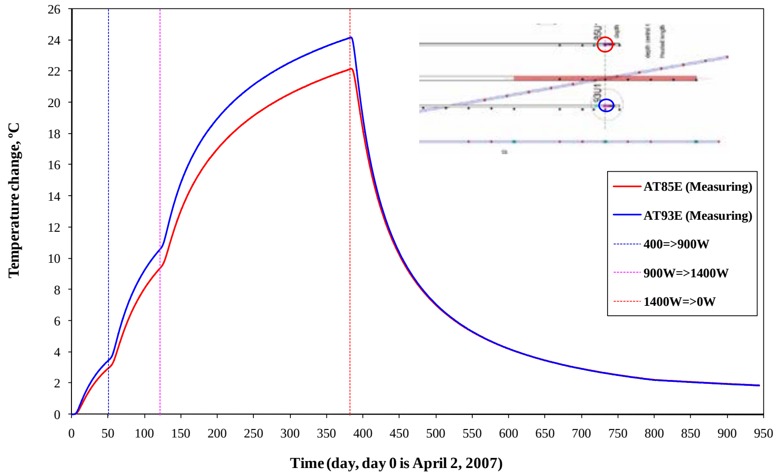

Figure 2: Temperature increase of sensors located in boreholes AT85E and AT93E

Measured pore water pressure

Figure 3 shows the evolution of the pore water pressure. The maximum pore water pressures increase ranges between 0.5 MPa and 1.0MPa. At the end of March 2008, the sudden drop of pore pressure is imposed on the piezometer PP-AT85E in order to determine the permeability of the massif near this sensor. It is interesting to observe that at the start of each heating phase, a temporary decrease of the pore pressure occurs in all the piezometers. The opposite phenomenon is observed when switching off the heater. The pore water pressures are now tending to recover slowly to their initial states before heating.

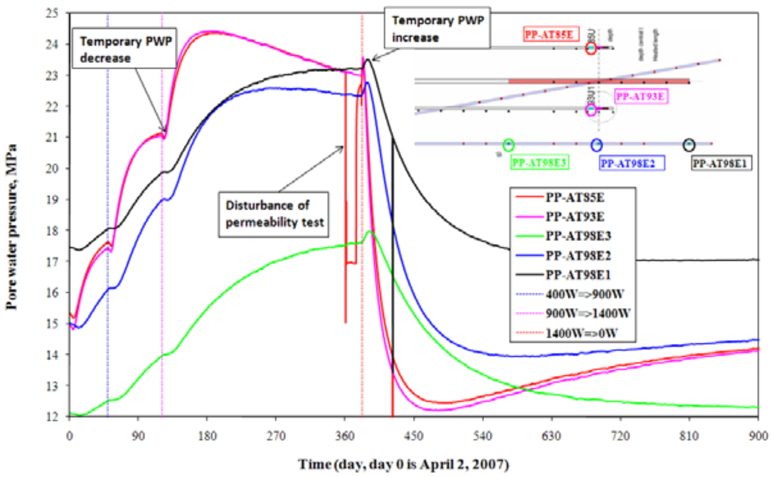

Figure 3: Evolution of pore water pressures in five sensors located in boreholes AT85E, AT93E and AT98E

Measured total stress

From the temporal evolution of the total stress measured by flatjacks, it can be observed that the total stresses present variations with the different sensors orientations for both AT85E and AT93E; besides, the temporary decrease of total stress at the start of each heating phase and temporary increase of total stress at the start of cooling phase are also noticed.

2.3 Benchmark exercise

Problem definition

The benchmark exercise consists in the reproduction of the heating and the cooling phases. Figure 4 presents the geometry of the experiment used for the modelling.

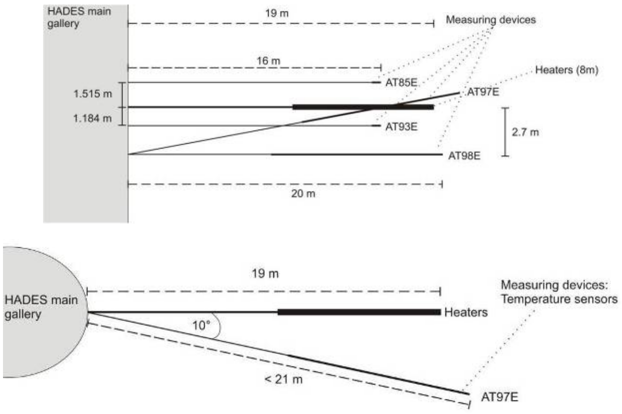

Figure 4: Geometry of ATLAS III. View in a horizontal plane and in a vertical plane

The experimental procedure consists in a thermal loading applied at the heater borehole. The thermal loading is composed of three steps. The first one rises the power from 0 to 400 W in four days and a period of 45 days of stabilisation is allowed. The second one enhances the power from 400 W to 900 W in five days and a period of 66 days of stabilisation is allowed. Finally, the third one, the power is increased up to 1400 W in five days and a period of 256 days of stabilisation is allowed. Then, the power is shut off instantaneously and a cooling phase goes on 69 days. At the difference to the experiment, the modelling stops after 450 days. Indeed, all the cooling phase is not modelled because the benchmark exercise was launched in January 2009 and the experiment ends in November 2009. As a consequence, only 69 days of the cooling cycle have been considered in this exercise. Of course, all the heating phases are considered.

The clay is initially considered as homogeneous. It is supposed to be fully saturated. Initial conditions are listed in Table 1. For Boom Clay, they are close to the ones encountered in the clay formation. The gravity will not be considered in the modelling. These initial conditions are the same for the three geometries used for the computations.

Initial state		Boom Clay
Total stresses [MPa]	$\sigma_x=\sigma_y=\sigma_z$	4.5
Pore pressure [MPa]	p_{w0}	2.25
Temperature [°C]	T_0	16.5

Table 1: Initial state – stresses, pore water pressure and temperature

The three proposed geometries correspond to an idealization of the ATLAS III experiment with an increasing complexity. The first model is a 1D axisymmetric model, which is the easiest model to realise. This model rapidly permits to have an overview of the physics implied in this modelling. The problem is of course not only a one-dimensional (radial) experiment and a 2D axisymmetric model is also proposed in order to quantify the effects (THM) of the heating in the axial direction. Finally, a 3D model is also proposed to evidence the impact of some anisotropy in the constitutive models.

Geometry

Figure 5 and Figure 6 present the geometry for one-dimensional problem (radial-axisymmetric) and the 2D axisymmetric and 3D model respectively. The inner and the external radius are respectively equal to 0.095 m and 100 m. For the 2D and 3D modelling, the height of the model is 119 m. The inner radius corresponds to the radius of the borehole equipped with heaters.

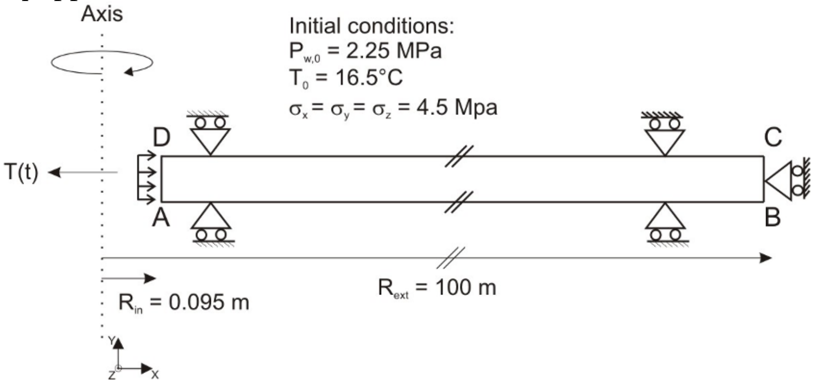

Figure 5: Illustration of the geometry of the 1D modelling

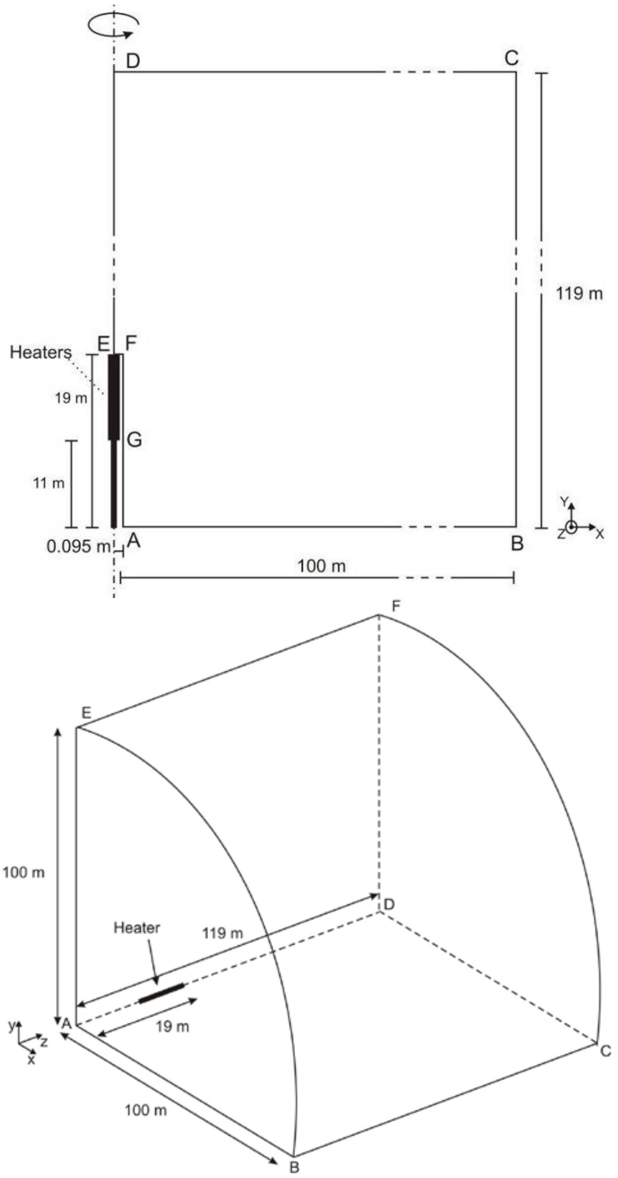

Figure 6: Schematic representation of the 2D axisymmetric and 3D modelling

Boundary conditions

We present in the following the boundary conditions used in this 2D modelling. The 1D axisymmetric and the 3D boundary conditions derive directly from the ones depicted in the following.

Mechanical boundary conditions are defined as followed: (1) Axial displacements are fixed on the external boundaries DC, AB and EF. (2) Radial displacements are fixed on the boundaries ED, BC and AF.

Hydraulic boundary conditions: (1) Pore water pressure are fixed on the boundaries DC, CB. (2) Boundary from the point A to point D is impervious. The boundary AB is also impervious.

Thermal boundary conditions: (1) Boundaries AB, BC, CD, DE and FA are adiabatic. (2) Heat flux is imposed on boundary FG.

Mechanical model

In this benchmark, the mechanical properties of Boom clay may be considered as isotropic or anisotropic. Indeed, the structure of clay in band layers (Mertens et al., 2003) permit to consider this material as transversely isotropic. Only elastic model have been considered in this modelling because the size of the EDZ is relatively small (as the borehole diameter is small) compare to the extent of host rock affected by the thermal process. That is the reason why the excavation of the borehole has not been considered: no EDZ has been created and a thermo-elastic modelling seems sufficient to reproduce the effect of the temperature far away from the heater. For both mechanical model, the total strain rate $\dot{\varepsilon}_{ij}$ is considered as the sum of the mechanical elastic strain rate $\dot{\varepsilon}_{ij}^{m,e}$ and the thermal elastic strain rate $\dot{\varepsilon}_{ij}^{e,th}$:

Linear isotropic elasticity

The first mechanical model considers only an isotropic elastic law, which can be summarised by the following equation:

$$\dot{\sigma}_{ij} = C_{ijkl}^{e}\dot{\varepsilon}_{kl}^{m,e} \tag{2.1}$$

with two elastic parameters, E is the Young's modulus and υ the Poisson's ratio.

Linear transversely isotropic elasticity

The second proposed mechanical model still considers an elastic model but, in this case, the Hooke's law defines a transversely isotropic elastic medium. The behaviour of a transversely isotropic material may be described by five independent parameters (Love, 1944). The required material parameters are two Young' modulus (E_v and E_h), two Poisson's ratio (ν_{vh} and ν_{hh}) and a shear modulus (G_{vh}). The subscripts v and h will be used for stiffness parameters to indicate vertical and horizontal directions respectively. Poisson's ratio for strain in the vertical direction due to a horizontal direct stress is ν_{vh}. Poisson's ratio for strain in any horizontal direction due to a horizontal direct stress at right angles is ν_{hh}. The remaining parameters are not independent.

Hydraulic and thermal constitutive models

Darcy's Law

The general Darcy flow law is used and defines the Darcy fluid velocity $\underline{q}_w$ as a linear function of permeability and the gradient of fluid pressure p_w:

$$\underline{q}_w = -\frac{\underline{\underline{k}}_w}{\rho_w . g}\left(\underline{\nabla} p_w\right) \tag{2.2}$$

where $\underline{\underline{K}}_w$ is the anisotropic tensor of permeability. This tensor has nine components and may be written in a general form as follows:

$$\underline{\underline{k}}_w = \begin{bmatrix} k_{xx} & k_{xy} & k_{xz} \\ k_{yx} & k_{yy} & k_{yz} \\ k_{zx} & k_{zy} & k_{zz} \end{bmatrix} \tag{2.3}$$

If the medium is supposed to be isotropic, the relation becomes:

$$\underline{q}_w = -\frac{k_{\text{int}}}{\mu_w}(\underline{\nabla} p_w) \tag{2.4}$$

where k_{int} is a scalar in isotropic situation [m²] .

Fourier's Law

The general Fourier's law is used to describe the conduction of heat in the medium. This law is expressed by:

$$\underline{i}_{cond} = -\underline{\underline{\lambda}}_m . \underline{\nabla} T \tag{2.5}$$

Where $\underline{\underline{\lambda}}_{\text{m}}$ is the anisotropic tensor of the conductivity of the medium. In a general form, this tensor has 9 components and is written:

$$\underline{\underline{\lambda}}_m = \begin{bmatrix} \lambda_{xx} & \lambda_{xy} & \lambda_{xz} \\ \lambda_{yx} & \lambda_{yy} & \lambda_{yz} \\ \lambda_{zx} & \lambda_{zy} & \lambda_{zz} \end{bmatrix} \tag{2.6}$$

In the same way as the Darcy' law, the Fourier' law for an isotropic material is:

$$\underline{i}_{cond} = -\lambda_m . \underline{\nabla} T \tag{2.7}$$

Liquid dynamic viscosity (μ_w [Pa.s])

$$\mu_w(T) = \mu_{w0} - \alpha_w . \mu_{w0} .(T - T_0) \tag{2.8}$$

where α_w is the liquid dynamic viscosity thermal coefficient [K^{-1}], T_0 is a reference temperature and μ_{w0} is liquid dynamic viscosity at reference temperature.

Water density (ρ_w)

$$\rho_w(T, p_w) = \rho_{w0} . \left[1 + \frac{p_w - p_{w0}}{\chi_w} - \beta_w .(T - T_0) \right] \tag{2.9}$$

where β_w is the liquid volumetric thermal expansion coefficient [K^{-1}], $1/\chi_w$ is the liquid compressibility coefficient [MPa^{-1}], ρ_{w0} is the density at reference temperature and p_{w0} is a reference pore pressure.

1D RESULTS

Figure 7 represents the evolution of the pore water pressure and the temperature with time. The power of the heater is increased in 3 steps. After each increase, the power is maintained constant. Figure 7 shows that a maximum of 100 °C at the inner radius is attained at the end of the third heating phase. Finally, when the heater is switched off, the temperature quickly decreases. The evolution of the pore water pressure is related to the thermal dilation of water, which is more important than the dilation of the solid. When the power is maintained constant, the pore water pressure is quiet stabilised. Finally, a decrease of pore pressure is observed during the cooling phase.

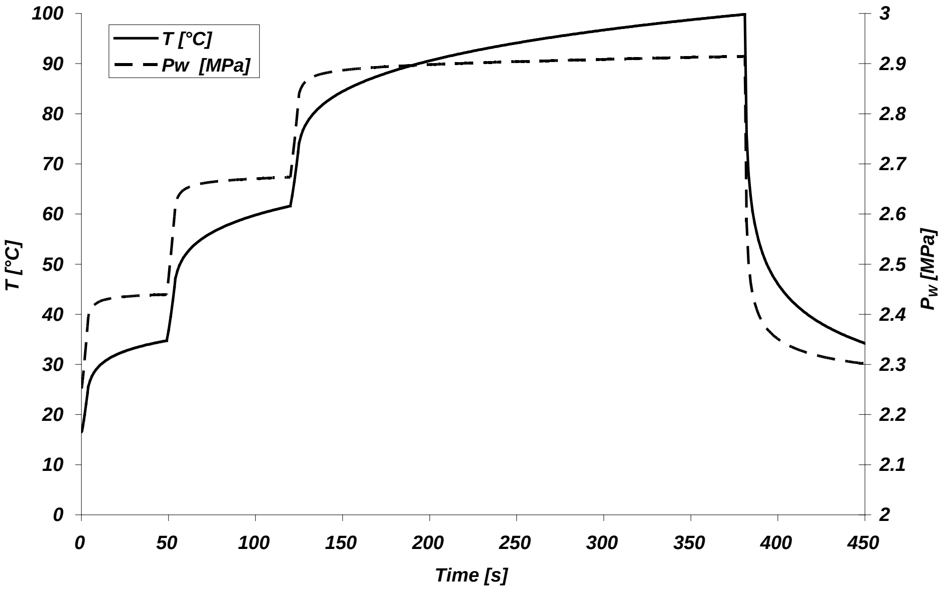

Figure 7: Evolution of the temperature and the pore water pressure at the inner cavity

The heat generated by the increase of the power dissipates into the medium. As a consequence, the temperature increases around the heater during the three phases of heating. The thermally affected zone grows with time due to the dissipation of the heat. When the power is switched off, the temperature near the cavity decreases but dissipation of the heat goes on and the temperature continues to increase in the far field.

The evolution of the pore water pressure with the radial distance is described in Figure 8, which shows the pore water pressure increases around the heater during the heating phase (profiles at 4, 54, 125 and 250 days). On the contrary, the reduction of the temperature induces a decrease of the pore pressure near the heater (profile at 450 days). But due to the dissipation of the heat, during the cooling phase, the pore water pressure continues to increase in the far field.

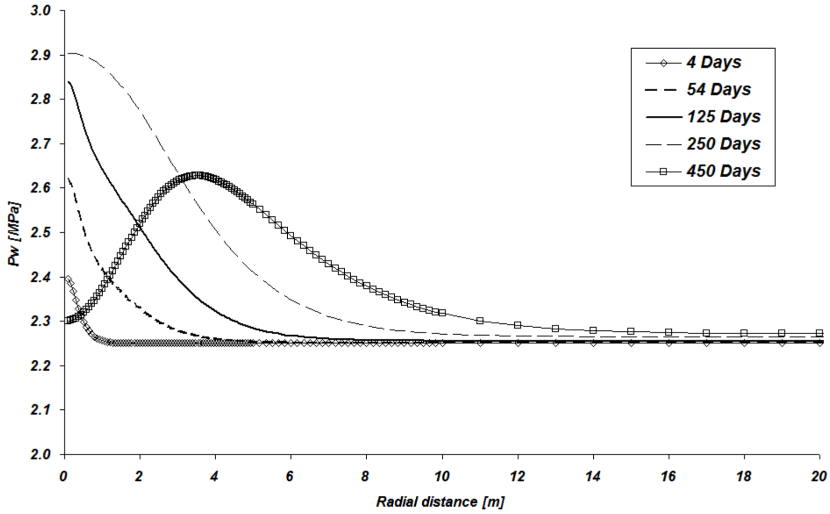

Figure 8: Evolution of the radial profiles of pore water pressure for various times

2D RESULTS

The radial distribution of the temperature leads to the same conclusion as previously in 1D modelling. The increasing power induces an increase of the temperature, whereas a decrease is observed during the cooling phase when the heater is switched off. However, at the difference to the 1D modelling, the dissipation of the heat in the 2D model can occur in 2 directions, whereas this dissipation concerns only one direction in 1D modelling. That is the reason why the maximum temperature at the inner radius is lower in the 2D modelling.

The evolution of the pore water pressure is analogous to the results obtained in the 1D modelling. But, on the contrary of the 1D case, the pore water pressure reaches a value lower than the initial value at the end of the modelling. This effect is related with the drainage, which has two components in 2D. Actually, the drainage can be axial or radial unlike in the 1D where the component of the drainage is radial.

3D RESULTS

This section presents the results obtained with the 3D modelling considering mechanical, hydraulical and thermal anisotropies.

Figure 9 presents the spatial distribution of the temperature at different times for the profile 1 and the profile 4. Due to the difference of thermal conduction, the temperature is greater in the far field for the profile 4 as compared to profile 1.

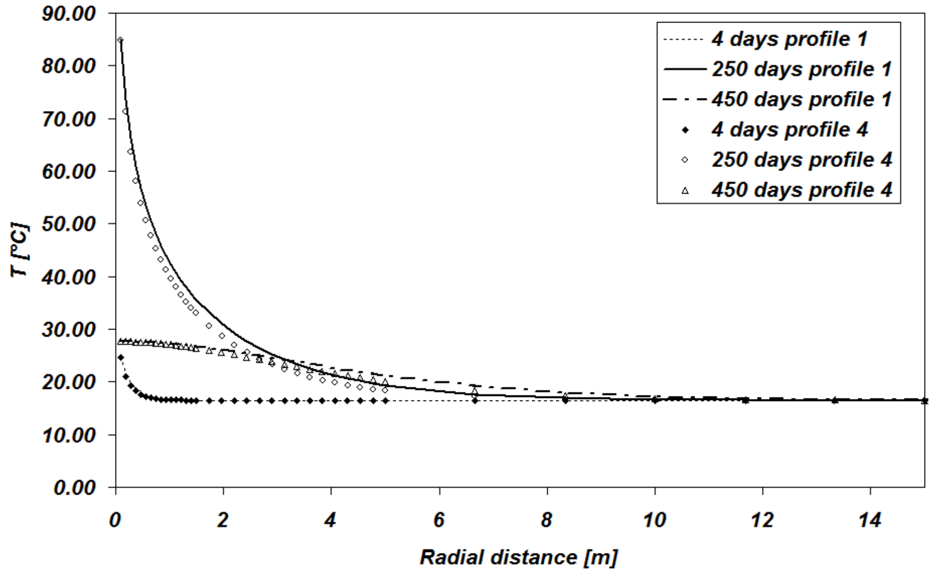

Figure 9: Distribution of the temperature according profile 1 and profile 4

As compared to isotropic case, the effect of all this anisotropy is to generate higher pore water pressures. Figure 10 shows the difference obtained for the pore water pressure evolution at AT85E between this anisotropic case and the isotropic case.

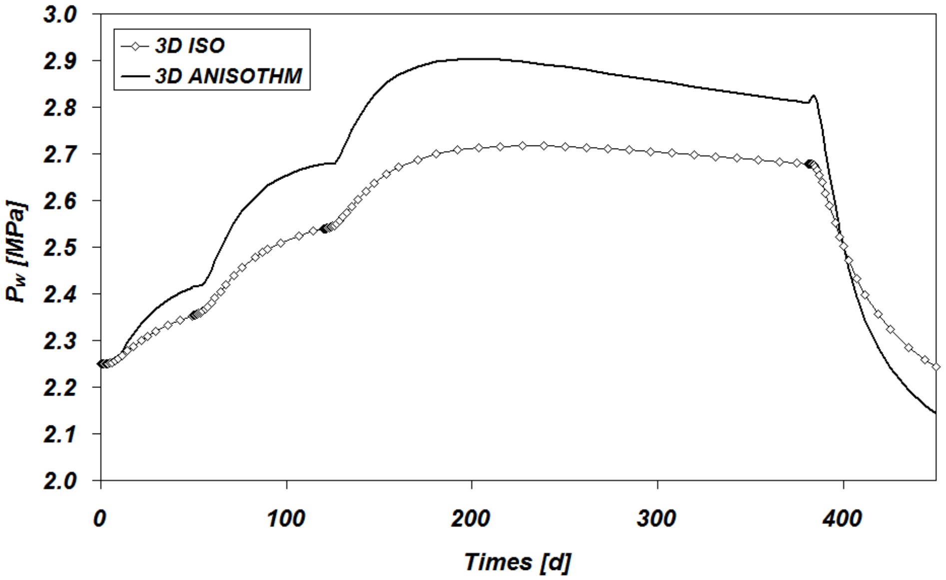

Figure 10: Evolution of the pore water pressure in the full anisotropic model and in the isotropic model at AT85E

COMPARISON WITH EXPERIMENTAL RESULTS

This section presents some comparisons between experimental and predicted data. Figure 11 presents a comparison of the temperature changes for the 1D and the 2D calculations. We show that the temperature increase is quite similar between the 2D and the experimental results.

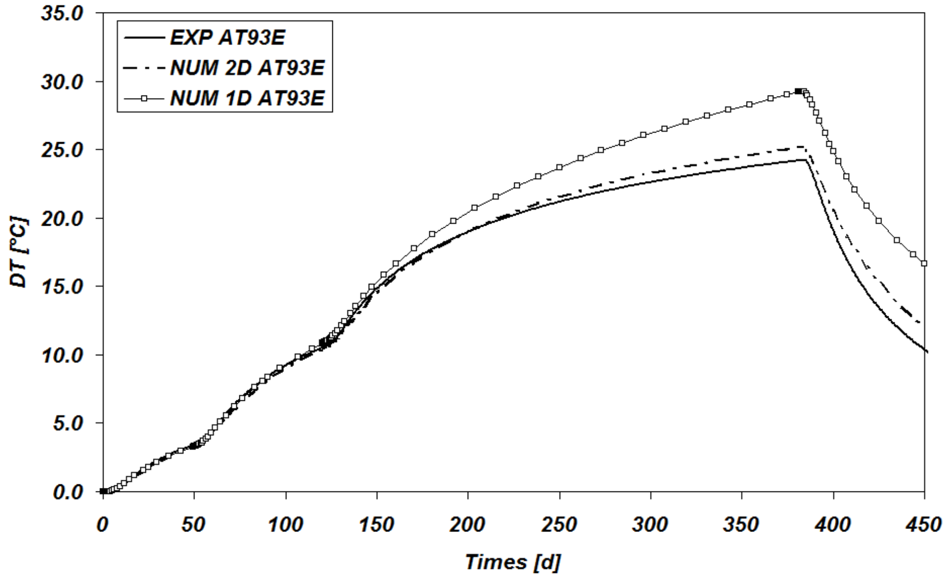

Figure 11: Comparison between the experimental results and the numerical results for the sensor located in the boreholes AT93E

In 2D modelling, the comparisons between the temperature evolution recorded and the numerical results show good agreement for some sensors in the horizontal plane. Figure 12 presents a comparison between the temperature recorded and the numerical results for some sensors of AT97E. This borehole is inclined compared with the horizontal plane. The result of this comparison shows that all the numerical results do not fit the experimental curves.

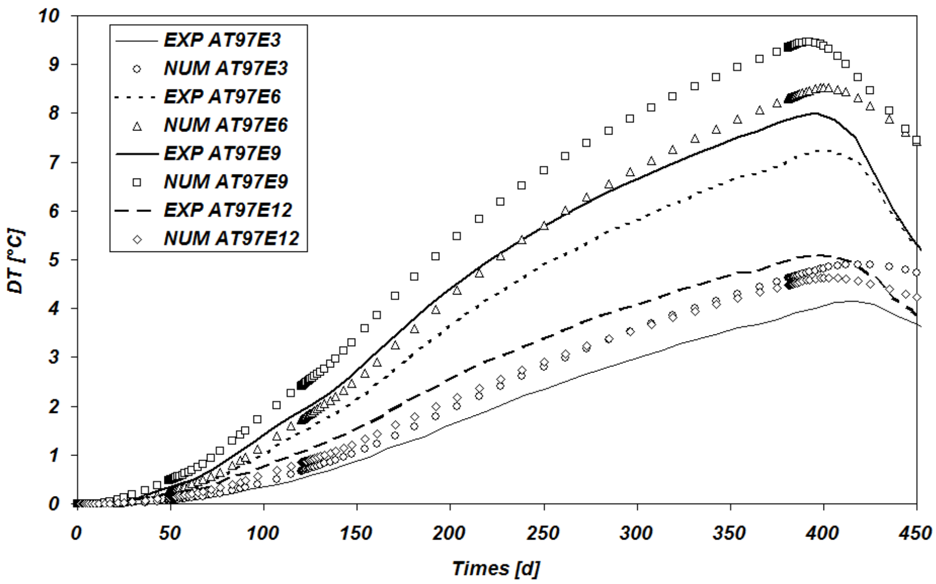

Figure 12: Comparison between experimental results and numerical results for sensors in the borehole AT97E

The evolution of the pore water pressure is different between modelling and experiment. Figure 13 presents the comparison between the experiment and the modelling. In both case, we see that the evolution of the pore pressure is underestimated.

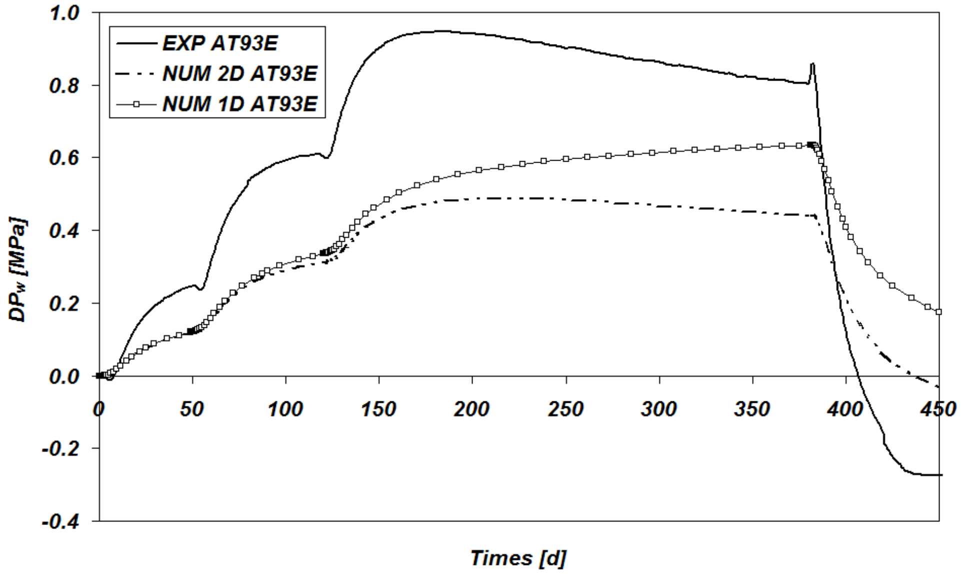

Figure 13: Comparison of the evolution of the incremental pore water pressure between experimental and numerical results

In 3D modelling, a comparison between the evolutions of the temperature for the different sensors has been realised. Figure 14 presents a comparison between the experimental data and the numerical results for the sensor AT97E. We can observe that the comparison between experimental and numerical results is quiet good for these sensors. The anisotropic parameters of the thermal conductivity permits to better reproduce the observed evolution as compared with the isotropic case. For the sensors of AT98E, the 3D numerical results are good except for AT98E10 and AT98E5. This means that some improvements have to be done in the calibration of the thermal parameters.

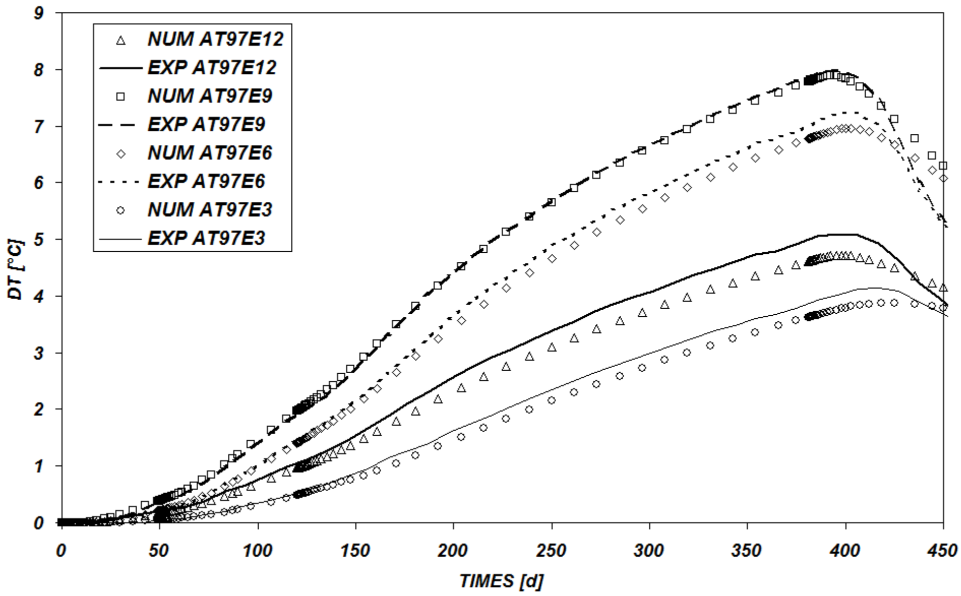

Figure 14: Comparison between the experimental and the numerical data for some sensors of AT97E

Concerning the evolution of the pore water pressure, the evolution is similar for 3D numerical results and experimental data, but the numerical results underestimate the observed evolution. This comparison is done in Figure 15 for the sensors AT85E and AT93E.

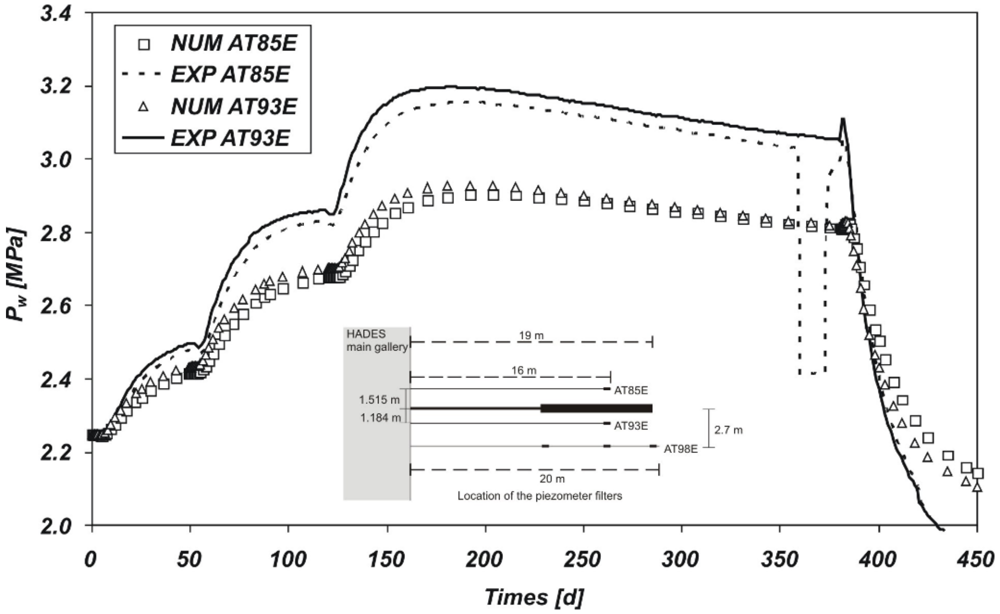

Figure 15: Comparison of the observed excess pore water pressure and the numerical result

2.4 Additional computations

Additional computations by ULg

During this benchmark exercise, ULg has realised different 3D modellings considering different sources of anisotropy. Indeed, the anisotropy can be considered in the mechanical, the hydraulical or thermal problem. The aim of this work is to study each case of anisotropy separately, in order to better understand their influence on the results and especially on the excess pore water pressure and on the thermal dissipation.

Considering anisotropy in the mechanical model, ULg uses a transversely isotropic elastic law with five independent parameters. The anisotropic model has two consequences (Figure 16): on one hand, a higher pore water pressure is obtained with this law due to a higher value of the elastic moduli. On the other hand, it is important to note that, only with the anisotropic mechanical model, an increase of pore pressure is observed when decreasing the heat power. The same observation has been made based on the in situ measurements. The phenomenon is also observed when increasing the heat power. But the numerical increase is less large than that of the in situ measurements.

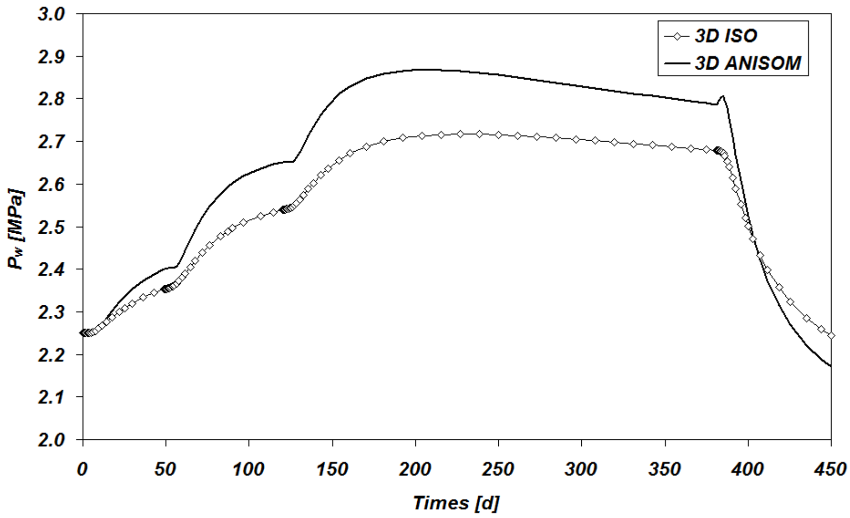

Figure 16: Comparison of the evolution of the pore water pressure for the senor AT85E between the isotropic case and the mechanical anisotropic case

The hydraulic anisotropy has also an influence on the results but can not produce a significant improvement of the predictions for the range of permeability considered in the modelling.

The thermal anisotropy is characterised by a vertical thermal conductivity smaller than the horizontal conductivity. As a consequence, the dissipation of the heat in the horizontal direction is larger than in the vertical direction (Figure 17). This anisotropy allows a better fitting of the temperature measurements at the different boreholes.

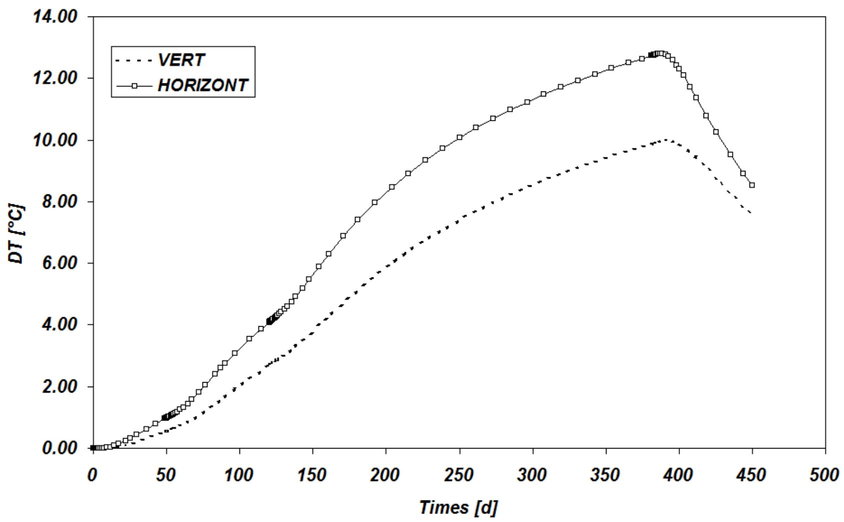

Figure 17: Evolution of the temperature for two points located at a distance of 2.75 m from the heater

Additional computations by EPFL

The EPFL team carried out the computations with an additional objective in mind; to assess the influence of non-linear thermo-elasticity and thermo-plasticity on the THM response of the repository.

Mechanical model

The ACMEG-T constitutive model accommodates non-linear thermo-elasticity coupled with a multi-dissipative thermo-plasticity in order to reproduce most thermo-mechanical features. The elastic part of the deformation increment $d\boldsymbol{\varepsilon}^e$ is expressed as following:

$$d\boldsymbol{\varepsilon}^e = \mathbf{D}d\boldsymbol{\sigma}' - \boldsymbol{\beta}'_T\, dT \tag{8.1}$$

$\boldsymbol{D}$ is the mechanical elastic tensor defined by the non-linear bulk and shear modulus, K and G, respectively,

$$K = K_{ref}\left(\frac{p'}{p_{ref}}\right)^{n^e} \quad ; G = G_{ref}\left(\frac{p'}{p_{ref}}\right)^{n^e} \tag{8.2}$$

where p' is the mean effective stress, n^e the non-linear elasticity exponent, p'_{ref} the reference pressure, K_{ref} and G_{ref} the bulk and shear modulus at the reference pressure, respectively. $\boldsymbol{\beta}'_T$ is the thermal expansion tensor. Considering an isotropic thermal dilatation, one can express the thermal expansion tensor as $\boldsymbol{\beta}'_T = 1/3\,\beta'_s \boldsymbol{I}$ with β'_s being the volumetric thermal expansion coefficient of the solid skeleton.

Using the concept of multi-mechanism plasticity, the total irreversible strain increment $d\boldsymbol{\varepsilon}^p$ is induced by two coupled dissipative processes: an isotropic and a deviatoric plastic mechanism. Each of them produces plastic strain increment, $d\boldsymbol{\varepsilon}^{p,iso}$ and $d\boldsymbol{\varepsilon}^{p,dev}$, respectively.

The 2D results of EPFL are briefly presented to highlight the influence of non-linear thermo-elasticity and thermo-plasticity on the THM response of the repository (Figure 18).

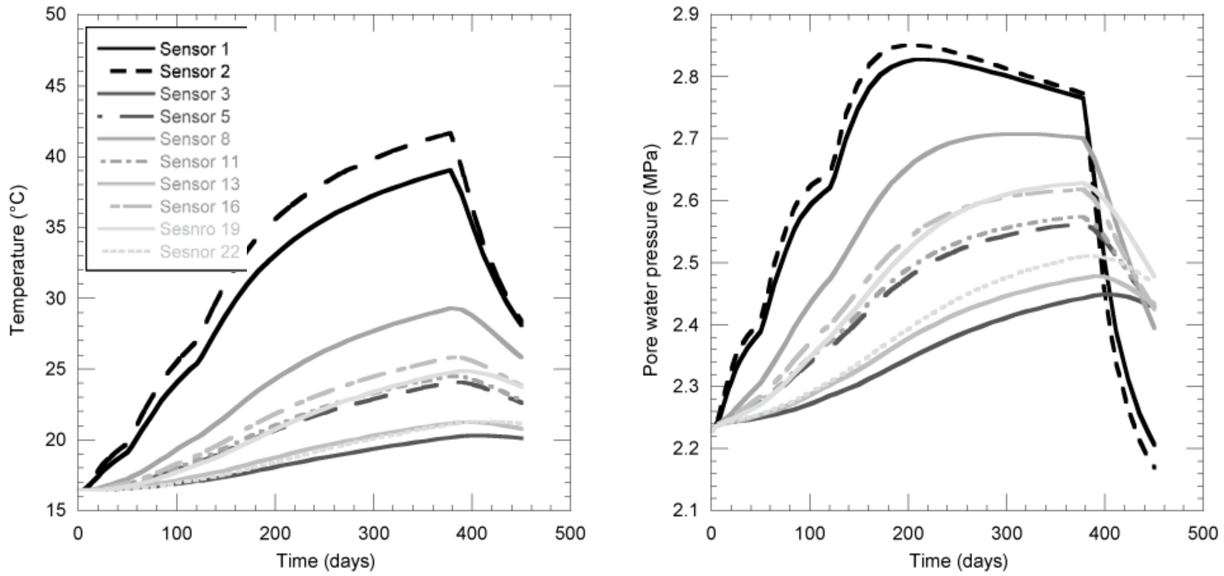

Figure 18: Time evolution of temperature, pore water pressure in the 2D modelling

The obtained pore pressures and stress fields differ from those obtained by the other teams. The differences are mainly due to the non-linear elasticity and the thermo-plasticity of the ACMEG-T model. An increase in rigidity as well as progressive plasticity induced by heating, causing an increase of the preconsolidation pressure, is considered in ACMEG-T. This causes an increase in excess pore water pressures, and consequently in effective stresses.

Additional computations by EURIDICE

Several additional cases of three dimensional coupled THM modellings were performed for ATLAS III test in order to interpretate the field data of pore water pressure. The 3D model was the same that the model proposed in the benchmark exercise, except that a steel tube with 19 m length, 95 mm external radius and 15 mm thickness was included in the geometry. The initial stress state differs from the proposed one by the fact that a lateral total stress coefficient $K_0 = 0.85$ is considered in the modelling.

Based on the selected THM parameters, especially the thermal conductivity, the best comparison of temperature between measurement and modeling we obtained is presented in Figure 19, and the comparison can be considered excellent.

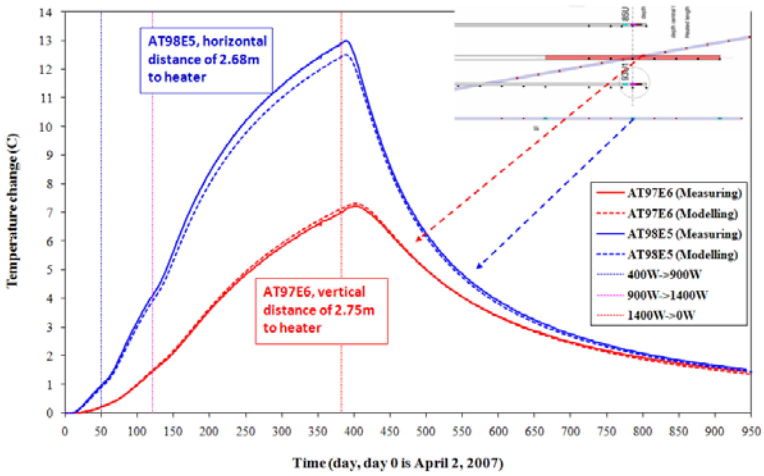

Figure 19: Comparison between modeling and measurement of temperature in sensors TC-AT98E5 and TC-AT97E6

To reproduce the measured pore water pressure by modeling, many cases have been calculated: isotropic elasticity, anisotropic elasticity and a Camclay model. The conclusion is that only with the anisotropic elastic parameters (E_h=700 MPa, E_v=350 MPa, G_v=140 MPa being used), the temporary pore pressure decrease (increase) after increasing (switching off) the power can be reproduced, but the measured pore pressure change is still around 30% underestimated by modeling. The comparison with good match between measured pore water pressure and modeled one is obtained especially by using the doubled moduli than in case 2: the modeling can not only well reproduce the temporary pore water pressure decrease after increasing power and temporary pore water pressure increase after cooling in all the five piezometers, but also it gives the close magnitude of the pore water pressure change to the measured one. The magnitude of the used Young's modulus is close to the one that can be obtained from the wave velocities of seismic tests on undisturbed Boom clay in HADES [9].

From the above several cases, it could be found that (1) only when anisotropic mechanical parameters are used, the modelling can reproduce the temporary pore water pressure decrease after increasing power and temporary pore water pressure increase after cooling observed in all the five piezometers, which provides the indirect evidence of the mechanical anisotropic behaviour of Boom clay; (2) Higher Young's moduli could be reasonably employed to obtain better comparison of pore water pressure between modelling and measurement.

Additional computations by UPC

CIMNE did a number of additional 3D THM computations to analyse the temperature and pore water pressure measurements registered in the third phase of the ATLAS experiment. The code used is Code_Bright and a description of the Thermo-Hydro-Mechanical formulation may be found in [11]. Anisotropic thermal conduction law, anisotropic water flow and anisotropic elastic constitutive law were used. The gallery from where the heating borehole was drilled and the heater itself are discretized explicitly. In contrast with other teams, a draining boundary condition was applied on the heater walls.

The thermal problem was solved for any possible combination of thermal conductivity couple. The best fitting thermal conductivity couple was determined for each sensor and each heating stage according to a method developed in [15]. The results are summarized in Figure 20-a. The average obtained from all the sensors is very close to the reference values (1.7-1.2W/m/K**)**. The same exercise was repeated using a power loss coefficient. For a power loss coefficient of 85%, the best fitting thermal conductivity couple converges 1.4-0.9W/m/K for all sensors as shown in Figure 20-b (1.4-0.95W/m/K).

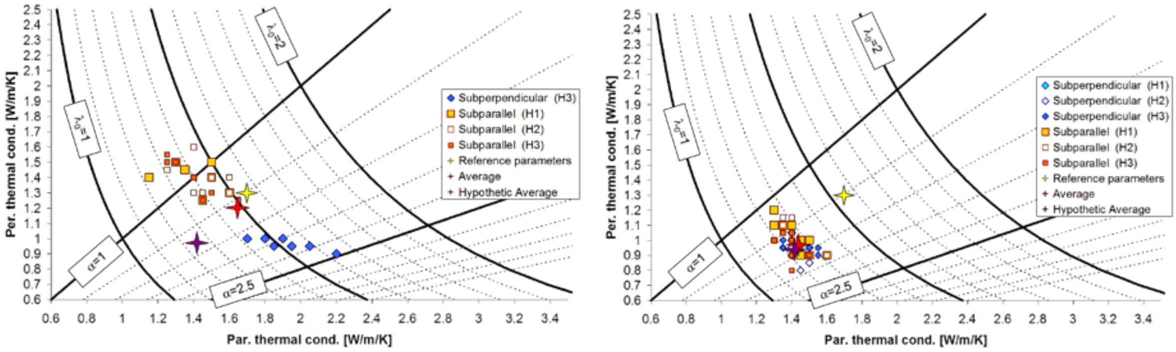

(a) (b)

Figure 20: Thermal conductivity values determined for each sensor and each heating period in the ATLAS experiment (a) 100% of the power (b) power loss coefficient of 85% . The yellow four branches star indicates the reference thermal conductivity values and the red four branches star the average thermal conductivity from this study.

The applied thermal load triggers a Hydro-Mechanical response of the rock as both, the rock skeleton and the water in the rock pores expand when heated. The hydro- and the mechanical response are tightly coupled. The heated volume around the heater undergoes an expansion as a consequence of the temperature increase. The constant temperature rock volume reacts mechanically to the expansion of the heated volume: the non-heated volume has a tendency to radial compression and circumferential expansion (relative to the heater).

As soon as the temperature starts to increase, two processes are in competition: compression of the water because thermal expansion of the water is larger than that of the rock skeleton and dissipation of the generated excess pore pressure. In a first stage, pore water pressure will increase: compression of the water is stronger than the dissipation. It should be noted that the pore water pressure increase rate depends on 1) the temperature increase rate and 2) the permeability of the medium. After some time, temperature increase rate decreases and excess pore water pressure starts to dissipate faster than they are generated by the temperature increase. Note that the dissipation of high pore pressures in the near field may also trigger an increase of pore water pressure in the far field.

Pore water pressure changes generated by temperature changes also contribute to the deformation of the medium through the effective stress concept.

Excess pore water pressure measured in the five sensors of the ATLAS experiment is plot against simulation results in Figure 21. The good agreement between measurements and simulation was achieved by introducing one change in the Boom clay reference parameter set: the equivalent water permeability was decreased from 3.2 $10^{-19}m^2$ to 1.1 $10^{-19}m^2$ (anisotropy ratio was kept constant). A similar agreement may have been reached by an increase of the stiffness.

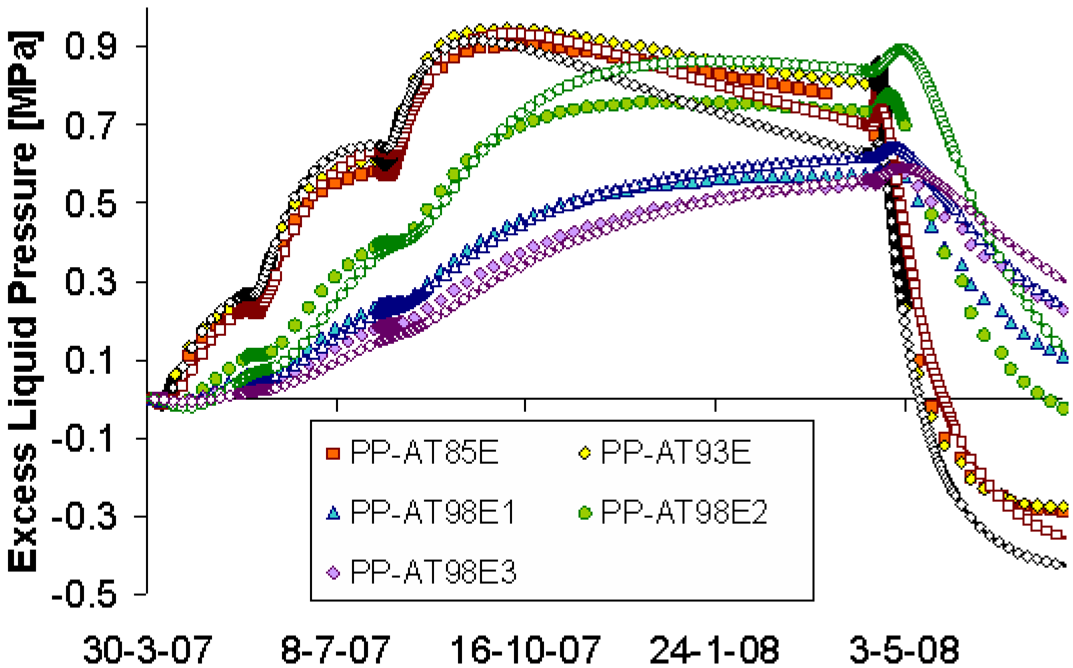

Figure 21: Measured (filled symbols) and simulated (white symbols) excess pore water pressure generated by heating in the ATLAS experiment from 30/03/07 to 26/07/08.

The sensitivity analysis of the permeability allows also for estimating the importance of this parameter. A difference of one order of magnitude between the two extreme cases indicates a non-negligible difference of 0.5MPa and 1.5MPa excess pore pressure.

2.5 Conclusions

The numerical modelling of the small-scale in situ experiment ATLAS III has been carried out in two successive steps. First, a benchmark exercise has been defined with three different geometries, based on the experimental set-up. The three configurations enable the participating teams to consider different levels of complexity: (1) a one-dimensional axisymmetric model is easy to handle and gives first insights of the relevant physical phenomena. (2) A 2D axisymmetric geometry helps to reproduce better the experiment, in the radial direction and the axial as well. (3) Finally, as far as anisotropy was suspected to play an important role, a fully 3D model has been also proposed for the benchmark exercise. All the participating teams were let free to select the geometry they want to deal with for this benchmark. Even if the in situ measurements were known at the beginning of the exercise, it was decided that the results of this exercise, provided by the different teams (ULg, EPFL, EURIDICE, UPC, NRG), consisted to blind predictions.

During the benchmark exercise, agreement between the predicted results of the different teams has been obtained. Also, first interpretations of predicted results have been made in term of principal stress evolution, followed stress path, pore water pressure and displacement profiles.

Then, in the second phase of simulations, the liberty was given to each team to focus on any specific features of behaviour related to the experimental evidences. The following aspects have been mainly addressed: (i) the contribution of each source of anisotropy (mechanical, hydraulical and thermal) of Boom Clay, (ii) the effect of the non-linear elasticity and the thermo-plasticity, (iii) the research of the best estimate for the anisotropic thermal conductivity and the anisotropic elastic moduli.

To reproduce the temperature modification and the pore pressure changes during the complex heating procedure, it has been noticed that plasticity does not play an important role for this experiment. The conclusion is that this in situ test characterizes mostly the THM behaviour of the undisturbed host rock. That is why most of the modelling uses thermo-elastic constitutive models.

The second aspect clearly evidenced by the experimental and numerical results is that anisotropy is really a key issue in the behaviour of the undisturbed rock. In order to reproduce the temperature field during the experiment, it is necessary to introduce an anisotropic thermal conductivity. The cross-anisotropic elasticity is mandatory for the modelling of the temporary pore water pressure decrease after increasing power and temporary pore water pressure increase after cooling observed in all the five piezometers. Moreover, for a correct prediction of the pore pressure increase, it is necessary to use higher elastic moduli than the one commonly used for numerical modelling of the EDZ.

As a conclusion, through numerical modelling of the in situ test ATLAS III, we have shown that the developed numerical models are able to reproduce the main processes that occur in Boom Clay during the hydro-mechanical hollow cylinder tests.

3 Test setup and field data

The original set-up was developed in 1992 by SCK-CEN within the framework of the European project Interclay II (1990~1994) [1]. From July 1993, a constant heat source of 900 W was applied in the heating test until June 1996, and this stage of test is named as ATLAS I. The test continued from June 1996 to May 1997 with increased and constant heat power of 1800 W, and shutdown and natural cooling started from June 1997, namely ATLAS II [2-4]. In 2006, the set-up has been refurbished, the heater was activated from April 2007 to April 2008 with stepwise power increase, then the heater was shut down instantaneously. This is the third life of ATLAS test and therefore named ATLAS III.
The objectives of ATLAS III test are: (1) To obtain a more accurate and extended field of the temperature and pore water pressure by recently drilling two additional boreholes equipped with more sensors, which enables to check the possible thermal anisotropy. (2) To test a new data acquisition system which has a higher data acquisition rate and is fully automatic instead of a low-rate and manual data acquisition system used in ATLAS I and II. (3) To have better assessment of THM characterisation of Boom clay at larger scale and at different temperature levels. (4) To serve as preparation for Praclay Heater Test, which is a large scale heater test in Boom clay intending to simulate a disposal gallery at real scale, and to provide a good link with Praclay heater test by up-scaling. (5) To provide data for a modeling benchmark in the European project TIMODAZ (2006~2010).

3.1 Test set-up

The test setup is composed of a central borehole with heater and of four boreholes with instrumentation. The main borehole (AT89E) with heater and three other boreholes (AT85E, AT93E, and AT98E) are in the same horizontal plane while a last borehole (AT97E) is slightly inclined towards the heater borehole. The inclination is about 10° down and 10° towards the heater borehole. Figure 20 illustrates the layout of the ATLAS III test.

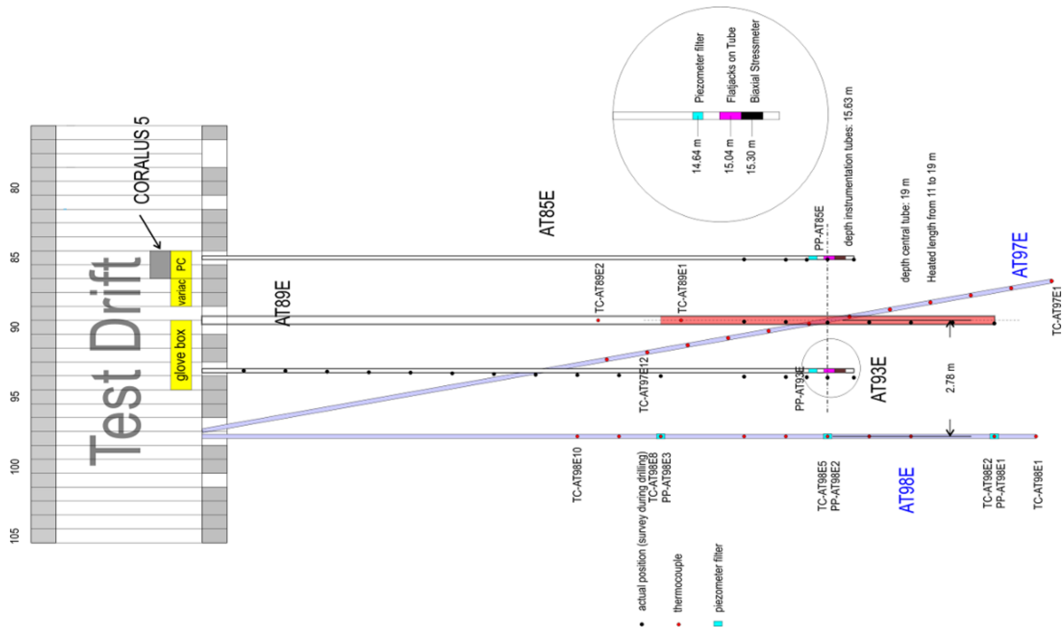

Figure 22: Layout and instrumentation of ATLAS III in situ test

(1) *Borehole AT89E* (see Figure 20)

The central borehole AT89E is located at the Test Drift ring 89/90 with drilling depth of 19 m and drilling diameter of 230 mm, and the borehole is cased by steel tube with external diameter of 190 mm and internal diameter of 160 mm. Attached to the inner wall of the casing are four U-sections, which are distributed evenly over the perimeter. Grooved aluminium strips fit into these sections, heater cables are mounted on these strips, and heated section runs from depth of 11 m to depth of 19 m.

(2) *Boreholes AT85E and AT93E* (see Figure 20)

To both sides of the heater borehole AT89E, two instrumentation boreholes AT85E and AT93E are installed. AT85E is located at Test Drift ring 85 (about 1.5 m to the left of the central borehole), and AT93E is located at Test Drift ring 93 (about 1.3 m to the right). Each borehole is cased by steel tube with diameter of 60 mm.
At the deep ends of both boreholes, flatjacks to measure the total pressures and piezometer filters (connected to vibrating wire sensors in the gallery) to measure the pore water pressure are situated between 14.6 m and 15.3 m depth, which coincides with the heater mid-plane.

(3) *Additional boreholes AT97E and AT98E* (see Figure 20)

To obtain measurement over a larger range in ATLAS III than that in ATLAS I and ATLAS II, to test the piezometer design and installation envisaged for Praclay gallery, to serve as a far field piezometer for the future large scale Praclay Heater Test, and to get a better picture of the possible thermal anisotropy, the two additional boreholes AT97E and AT98E have been drilled in Jan 2006 from the Test Drift ring 97/98.
Borehole AT98E is located at horizontal distance of 2.7 m to the central borehole, it has a length of 20 m, and it is equipped with 10 temperature sensors and 3 piezometer filters (one in the middle plane of the heater, and one at each side at 4 m distance).
Borehole AT97E has been drilled at the same entrance position as AT98E, having depth of 21 m and diameter of 95 mm, and it is cased by a PVC tube with an external diameter of 80 mm and an internal diameter of 40 mm, being inclined at 10º downward and with horizontal deviation (to the left) of 10º. This one is equipped with 12 temperature sensors and has a length of 21 m.

(4) Data acquisition

To deal with the increased number of sensors and higher data rate requirements in ATLAS III test, the data acquisition system is updated.

Borehole	Sensor No.	Distance to borehole Entrance (m)	Sensor Type	Note
AT85E	Left/Top/Right/Bottom	15.04	Thermistor	"Left" is discarded
	PP-AT85E	14.64	Piezometer	
	Left/Top/Right/Bottom	15.04	Flatjack	
AT93E	Left/Top/Right/Bottom	15.04	Thermistor	"Right" is discarded
	PP-AT93E	14.64	Piezometer	
	Left/Top/Right/Bottom	15.04	Flatjack	

AT97E	TC-AT97E1~12	21~10	Thermocouple	Sensors are homogeneously distributed
AT98E	TC-AT98E1	20	Thermocouple	
	TC-AT98E2	19		
	TC-AT98E3	17		
	TC-AT98E4	16		
	TC-AT98E5	15		
	TC-AT98E6	14		
	TC-AT98E7	13		
	TC-AT98E8	11		
	TC-AT98E9	10		
	TC-AT98E10	9		
	PP-AT98E1	19	Piezometer	
	PP-AT98E2	15		
	PP-AT98E3	11		

Table 2: Summary of the instrumented sensors for ATLAS III in situ test

This setup allows observing the thermal perturbation up to about 2.7 m in the horizontal and vertical directions. Table 2 gives a brief summary of the main features of 4 boreholes. It should be noted that after drilling, optical survey of the boreholes was performed to check their real deviations with respect to their theoretical positions, based on which the actual coordination of all the sensors are carefully calculated.

The heater has been re-activated on April 2, 2007 starting with a relatively low heating power of 400 W, the power has been increased stepwisely to 900 W then to 1400 W and was finally shut off instantaneously on April 17, 2008 to observe the effects of the cooling transient. Table 3 gives the main features of the heating process. Until Nov. 2, 2009, ATLAS III test has lasted for 945 days, with heating for 381 days and cooling for 564 days.

Step	Phase	Power (W)	Date	Day No.	Duration (days)
1	Heating	0→400	Apr. 2→Apr. 5, 07	0→4	4
2	Stalilization	400	Apr. 06, 07→May 20, 07	4→49	45
3	Heating	400→900	May 21, 07→May 25, 07	49→54	5
4	Stabilization	900	May 26, 07→Jul. 29, 07	54→120	66
5	Heating	900→1400	Jul. 30, 07→Aug. 03, 07	120→125	5
6	Stabilization	1400	Aug. 04, 07→Apr. 16, 08	125→381	256
7	Cooling	0	Apr. 17, 08→Nov. 02, 09	381→945	564

Table 3: Heating and cooling cycle of the ATLAS III test

3.2 *Field data*

ATLAS III test yielded a large amount of good-quality data on the thermal, hydraulic and mechanical perturbations. Some interesting phenomena are revealed by the meaurements of temperature, pore water pressure and total stress.

3.2.1 Measured temperature

As indicated in Table 2, there is one temperature sensor in AT85E, one temperature sensor in AT93E, twelve temperature sensors in AT97E, and ten temperature sensors in AT98E. The measured temperature are displayed in Figure 21, Figure 22 and Figure 23, where the vertical dashed lines indicate the times of increasing power or shutting down the power.

(1) Boreholes AT85E and AT93E

In these two boreholes, the temperatures are measured at about 15 m depth, i.e. in the symmetry plane perpendicular to the heating section of AT89E and passing through its mid-point, with 4 thermistors (one in each flatjack) in each borehole. Ideally, the four sensors in each borehole should have the same temperature, but sensor "93right" presents the highest initial offset, and sensor "85left" shows some instable behaviour. Therefore it is assumed that these sensors (more than 15 years old) are damaged and their measurements are discarded for temperature interpretation, so they are not included to calculate the average temperature increase at each borehole. Figure 21 shows the average temperature increases in these two boreholes.
The temperature increase is larger at AT93E than that at AT85E due to the shorter distance between AT93E and the heater tube (see Figure 20). The maximum temperature increases of 24°C and 22°C are observed in sensor AT93E and sensor AT85E respectively. The successive heating steps are well visible. A decrease in temperature is only visible 2 days after switching off the heater.

(2) Borehole AT97E

A maximum temperature increase of 8°C is observed at the sensor situated in the symmetry plane of the heater. All measured temperature by sensors in borehole AT97E (see Figure 22a and Figure 22b) show a delay of the temperature decrease after switching off the heater. Especially the temperature in sensor AT97E1 started to drop after switching off the heater for nearly 3 months, and sensor AT97E1 is located furthest away from the heater.

(3) Borehole AT98E

All measured temperatures by sensors in borehole AT98E (see Figure 23a and Figure 23b) show a delay of the temperature decrease after switching off the heater. A maximum temperature increase of 13°C is observed at the sensor located in the symmetry plane of the heater.

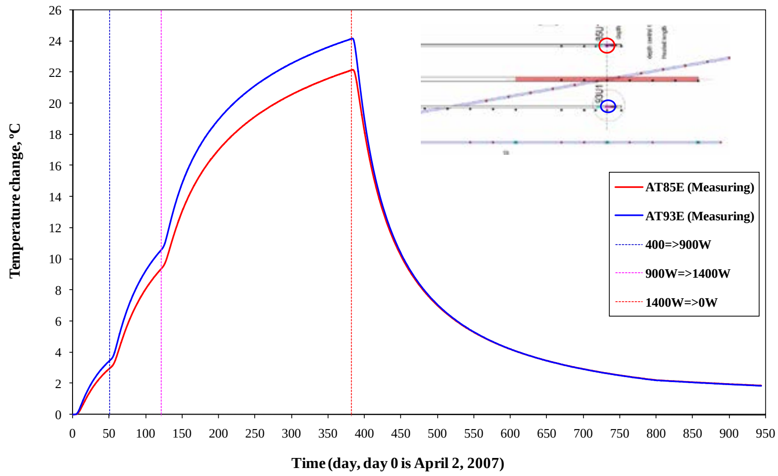

Figure 23: Temperature increase of sensors located in boreholes AT85E and AT93E

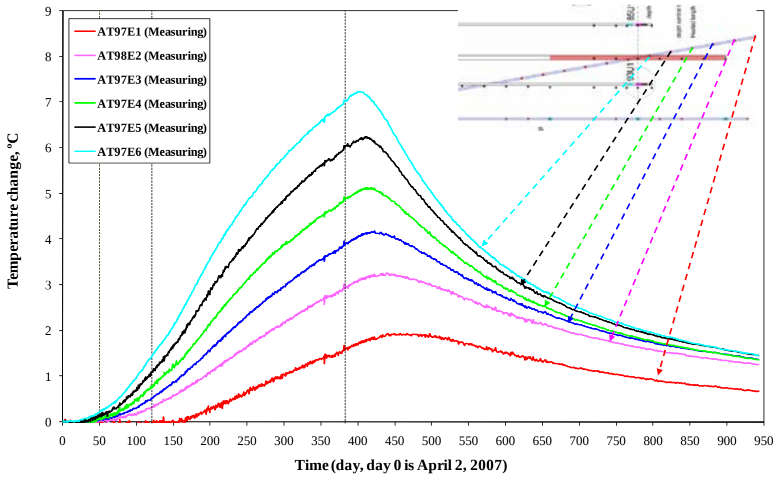

(a) Sensors AT97E1~AT97E6

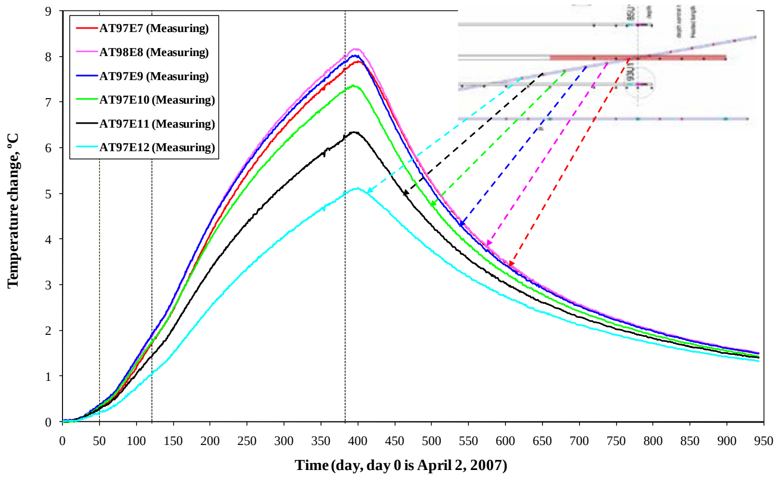

(b) Sensors AT97E7~AT97E12

Figure 24: Temperature increase in sensors along borehole AT97E

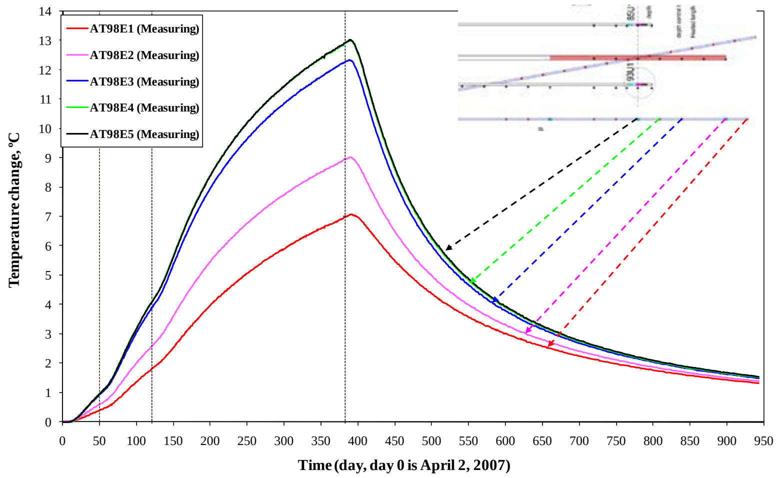

(a) Sensors AT98E1~AT98E5

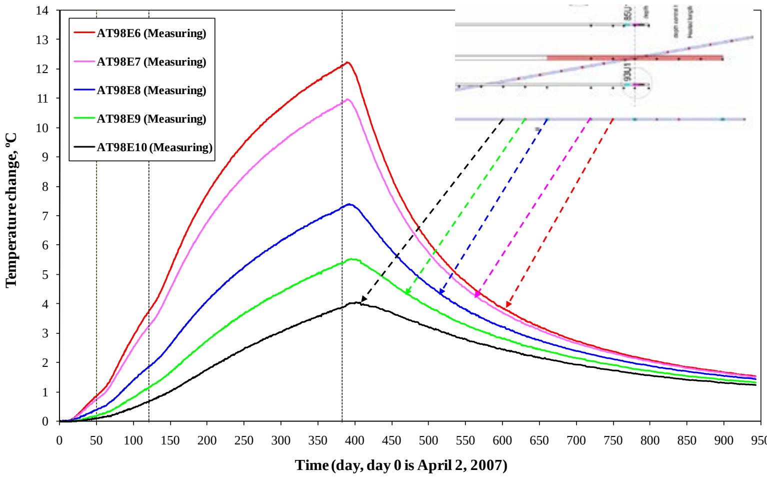

(b) Sensors AT98E6~AT98E10

Figure 25: Temperature increase in sensors along borehole AT98E

3.2.2 Measured pore water pressure

As shown in Table 2 there is one piezometer in AT85E at depth 14.6 m, one piezometer in AT93E at depth 14.6 m, and three piezometers in AT98E at depth 11 m, 15 m, and 19 m, respectively. Figure 24 shows the evolution of the pore water pressure. The maximum pore water pressures increase ranges between 0.5 MPa and 1.0MPa. Due to the slow drainage towards the underground laboratory, initial pore water pressures range from 1.2 MPa to 1.75 MPa depending on the distance to the Test Drift. At the end of March 2008, the sudden drop of pore pressure is imposed on the piezometer PP-AT85E in order to determine the permeability of the massif near this sensor.

It is interesting to observe that at the start of each heating phase, a temporary decrease of the pore pressure occurs in all the piezometers. The opposite phenomenon is observed when switching off the heater. During the cooling phase, the measured pore water pressure changes in sensors PP-AT85 and PP-AT93 drop maximally to around -0.29 MPa (i.e. 0.29 MPa lower than initial pore water pressure before heating), while the corresponding measured pore water pressure changes in sensors PP-AT98E1, PP-AT98E2 and PP-AT98E3 drop to around -0.1 MPa,-0.04 MPa, and 0.02 MPa. The pore water pressures are now tending to recover slowly to their initial states before heating.

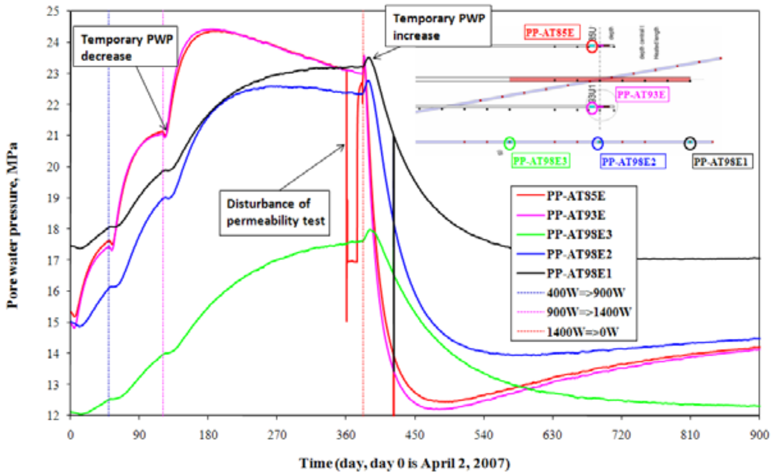

Figure 26: Evolution of pore water pressures in five sensors located in boreholes AT85E, AT93E and AT98E

3.2.3 Measured total stress

As indicated in Table 2 there are four flatjacks (at the left, top, right and down sides of the instrumentation tubings) at depth 15 m in AT85E and AT93E respectively. Figure 25 and Figure 26 show the temporal evolution of the total stress measured by flatjacks in boreholes AT85E and AT93E, respectively. It can be observed that the total stresses present variations with the different sensors orientations for both AT85E and AT93E; besides, the temporary decrease of total stress at the start of each heating phase and temporary increase of total stress at the start of cooling phase are also noticed.

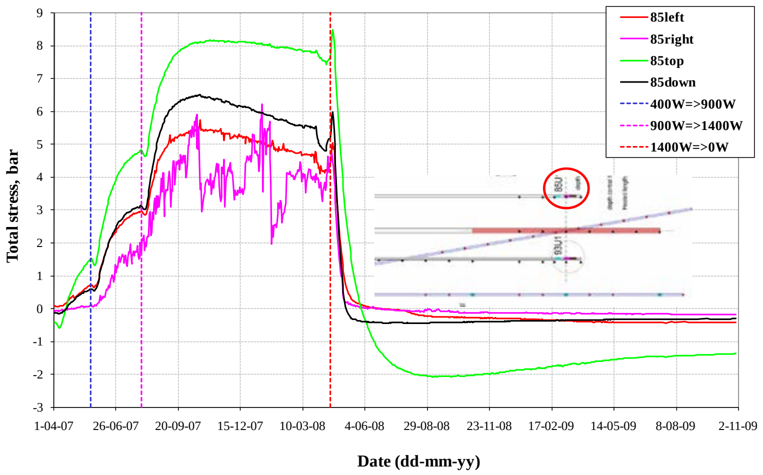

Figure 27: Evolution of total stress measured by flatjacks in AT85E

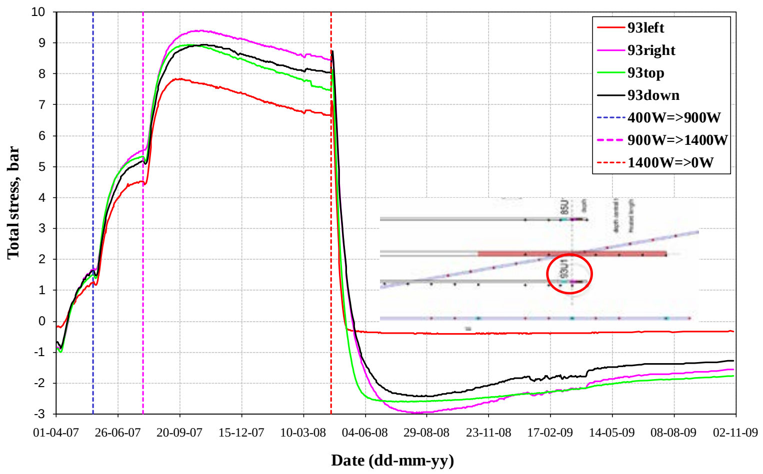

Figure 28: Evolution of total stress measured by flatjacks in AT93E

4 Exercise definition

The benchmark exercise consists in the reproduction of the heating and the cooling phases. Figure 27 and Figure 28 present the geometry of the experiment used for the modelling. As seen previously, the experiment is composed of a principal heater borehole and of four boreholes equipped with instrumentation (AT85E, AT93E, AT97E, and AT98E). The heater and 3 boreholes (AT85E, AT93E, and AT98E) are in a same horizontal plane while a last borehole (AT97E) is inclined towards the heater.

The main tube with heaters has a length of 19 m and a diameter of 190 mm.

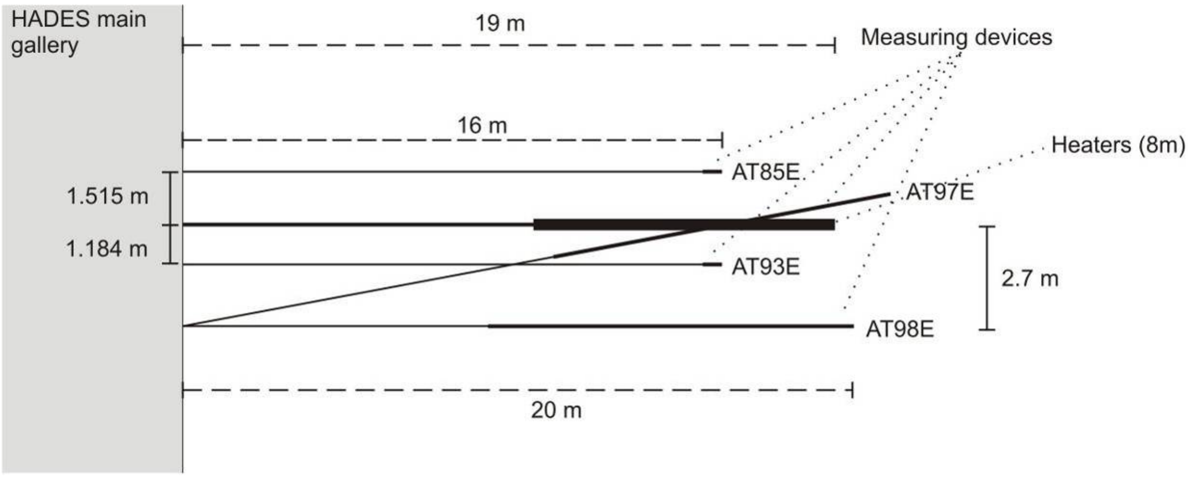

Figure 29: Geometry of ATLAS III. View in a horizontal plane

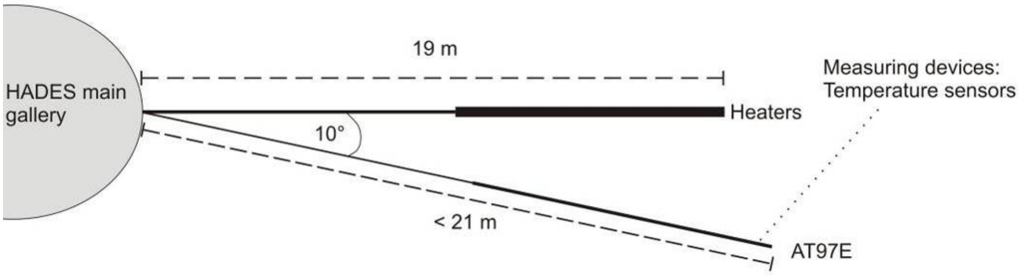

Figure 30: View of ATLAS experiment in a vertical plane

As explained in section 3.1, the experimental procedure consists in a thermal loading applied at the heater borehole. Figure 29 presents the power dissipated by the heaters as a function of time. The thermal loading is composed of three steps. The first one rises the power from 0 to 400 W in four days and a period of 45 days of stabilisation is allowed. The second one enhances the power from 400 W to 900 W in five days and a period of 66 days of stabilisation is allowed. Finally, the third one, the power is increased up to 1400 W in five days and a period of 256 days of stabilisation is allowed. Then, the power is switch off instantaneously and a cooling phase goes on 69 days. At the difference to the experiment, the modelling stops after 450 days. Indeed, all the cooling phase is not modelled because the benchmark exercise was launched in January 2009 and the experiment ends in November 2009. As a consequence, only 69 days of the cooling cycle have been considered in this exercise. Of course, all the heating phase is considered.

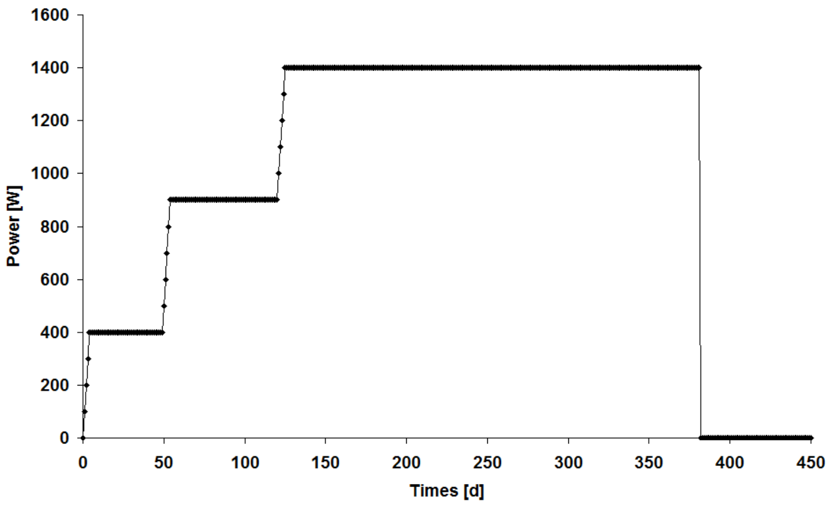

Figure 31: Evolution of the power dissipated by the heaters during the ATLAS III experiment

Table 4 proposes a summary of the idealized heating/cooling cycle of ATLAS III experiment.

Phase	Number of days	Power [W]
Step 1: heating	4	0 ➔ 400
Step 1: stabilisation	45	400
Step 2: heating	5	400 ➔ 900
Step 2: stabilisation	66	900
Step 3: heating	5	900 ➔ 1400
Step 3: stabilisation	256	1400
Step 4: cooling	69	0

Table 4: Summary of the different steps of the heating/cooling cycle

4.1 Constitutive models and parameters

4.1.1 Mechanical model

In this benchmark, the mechanical properties of Boom clay may be considered as isotropic or anisotropic. Indeed, the structure of clay in band layers (Mertens et al., 2003) permit to consider this material as transversely isotropic.

Only elastic model have been considered in this modelling because the size of the EDZ is relatively small (as the borehole diameter is small) compare to the extent of host rock affected by the thermal process. That is the reason why the excavation of the borehole has not been considered: no EDZ has been created and a thermo-elastic modelling seems sufficient to reproduce the effect of the temperature far away from the heater.

Linear isotropic elasticity

The first mechanical model considers only an isotropic elastic law, which can be summarised by the following equation:

$$\dot{\sigma}_{ij} = C^{e}_{ijkl}\dot{\varepsilon}^{m,e}_{kl} \tag{4.1}$$

with

$$C^{e}_{ijkl} = \frac{E}{(1+\upsilon)(1-2\upsilon)}\begin{pmatrix} (1-\upsilon) & \upsilon & \upsilon & & & \\ & (1-\upsilon) & \upsilon & & & \\ & & (1-\upsilon) & & & \\ & & & \frac{(1-2\upsilon)}{2} & & \\ & & & & \frac{(1-2\upsilon)}{2} & \\ & & & & & \frac{(1-2\upsilon)}{2} \end{pmatrix} \tag{4.2}$$

Where E is the Young's modulus and υ the Poisson's ratio.

Linear transversely isotropic elasticity

The second proposed mechanical model still considers an elastic model but, in this case, the Hooke's law defines a transversely isotropic elastic medium. The stress-strain equation is defined by eq. (4.1).

The behaviour of a transversely isotropic material may be described by five independent parameters (Love, 1944). The required material parameters are two Young' modulus (E_v and E_h), two Poisson's ratio (ν_{vh} and ν_{hh}) and a shear modulus (G_{vh}). The subscripts *v* and *h* will be used for stiffness parameters to indicate vertical and horizontal directions respectively. Poisson's ratio for strain in the vertical direction due to a horizontal direct stress is ν_{vh}. Poisson's ratio for strain in any horizontal direction due to a horizontal direct stress at right angles is ν_{hh}.

The remaining parameters are not independent.

$$\frac{\nu_{hv}}{E_h} = \frac{\nu_{vh}}{E_v} \text{ and } G_{hh} = \frac{E_h}{2(1+\nu_{hh})} \tag{4.3}$$

In this case, the Hooke's matrix is:

$$C_{ijkl}^{e} = \begin{bmatrix} E_h \frac{1-n\nu_{vh}^{2}}{(1+\nu_{hh})m} & E_h \frac{\nu_{hh}+n\nu_{vh}^{2}}{(1+\nu_{hh})m} & E_h \frac{\nu_{vh}}{m} & & & \\ E_h \frac{\nu_{hh}+n\nu_{vh}^{2}}{(1+\nu_{hh})m} & E_h \frac{1-n\nu_{vh}^{2}}{(1+\nu_{hh})m} & E_h \frac{\nu_{vh}}{m} & & & \\ E_h \frac{\nu_{vh}}{m} & E_h \frac{\nu_{vh}}{m} & \frac{E_v\left(1-\nu_{hh}\right)}{m} & & & \\ & & & \frac{E_h}{2\left(1+\nu_{hh}\right)} & & \\ & & & & G_{vh} & \\ & & & & & G_{vh} \end{bmatrix} \tag{4.4}$$

with

$$m = 1-\nu_{hh} - 2n\nu_{vh}^{2} \quad \text{and} \quad n = \frac{E_h}{E_v} \tag{4.5}$$

The strain energy function should be positive. Consequently, the five independent parameters are bounded following:

$$E_v > 0;\ E_h > 0;\ G_{vh} > 0 \tag{4.6}$$

$$-1 < \nu_{hh} < 1 \tag{4.7}$$

and

$$\frac{E_v}{E_h}(1-\nu_{hh}) - 2\nu_{vh}^{2} > 0 \tag{4.8}$$

Thermo-elasticity

For both cases, the total strain rate $\dot{\varepsilon}_{ij}$ is considered as the sum of the mechanical elastic strain rate $\dot{\varepsilon}_{ij}^{m,e}$ and the thermal elastic strain rate $\dot{\varepsilon}_{ij}^{e,th}$:

$$\dot{\varepsilon}_{ij}^{e} = \dot{\varepsilon}_{ij}^{m,e} + \dot{\varepsilon}_{ij}^{th,e} \quad \text{with} \quad \dot{\varepsilon}_{ij}^{th,e} = \beta \dot{T} \delta_{ij} \tag{4.9}$$

where β is the medium linear thermal expansion coefficient [K^{-1}] and δ_{ij} is the Kronecker symbol.

4.1.2 Balance equations

Momentum balance equation

The momentum balance equation is written for quasi-static conditions:

$$div(\sigma_{ij}) = 0 \tag{4.10}$$

where σ_{ij} is the total stress tensor [Pa]

The total stress is expressed by:

$$\sigma_{ij} = \sigma'_{ij} + p_w \tag{4.11}$$

Water mass balance equation

The water mass balance equation is written:

$$\dot{S}_w + div(\underline{f}_w) = Q_w \tag{4.12}$$

where $\dot{S}_w$ is the water storage term [kg.m^{-3}.s^{-1}], $\underline{f}_w$ is the water mass flux [kg.m^{-2}.s^{-1}] with respect to the solid configuration (updated Lagrangian configuration) and Q_w is a term of production / consummation of water [kg.m^{-3}.s^{-1}].

$$\underline{f}_w = \rho_w . \underline{q}_w \tag{4.13}$$

where $\underline{q}_w$ is the mean speed of the liquid phase relative to the solid phase [m.s^{-1}].
These two equations can be regrouped as follows:

$$\frac{\partial}{\partial t}(\rho_w.\phi) + div\left(\rho_w.\underline{q}_w\right) - Q_w = 0 \tag{4.14}$$

Darcy's Law

The general Darcy flow law is used and defines the Darcy fluid velocity $\underline{q}_w$ as a linear function of permeability and the gradient of fluid pressure p_w:

$$\underline{q}_w = -\frac{\underline{\underline{k}}_w}{\rho_w.g}\left(\underline{\nabla} p_w\right) \tag{4.15}$$

where $\underline{\underline{K}}_w$ is the anisotropic tensor of permeability. This tensor has nine components and may be written in a general form as follows:

$$\underline{\underline{k}}_w = \begin{bmatrix} k_{xx} & k_{xy} & k_{xz} \\ k_{yx} & k_{yy} & k_{yz} \\ k_{zx} & k_{zy} & k_{zz} \end{bmatrix} \tag{4.16}$$

If the medium is supposed to be isotropic, the relation becomes:

$$\underline{q}_w = -\frac{k_{\text{int}}}{\mu_w}\left(\underline{\nabla} p_w\right) \tag{4.17}$$

where k_{int} is a scalar in isotropic situation $k_{\text{int}} = K_w \dfrac{\mu_w}{\rho_w.g}$;

k_{int} is the intrinsic permeability coefficient [m²] ;
K_w is the isotropic permeability [m/s] ;

μ_w is the fluid dynamic viscosity [Pa/s].

Heat balance equation

The heat balance equation can then be written:

$$\dot{S}_T + div(\underline{V}_T) - Q_T = 0 \tag{4.18}$$

Where S_T represents the stored heat quantity [J/m³], $\underline{V}_T$ the heat flux [W/m²] and Q_T the volumetric heat source [W/m³].

Stored heat quantity per unit volume

The system enthalpy is defined as the sum of the contribution of each component of the system: $S_T = \sum H_i$ with, for a soil completely saturated:

$$H_w = n.\rho_w.c_{p,w}.(T - T_0) \tag{4.19}$$

$$H_s = (1-n).\rho_s.c_{p,s}.(T - T_0) \tag{4.20}$$

Heat transfer per unit volume

The term of heat transfer per unit volume is decomposed in a term of conduction and a term of convection.

$$V_T = \underbrace{\underline{i}_{cond}}_{conduction} + \underbrace{c_{p,w}.\rho_w.\underline{q}_w.(T - T_0)}_{convection} \tag{4.21}$$

The conduction is defined by the Fourier's law. The general Fourier's law is used to describe the conduction of heat in the medium. This law is expressed by:

$$\underline{i}_{cond} = -\underline{\underline{\lambda}}_m.\underline{\nabla}T \tag{4.22}$$

Where $\underline{\underline{\lambda}}_m$ is the anisotropic tensor of the conductivity of the medium. In a general form, this tensor has 9 components and is written:

$$\underline{\underline{\lambda}}_m = \begin{bmatrix} \lambda_{xx} & \lambda_{xy} & \lambda_{xz} \\ \lambda_{yx} & \lambda_{yy} & \lambda_{yz} \\ \lambda_{zx} & \lambda_{zy} & \lambda_{zz} \end{bmatrix} \tag{4.23}$$

In the same way as the Darcy' law, the Fourier' law for an isotropic material is:

$$\underline{i}_{cond} = -\lambda_m.\underline{\nabla}T \tag{4.24}$$

It exits some coupling between temperature and hydraulic flow. The liquid dynamic viscosity (μ_w [Pa.s]) depends on the temperature. This dependence is linear and is written:

$$\mu_w(T) = \mu_{w0} - \alpha_w.\mu_{w0}.(T - T_0) \tag{4.25}$$

where α_w is the liquid dynamic viscosity thermal coefficient [K^{-1}], T_0 is a reference temperature and μ_{w0} is liquid dynamic viscosity at reference temperature.

The density varies with temperature and the pressure according to the following relationship:

$$\rho_w(T, p_w) = \rho_{w0}.\left[1 + \frac{p_w - p_{w0}}{\chi_w} - \beta_w.(T - T_0)\right] \tag{4.26}$$

where β_w is the liquid volumetric thermal expansion coefficient [K^{-1}], $1/\chi_w$ is the liquid compressibility coefficient [MPa^{-1}], ρ_{w0} is the density at reference temperature and p_{w0} is a reference pore water pressure.

4.2 Parameters

Here are presented, in Table 5, Table 6 and Table 7, the thermo-hydro-mechanical characteristics of the Boom Clay. The properties are given for the initial temperature and pore pressure. The values of these parameters are indicative and may be different according the constitutive law used in this exercise.

Geomechanical characteristics		Boom Clay
Young elastic modulus [MPa]	E_0	300
Poisson ratio [-]	υ	0.125
Solid specific mass [kg/m³]	ρ_s	2682
cohesion [kPa]	c_0	300
Initial friction angle [°]	ϕ_{c0}	5
Final friction angle [°]	ϕ_{cf}	18
Hardening parameter [-]	β_c	0.01
Dilatancy angle [°]	ψ	0
Biot's coefficient [-]	b	1

Table 5: Geomechanical characteristics

Hydraulic characteristics		Boom Clay
Porosity [-]	n	0.39
Intrinsic permeability [m²]	k_{sat}^{int}	4.10^{-19}
Water specific mass [kg/m³]	ρ_w	1000
Fluid dynamic viscosity [Pa.s]	μ_{w0}	10^{-3}
Liquid compressibility coefficient [MPa^{-1}]	$1/\chi_w$	5.10^{-4}

Table 6: Hydraulic characteristics

Thermal characteristics		Boom Clay
Thermal conductivity [W/(mK)]	λ	1.35
Volumetric heat capacity [J m^{-3}.K^{-1}]	ρC_p	2.84 10^6
Linear medium thermal expansion coefficient [K^{-1}]	β	10^{-5}
Volumetric liquid thermal expansion coefficient [K^{-1}]	β_w	3.10^{-4}
Liquid dynamic viscosity thermal coefficient [K^{-1}]	α_w	0.01

Table 7: Thermal characteristics

The 3D modelling allows taking into account the anisotropy of the clay. The parameters for this case are given in Table 8. These parameters are given for an anisotropic elastic law. The considered anisotropic law is a transversely isotropic elastic law.

Anisotropic parameters		Boom Clay
Horizontal Young modulus [MPa]	E_h	700
Vertical Young modulus [MPa]	E_v	350
Shear modulus [MPa]	G_{vh}	140
Poisson's ratio in transversely isotropic material	ν_{hh}	0.25
Poisson's ratio in transversely isotropic material	ν_{vh}	0.125
Intrinsic horizontal permeability [m²]	k_h	4.10^{-19}
Intrinsic vertical permeability [m²]	k_v	2.10^{-19}
Vertical thermal conductivity [W/(mK)]	λ_v	1.25
Horizontal thermal conductivity [W/(mK)]	λ_h	1.7

Table 8: Thermo-hydro-mechanical parameters for the anisotropic cases

4.3 Initial conditions

The clay is initially considered as homogeneous and isotropic. It is supposed to be fully saturated. Initial conditions are listed in Table 9. For Boom Clay, they are close to the ones encountered in the clay formation. The gravity will not be considered in this modelling. These initial conditions are the same for the three models.

Initial state		Boom Clay
Total stresses [MPa]	$\sigma_x=\sigma_y=\sigma_z$	4.5
Pore pressure [MPa]	p_{w0}	2.25
Temperature [°C]	T_0	16.5

Table 9: Initial state – stresses, pore water pressure and temperature

4.4 Geometry

4.4.1 Description of the 1D axisymmetric model

The first model is a 1D axisymmetric model which is the easiest model to realise. This model rapidly permits to have an overview of the physics implied in this modelling. But this model has some limitations concerning the dissipation of heat in the medium. As a consequence, the temperature obtained using this model will be overestimated in comparison with the 2D and the 3D modelling. Another limitation of this model concerns the drainage. Indeed, the drainage only occurs radially in the 1D while there is an axial component of the drainage in the 2D model.

Geometry

The geometry of the 1D axisymmetric model consists in a one-dimensional problem (radial-axisymmetric) and is described in Figure 30. The inner and the external radius are respectively equal to 0.095 m and 100 m. The inner radius corresponds to the radius of the borehole equipped with heaters.

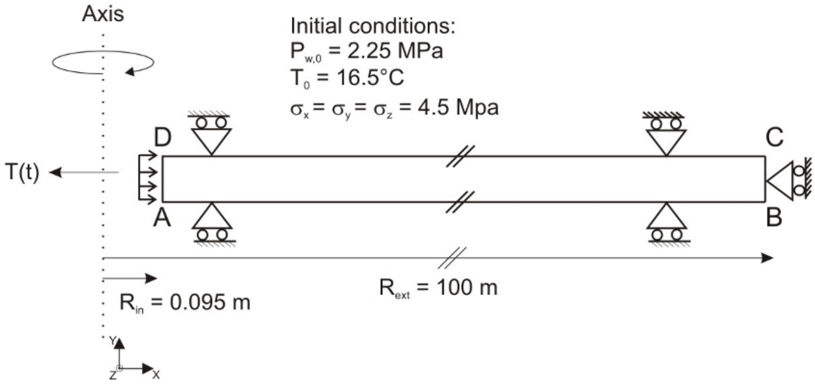

Figure 32: Illustration of the geometry of the 1D modelling

Boundary conditions

The boundary conditions for the 1D modelling are illustrated in Figure 31.

Mechanical boundary conditions are imposed such as:

- Vertical displacements are fixed on boundaries AB and DC;
- Horizontal displacements are fixed on boundaries AD and CB.

Hydraulic boundary conditions are imposed such as:

- Boundaries AD, AB and DC are impervious;
- Pore water pressure is fixed on CB.

Thermal boundary conditions are imposed such as:

- Boundaries DC, CB and AB are adiabatic;
- Heat flux is imposed on boundary AD following the experimental procedure described in section 3.1 and in section 4.

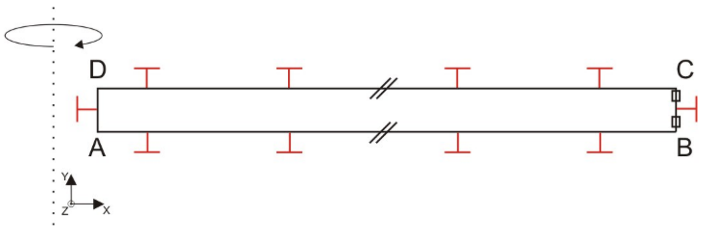

Figure 33: Boundary conditions considered in the modelling

4.4.2 Description of the 2D axisymmetric model

This section describes especially the geometry and the boundary conditions of the 2D modelling. Initial conditions, constitutive laws and parameters are the same as the 1D model.

Geometry

This section describes the geometry of the modelling for the 2D axisymmetric condition. The axis of symmetry corresponds to the axis of the main borehole equipped with heaters. This model is 100 m wide and 119 m high. Figure 32 illustrates the 2D axisymmetric model.

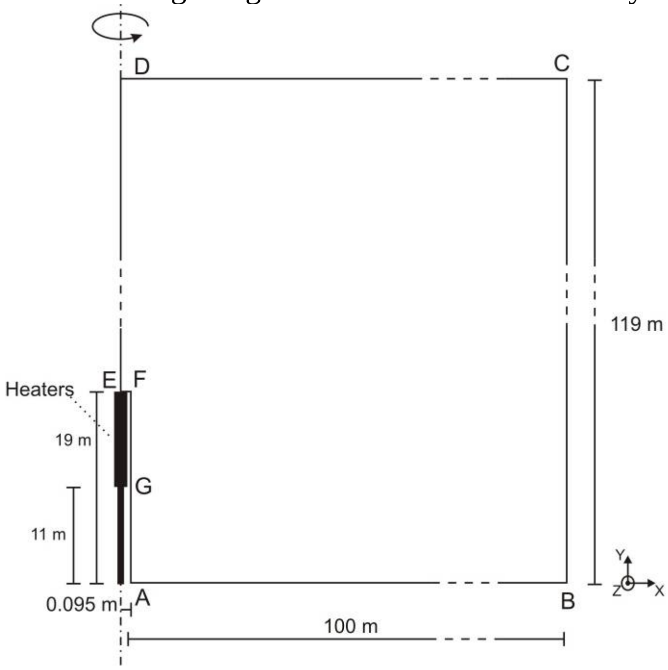

Figure 34: Schematic representation of the 2D axisymmetric modelling

Boundary conditions

Figure 33 represents the boundary conditions used in this 2D modelling.

Mechanical boundary conditions are defined as followed:

- Axial displacements are fixed on the external boundaries DC, AB and EF;
- Radial displacements are fixed on the boundaries ED, BC and AF.

Hydraulic boundary conditions:

- Pore water pressure are fixed on the boundaries DC, CB;
- Boundary from the point A to point D is impervious. The boundary AB is also impervious.

Thermal boundary conditions:

- Boundaries AB, BC, CD, DE and FA are adiabatic;

- Heat flux is imposed on boundary FG.

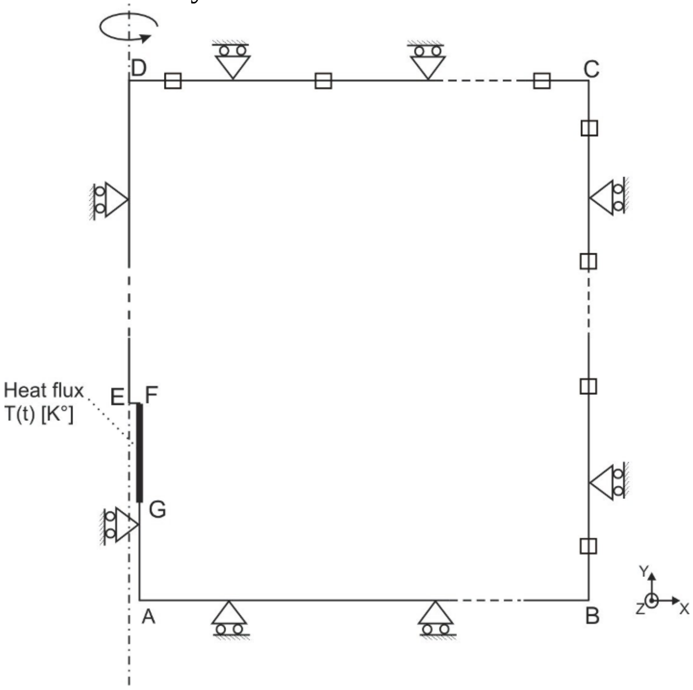

Figure 35: Schematic representation of the boundary conditions in the 2D axisymmetric modelling

4.4.3 Description of the 3D model

This section describes the 3D model used in this exercise. This section will present the geometry and the boundary conditions.

Geometry

The geometry of the 3D model is described in Figure 34. The model has a height of 100m, a width of 100 m and a depth of 119 m. The main borehole equipped with heaters is also modelled.

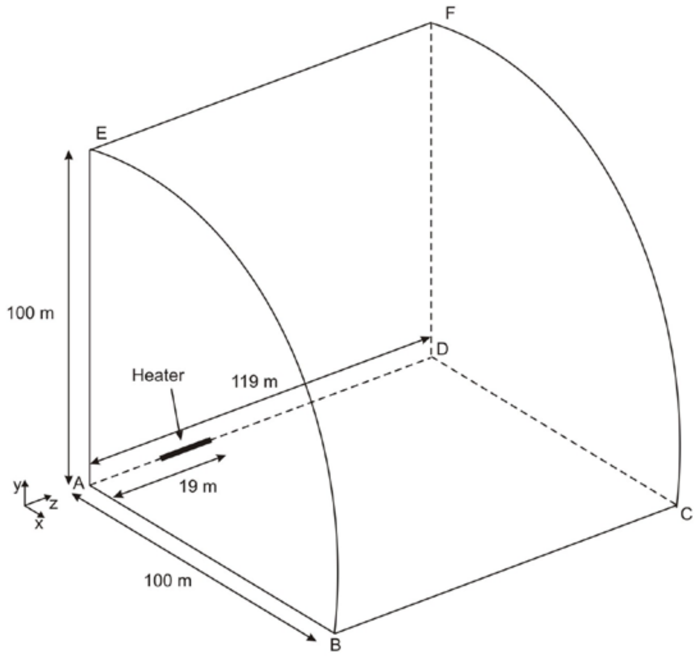

Figure 36: Geometry of the 3D model

Boundary conditions

The boundary conditions are the following:

Mechanical boundary conditions are defined as followed:

- Displacements according Z axis are fixed on the external boundaries ABE and DCF;
- Displacements according X axis are fixed on the boundaries ADFE and BCFE;
- Displacements according Y axis are fixed on the boundaries ABCD and BCFE;
- Radial displacements are fixed on the inner surface of the borehole.

Hydraulic boundary conditions:

- Pore water pressure are fixed on the boundaries BCFE and DCF;
- Boundaries ABE, ABCD, ADFE are considered impervious;
- Boundary at the inner surface of the borehole is impervious.

Thermal boundary conditions:

- All boundaries are supposed to be adiabatic except for the heater where a heat flux is imposed according to the experiment procedure.

5 General form of numerical results

This section presents the results. In a first phase, we will present the 1D results to explain the physical phenomena related to this experiment. The second phase will concern the 2D results. A brief comparison between the 1D and the 2D model will follow. Then a presentation of the 3D results will be realised, for which all the sources of anisotropy were considered.

Profiles of temperature pore water pressure and stresses will be present respectively at 4, 54, 125, 250 and 450 days. Figure 35 presents the different times where the profiles will be analysed.

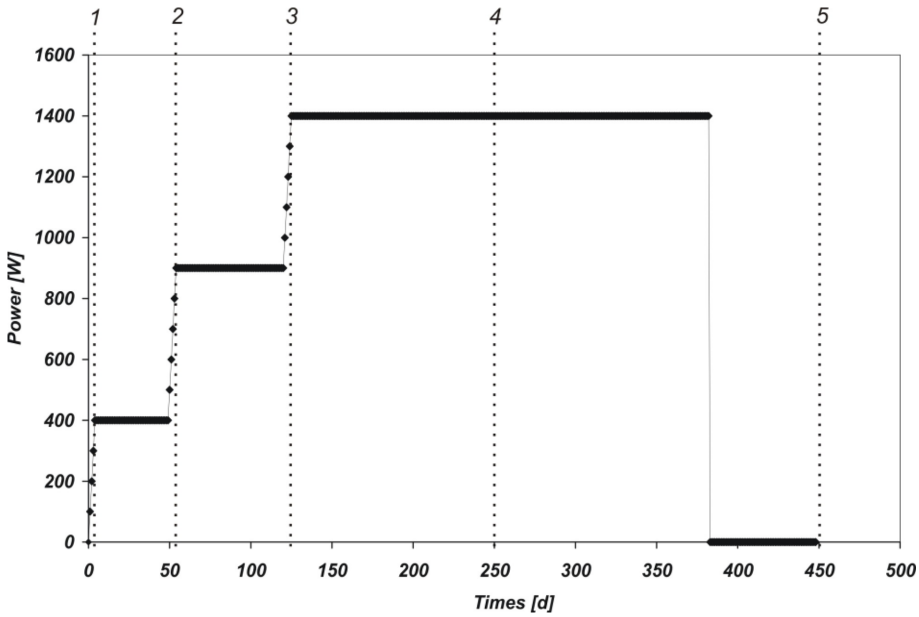

Figure 37: Times where the results are analysed

5.1 1D results

Figure 36 represents the evolution of the pore water pressure and the temperature with time. Remember that the modelling is composed in 4 major steps. The power of the heater is increased in 3 phases. After each increase, the power is maintained constant. Figure 36 shows that a maximum of 100 °C at the inner radius is attained at the end of the third heating phase. Finally, when the heater is switched off, the temperature quickly decreases.

The evolution of the pore water pressure is related to the increase of volume due to thermal effect. Indeed, when the temperature increases, the volume of water expands which induces an increase of the pressure. When the power is maintained constant, the pore water pressure is quiet stabilised. Finally, a decrease of pore pressure is observed during the cooling phase.

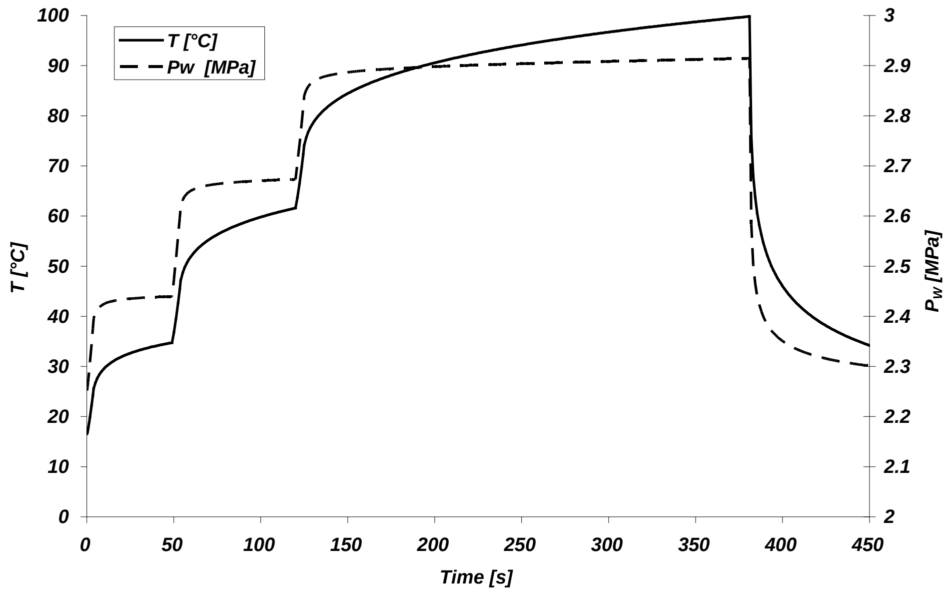

Figure 38: Evolution of the temperature and the pore water pressure at the inner cavity

Figure 37 presents numerical evolution of the temperature, for different thermocouples, in the medium due to the increasing power. The different sensors are located at different distances from the heater. The nearest (AT93E) has the higher temperature and the farthest (AT98E5) has the lower temperature.

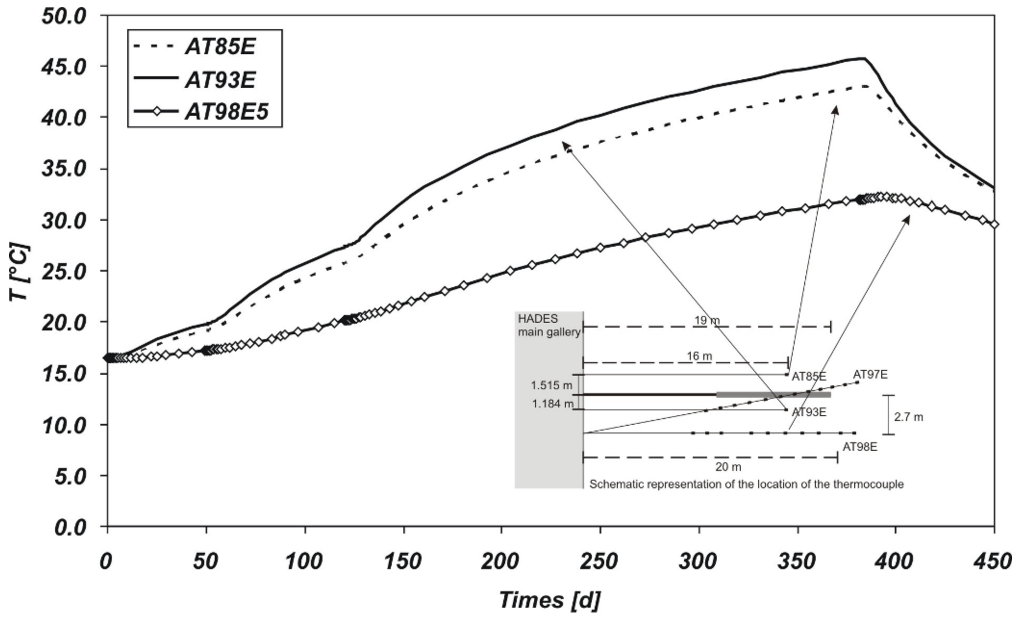

Figure 39: Numerical temperature evolution for different sensors

Figure 38 illustrates the pore water evolution for three sensors. As explained previously, an excess pore water pressure is generated during the heating. This excess pore pressure is all more important as the sensor is close from the heater (AT93E in comparison with AT98E2).

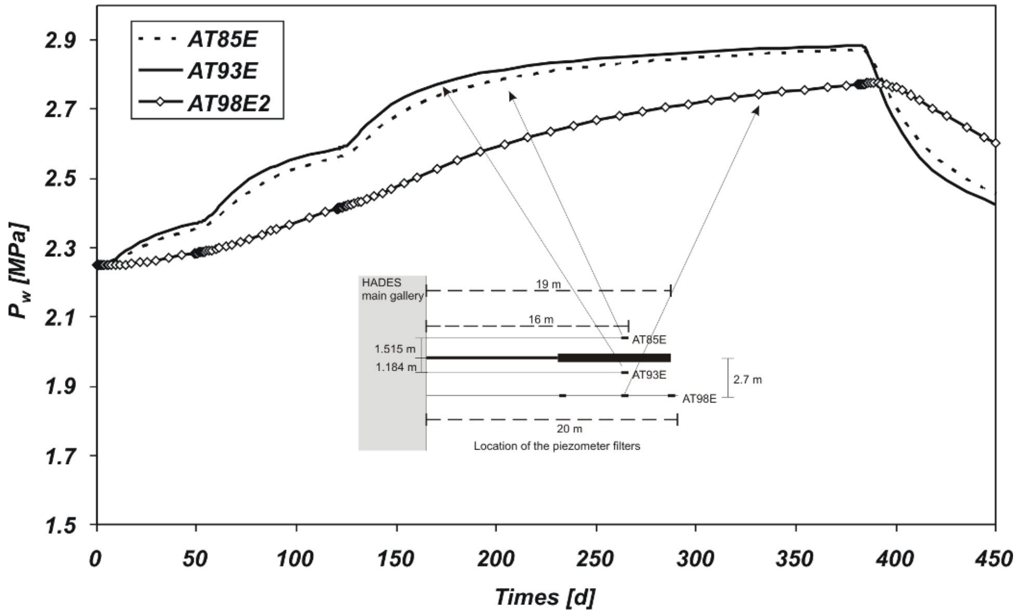

Figure 40: Numerical pore water pressure evolution for different sensors

Results along radial profiles

Figure 39 presents the radial profiles of temperature at different times of the experiment. The heat generated by the increase of the power dissipates in the medium. As a consequence the temperature increases around the cavity during all the three phases of heating. The zone affected by the temperature increases during the experiment due to the dissipation of the heat. The profiles at 4, 54, 125 and 250 days characterise this evolution of the temperature in the medium. When the power is switched off, the temperature at the cavity decreases but dissipation of the heat goes on and the temperature continues to increase in the far field (profile at 450 days).

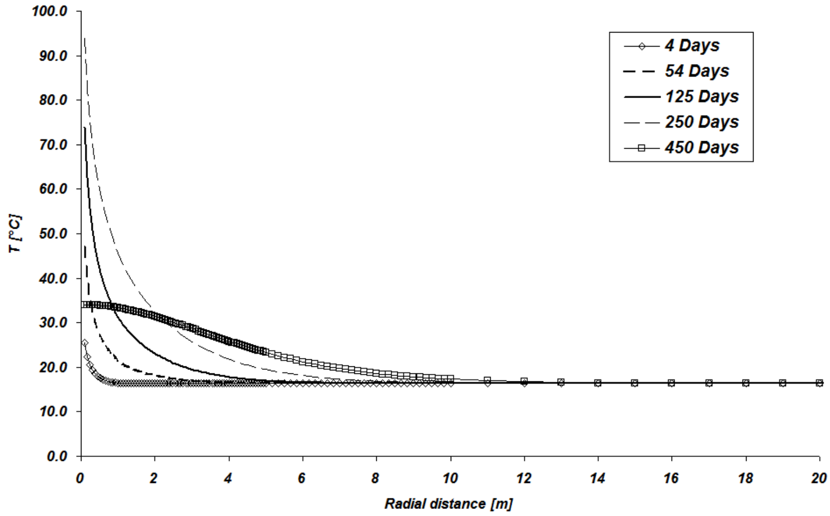

Figure 41: Evolution of the radial profiles of temperature

The evolution of the pore water pressure with the radial distance is described in Figure 40. As explained previously, the increase of the temperature induces an expansion of the volume of the water which is more important than the dilation of the solid (three times greater). Due to this differential dilation, the pore water increases in the medium. This rise in pressure is linked with the permeability of the medium. If the permeability of the porous medium is high, the excess pore water pressure induced by an increase of temperature will be rapidly dissipated. Figure 40 shows the pore water pressure increases around the cavity during the heating phase (profiles at 4, 54, 125 and 250 days). On the contrary, the reduction of the temperature induces a decrease of the pore pressure near the cavity (profile at 450 days). But due to the dissipation of the heat, during the cooling phase, explained previously, the pore water pressure continues to increase in the far field.

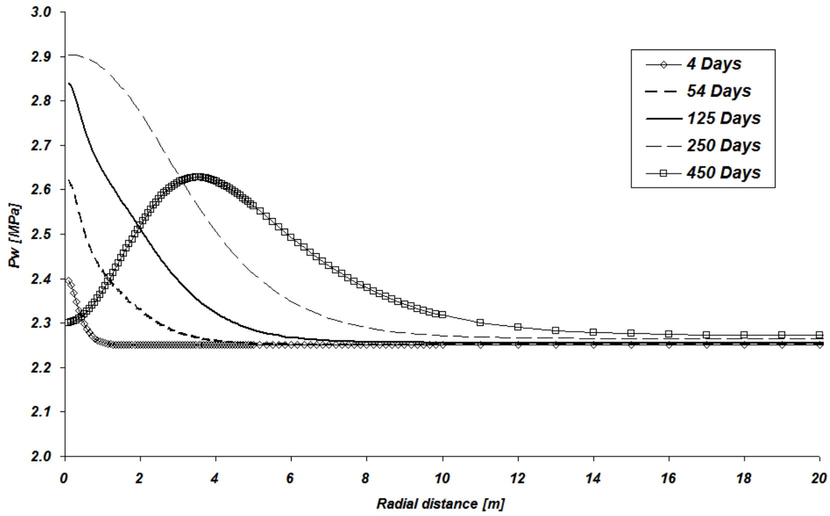

Figure 42: Evolution of the radial profiles of pore water pressure for various times

Figure 41 represents the evolution of the radial effective stress with the radial distance. During the heating phase, the rise in pore water pressure induces a decrease of the effective stress (Figure 36) in accordance with the Terzaghi's principle. When the power is switched off, the pore water pressure decreases near the cavity but continues to increase in the far field. Due to this phenomena, the stress increases near the cavity but decreases in the far field.

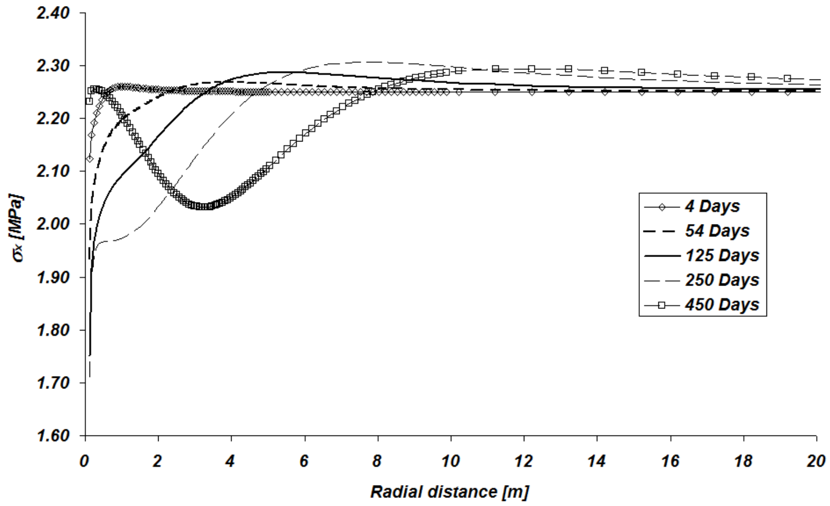

Figure 43: Evolution of the radial effective stress with the radial distance for various times

When the soil is heated, the expansion of the solid skeleton induces radial displacements in the medium towards the external boundaries. Figure 42 represents the evolution of the radial displacements with time. The radial displacements increase during all the experiment even during the cooling phase due to the dissipation of heat.

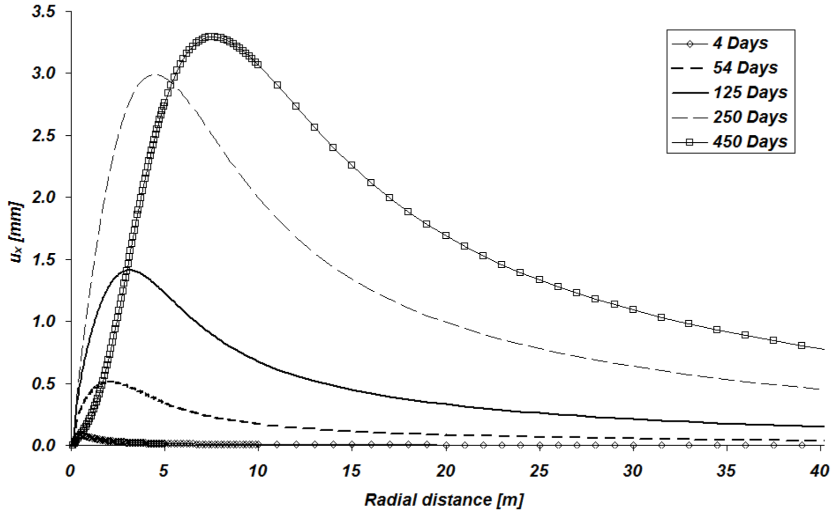

Figure 44: Evolution of radial displacements for different times in the 1D modelling

5.2 2D results

This section presents results in the 2D modelling. Firstly, we will see results along a radial profile which crosses the heater at its middle (profile 1 in Figure 43). Secondly, the evolution of the heat, the stresses and the pore pressure will be present along a profile which is parallel to the heater (profile 2 in Figure 43).

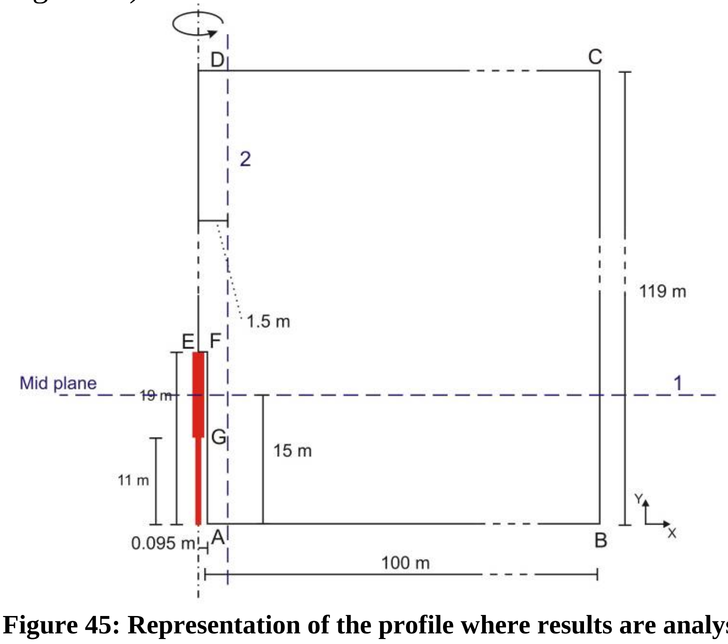

Figure 45: Representation of the profile where results are analysed

Results along radial profiles

Figure 44 represents the evolution of the temperature according to a profile perpendicular to the heater for various times. The same conclusion as previously in 1D modelling can be done. The increasing power induces an increase of the temperature whereas a decrease is observed during the cooling phase when the heater is switch off. At the end of the cooling phase, the dissipation of the heat continues and the temperature increases in the far field.

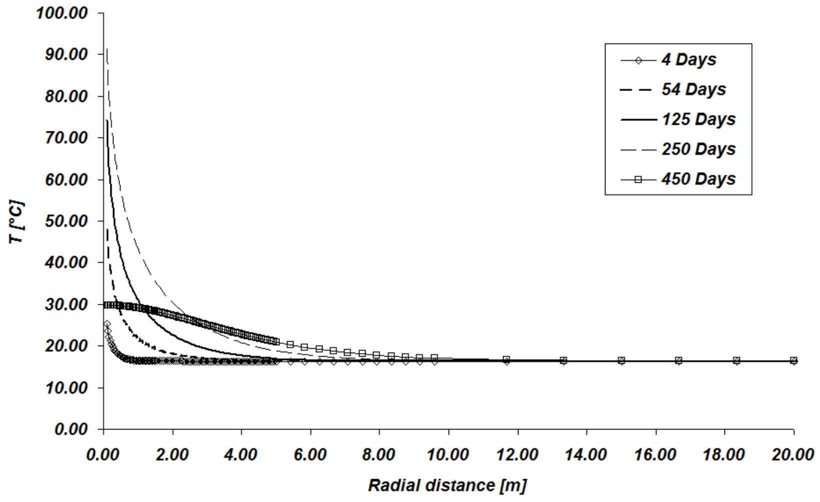

Figure 46: Radial profiles of the evolution of the temperature

The evolution of the pore water pressure is analogous to the results obtained in the 1D modelling and may be seen in Figure 45. But, on the contrary of the 1D case, at the end of the modelling the pore water pressure reaches a value lower than the initial value. This effect is related with the drainage which has two components in 2D. Actually, the drainage can be axial or radial unlike in the 1D where the component of the drainage is radial. The excess pore water pressure induces by the temperature is more or less the same in 2D and in 1D. But, in 2D, the axial drainage reduces the excess pore pressure. So, when the temperature decreases, the pore water pressure decreases in the same proportion of its increase. As a consequence, the pore water pressure becomes lower as its initial value.

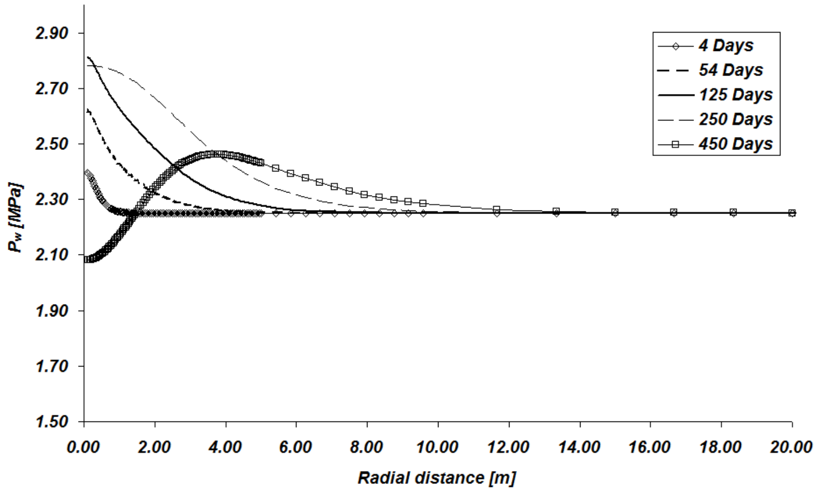

Figure 47: Evolution of the pore water pressure as a function of the radial distance from the heater

Figure 46 presents the evolution of the radial displacements induced by the temperature variation. At the end of the modelling, negative values of radial displacements are obtained. This can be explained by the axial dilation which produces a radial contraction at the end of the modelling. Indeed, the heat continues to be dissipated during the cooling phase producing an increase of the axial displacement.

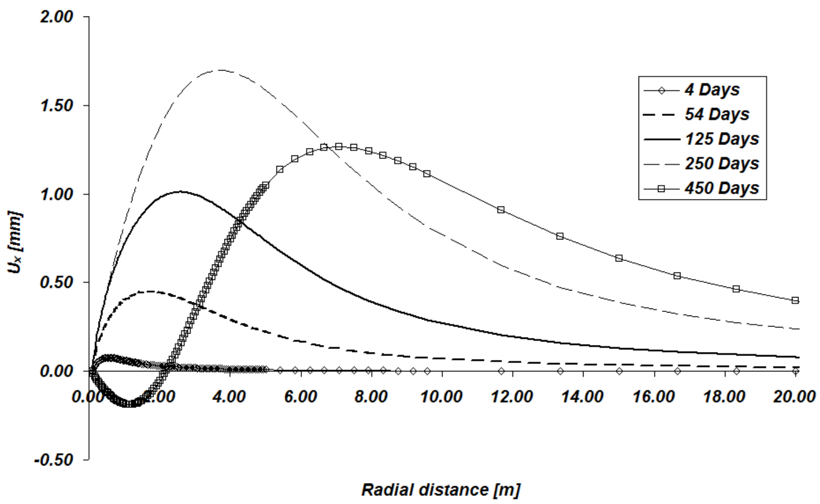

Figure 48: Evolution of the radial displacements with the radial distance

Figure 47 presents the evolution of the axial displacement with the radial distance. During the heating phase, the displacements increase due to the dilation of the solid. This evolution goes on during the cooling phase. This increase during the cooling phase is due to the dissipation of heat as explained in the 1D modelling. If the model was symmetric, that is to say that the centre of the heater was located at the middle of the model, no axial displacements would have been observed along this profile.

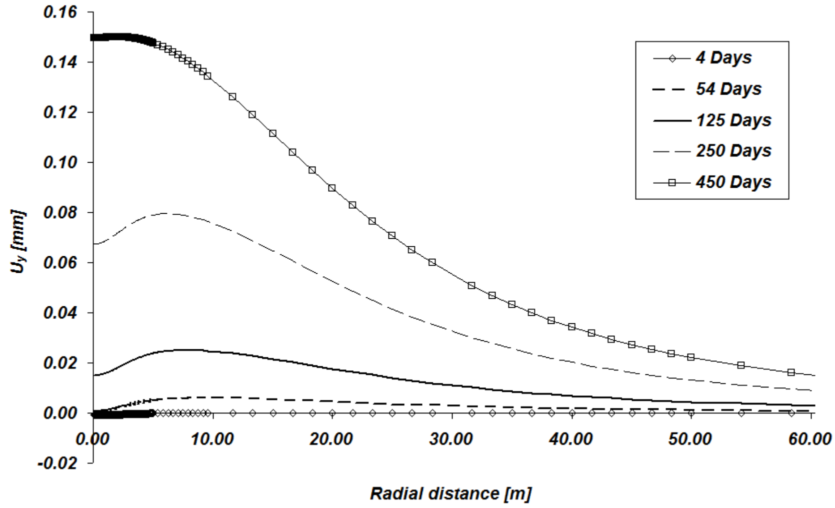

Figure 49: Evolution of the axial displacements with the radial distance

Results along axial profiles

This part will present results along a profile parallel to the heater (profile 2 in Figure 43). Figure 48 presents the evolution of the temperature along this profile. This figure illustrates the fact that in this model, the dissipation of the heat can also occur in the axial direction. The same conclusions as the radial profiles may be observed. An increase of the power induces higher temperature in the model. A decrease of the power reduces the temperature in the central part of the heater, but temperature still increases laterally due to the dissipation of heat.

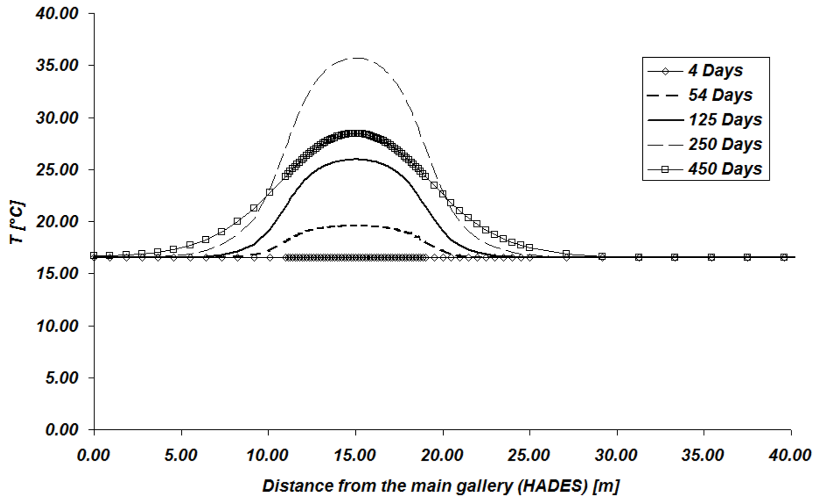

Figure 50: Evolution of the temperature according a profile parallel to the heater

Figure 49 shows the evolution of the pore water pressure during the calculation. The same phenomenon as seen previously may be observed. Firstly, an increase of the temperature induces an expansion of the volume of water which increases the pore pressure. Secondly, the cooling phase generates a diminution of the pressure but pore pressure increases laterally due to the dissipation of the heat.

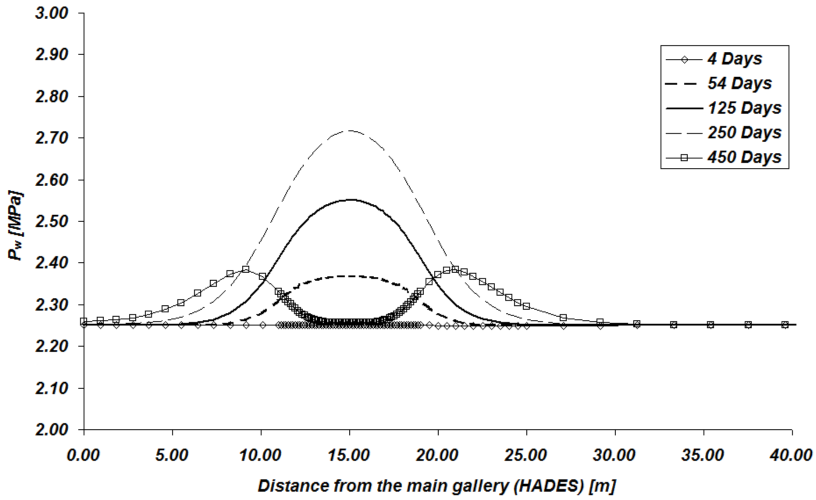

Figure 51: Evolution of pore water pressure following an axial profile

Figure 50 illustrates the evolution of the radial displacements. The same conclusion as in the first profile can be done. Heating produces displacements towards the external boundaries of the model. As explained previously, the negative values of radial displacements appear at the end of the modelling.

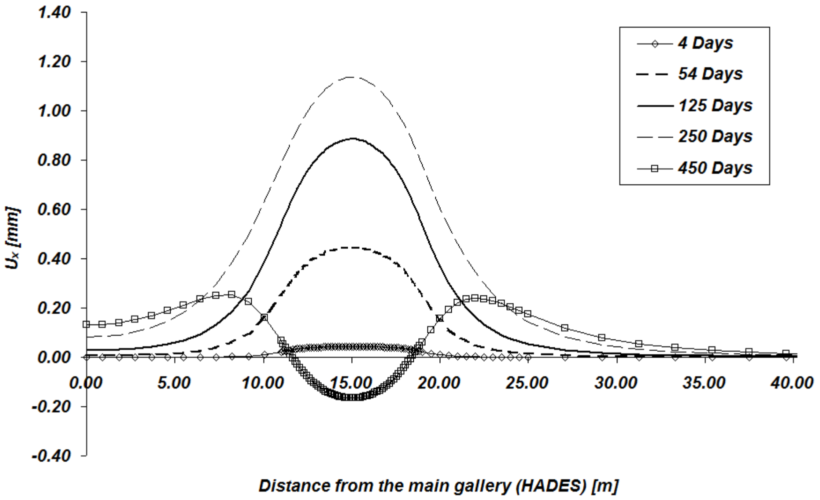

Figure 52: Evolution of the radial displacements according the second profile

Figure 51 illustrates the evolution of the axial displacements for different times. The solid expands in all the directions of the space. The dilation of the solid appears in the axial and in the radial directions. So, the solid tends to move towards the external boundaries of the model that is to say in the opposite direction of the heater. If the model was symmetric, this profile would have been antimetric.

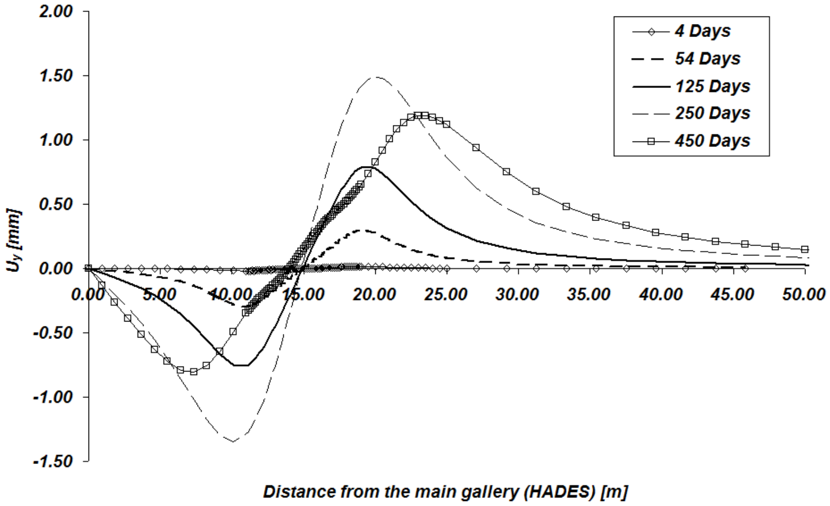

Figure 53: Evolution of the axial displacements along the axial profile

COMPARISONS BETWEEN 1D AND 2D

At the difference to the 1D modelling, the dissipation of the heat in the 2D model can occur in 2 directions whereas this dissipation concerns only one direction in 1D modelling. In order to highlight these differences, results will be presented according to the evolution of pressure and temperature at a point in AT93E. This borehole is in the same horizontal plane as the heater.

The difference might be observed in Figure 52 which represents the evolution of the temperature for this point in both cases. A higher temperature is reached with the 1D modelling. This difference is explained by the different dissipation of heat occurring in each model. We also see that the behaviour is the same in the short term for the 2 modellings but differ in the long term.

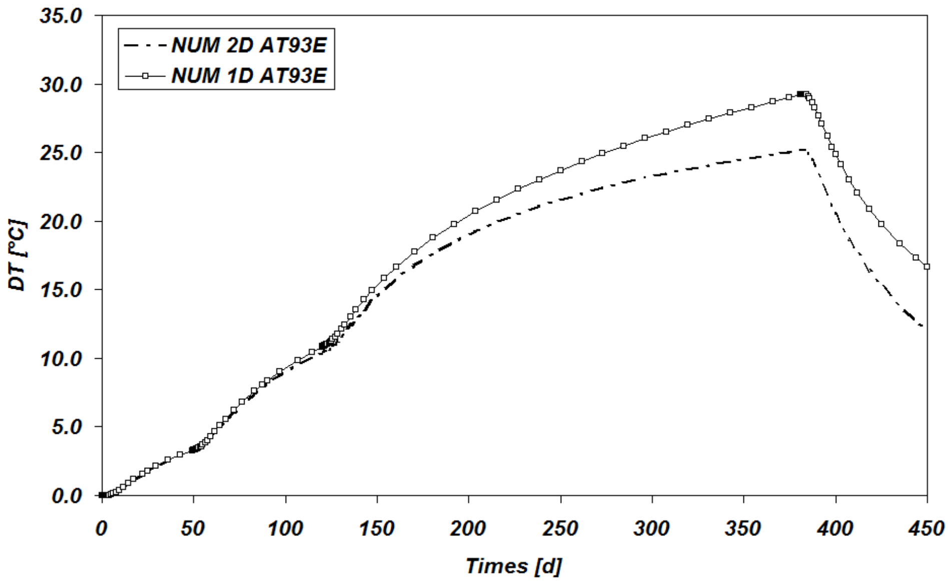

Figure 54: Evolution of temperature with time for a point located in the boreholes AT93E for the 2 modellings

Another difference is observed in the evolution of the pore water pressure at the same experimental point. The same conclusion as in Figure 53 can be done. Due to this difference of dissipation, the greater temperature in the 1D model induces a more important pore water pressure than in the 2D model. Moreover, the pore pressure seems to decrease during the third heating phase in the 2D. This reduction of the excess pore pressure is due to drainage which occurs radially and axially in the 2D model. As a consequence, the excess pore water pressure is dissipated during the heating phase. This effect may be called thermal consolidation.

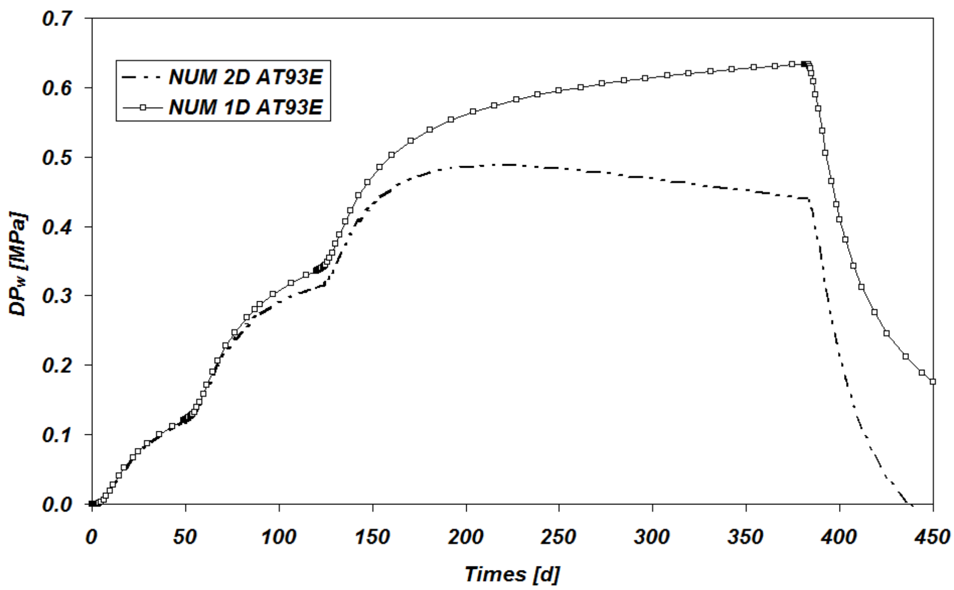

Figure 55: Evolution of pore water pressure with time for a point located in the boreholes AT93E for the 2 modellings

Figure 54 illustrates the difference in the radial profile between the 1D modelling and the 2D modelling. We have seen that the 1D modelling is very simple to realise but present some disadvantages. Indeed, the temperature is overestimated in the long term behaviour as shown in this figure. On the contrary, in the short term behaviour, the results are the same for the both models.

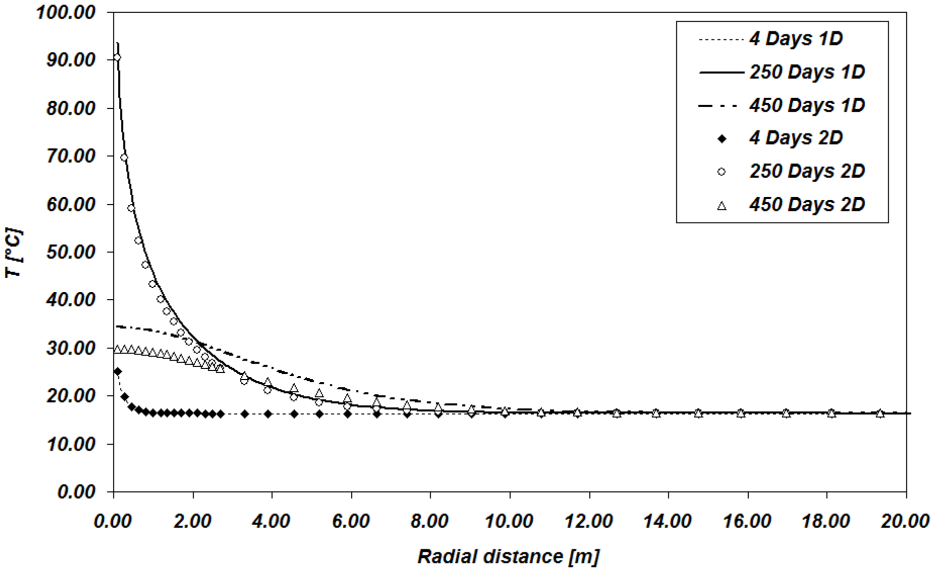

Figure 56: Comparison between the evolutions of the radial profiles of the temperature for the 2 models

COMPARISON WITH EXPERIMENTAL RESULTS

This section presents some comparisons between experimental and predicted data. Figure 55 presents a comparison of the temperature changes for the 1D and the 2D calculation. We show that the temperature increase is quite similar between the 2D and the experimental results.

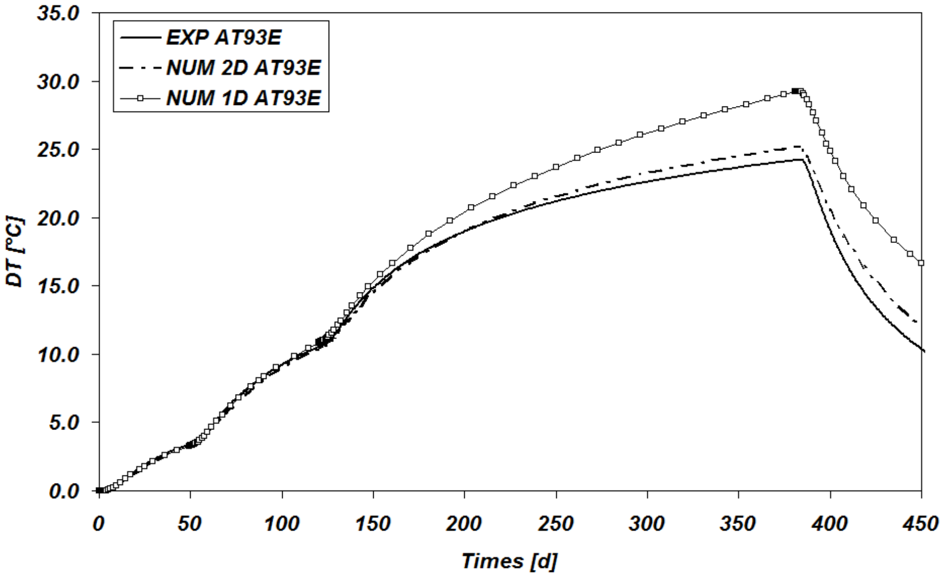

Figure 57: Comparison between the experimental results and the numerical results for the sensor located in the boreholes AT93E

As explained previously, the evolution of temperature is overestimated considering the 1D modelling. So, in the next paragraphs, we will focus on the evolution of temperature with the 2D modelling.

In 2D, the comparisons between the temperature evolution recorded and the numerical results show good agreement for some sensors in the horizontal plane. An example of this comparison is realised in Figure 56 which compares the numerical and the experimental evolution of the temperature for AT85E and AT93E.

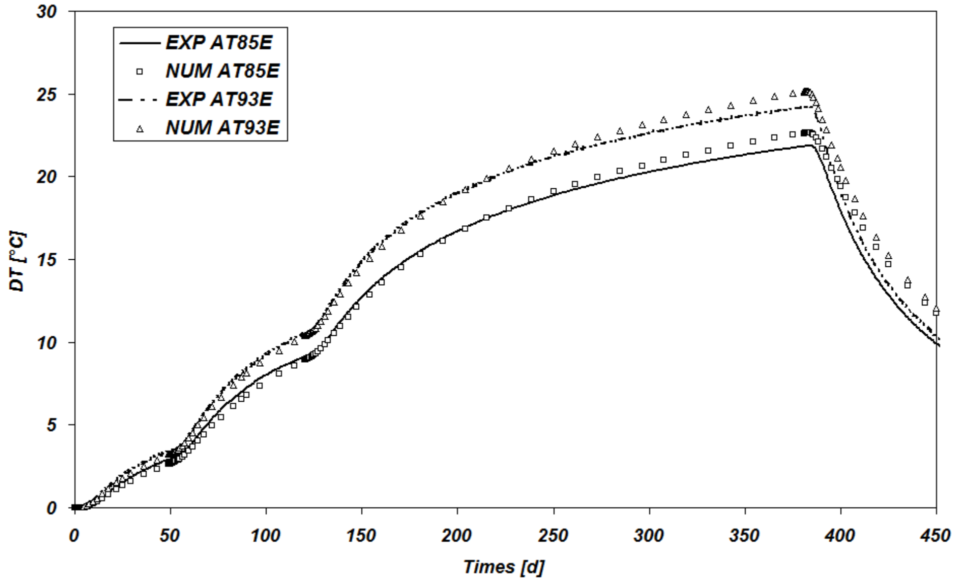

Figure 58: Comparison between the numerical evolution of the temperature and the recorded temperature for sensors AT85E and AT93E

Figure 57 presents a comparison between the experimental and numerical results for sensors located in AT98E. As mentioned previously, this borehole is in the same horizontal plane as the heater. The numerical results seem quiet good for AT98E5 and AT98E10. But for the two others, this is not the case.

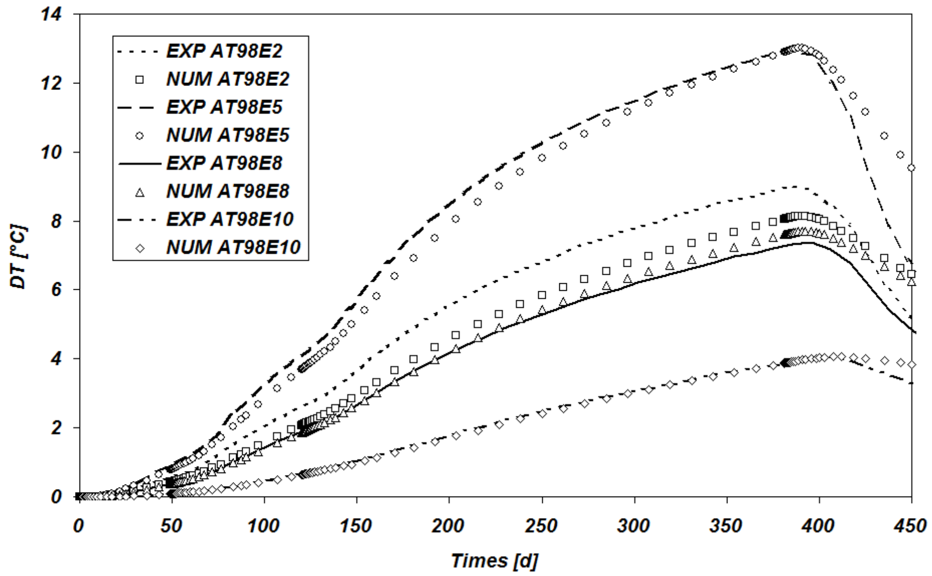

Figure 59: Comparison between experimental results and numerical results for sensors in the borehole AT98E

Figure 58 presents a comparison between the temperature recorded and the numerical results for some sensors of AT97E. This borehole is inclined compared with the horizontal plane. The result of this comparison shows that all the numerical results do not fit the experimental curves.

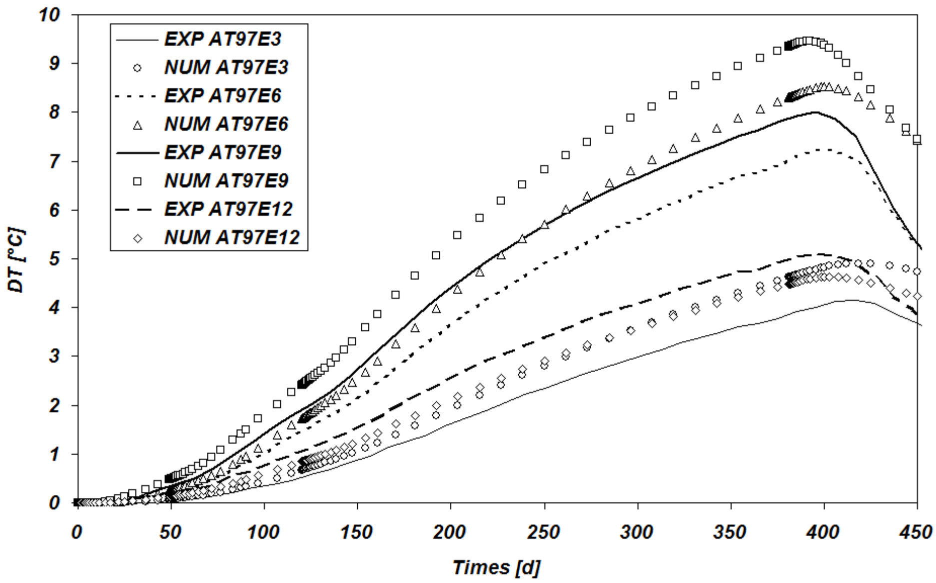

Figure 60: Comparison between experimental results and numerical results for sensors in the borehole AT97E

The evolution of the pore water pressure is different between modelling and experiment. Figure 59 presents the comparison between the experiment and the modelling. In both case, we see that the evolution of the pore pressure is underestimated.

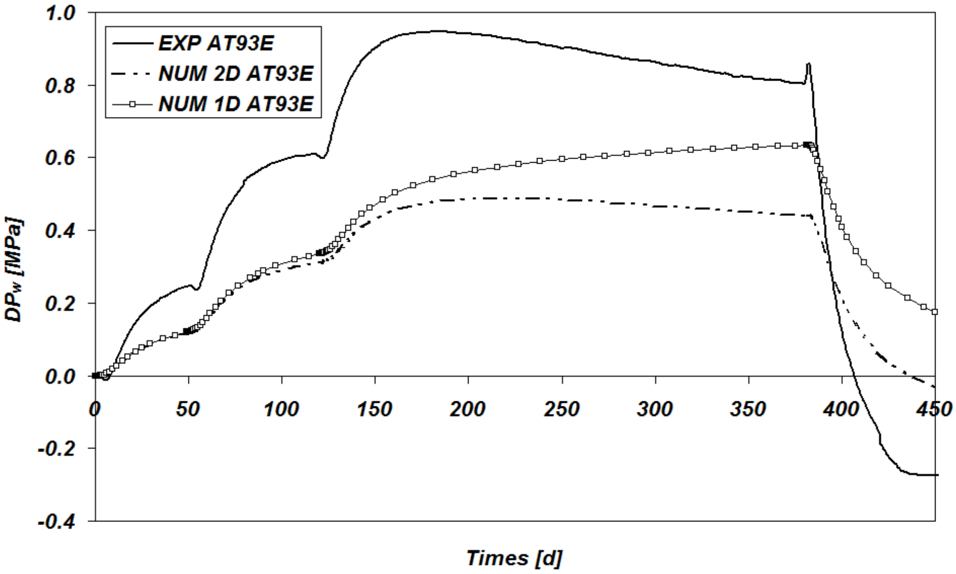

Figure 61: Comparison of the evolution of the incremental pore water pressure between experimental and numerical results

5.3 3D results

This section presents the results obtained with the 3D modelling considering mechanical, hydraulical and thermal anisotropy. The physics of the problem have been already discussed during the presentation of the results of 1D and 2D model. We will focus on the changes of pore water pressure and temperature.

Figure 60 presents the different profiles where the results are analysed. Two profiles (1and 2) are situated in the horizontal plane and two others profiles are in the vertical plane.

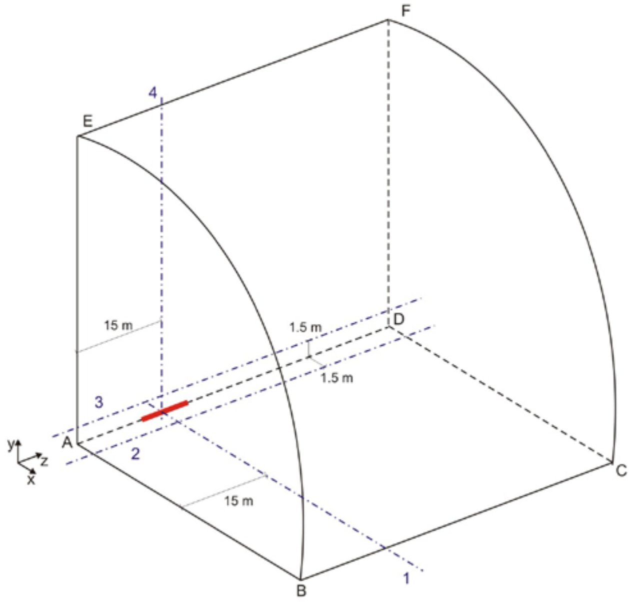

Figure 62: Presentation of the profiles where results are provided

The temporal evolution of one sensor will be also given. This sensor is AT85E and is located in the same horizontal plane as the heater. Figure 61 illustrates the position of the sensor next to the heaters.

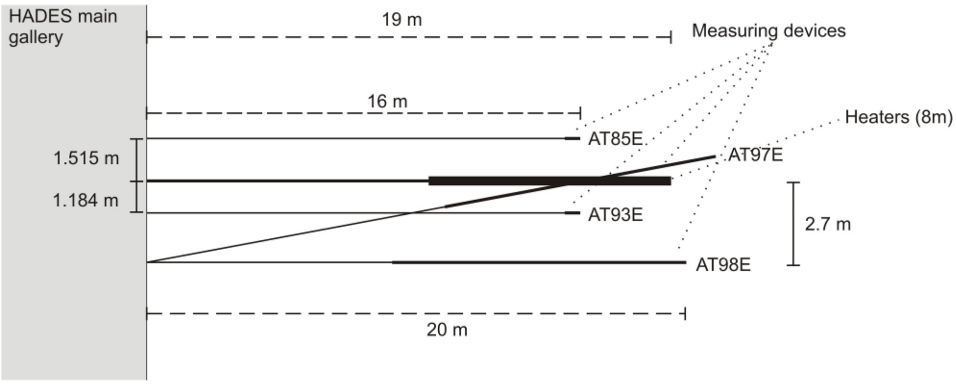

Figure 63: Position of the sensor where the results are discussed

The effect of the different anisotropy is to generate different results according the direction in term of pore water pressure and thermal dissipation. As example, Figure 62 presents a comparison of the distribution of the pore water pressure according the profile 1 and profile 4. This comparison shows difference of pore water pressure in the far field due to difference in pore water pressure dissipation due the combination of the anisotropy effect.

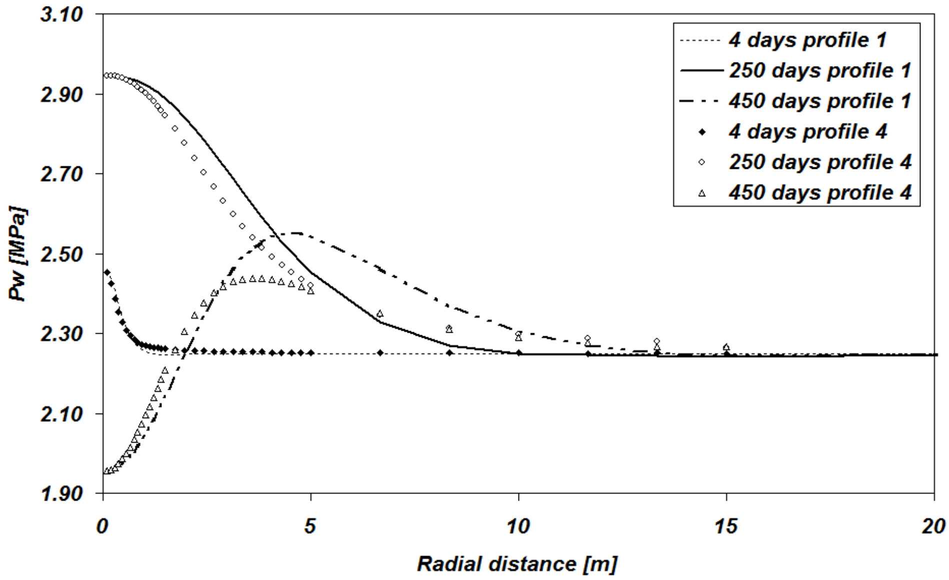

Figure 64: Distribution of pore water pressure according profile 1 and profile 4

Figure 63 presents the spatial distribution of the temperature at different times for the profile 1 and the profile 4. Due to the difference of thermal dissipation, the temperature is greater in the far field for the profile 4 as compared to profile 1.

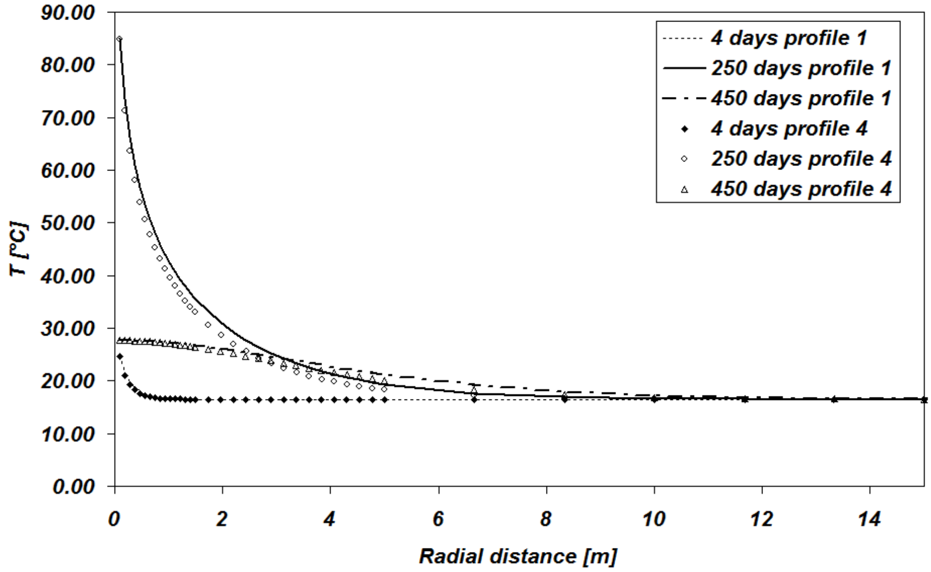

Figure 65: Distribution of the temperature according profile 1 and profile 4

As compared to isotropic case, the effect of all this anisotropy is to generate higher pore water pressure than in the isotropic case. This higher excess pore water pressure is due to a combination of all the phenomena explained previously. Figure 64 shows the difference obtained for the pore water pressure evolution at AT85E between this anisotropic case and the isotropic case.

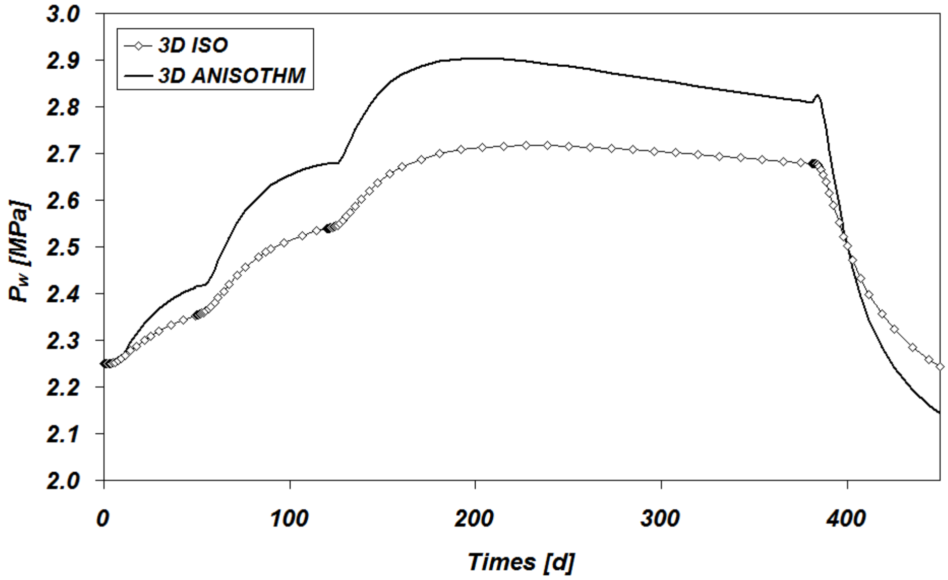

Figure 66: Evolution of the pore water pressure in the full anisotropic model and in the isotropic model at AT85E

Comparisons with experimental data

The comparisons with the experimental have been realised and the results are given in this section.

A comparison between the evolutions of the temperature for the different sensors has been realised. Figure 65 shows a comparison between numerical and experimental data for two sensors (AT85E and AT93E). The comparison is very good for these two sensors.

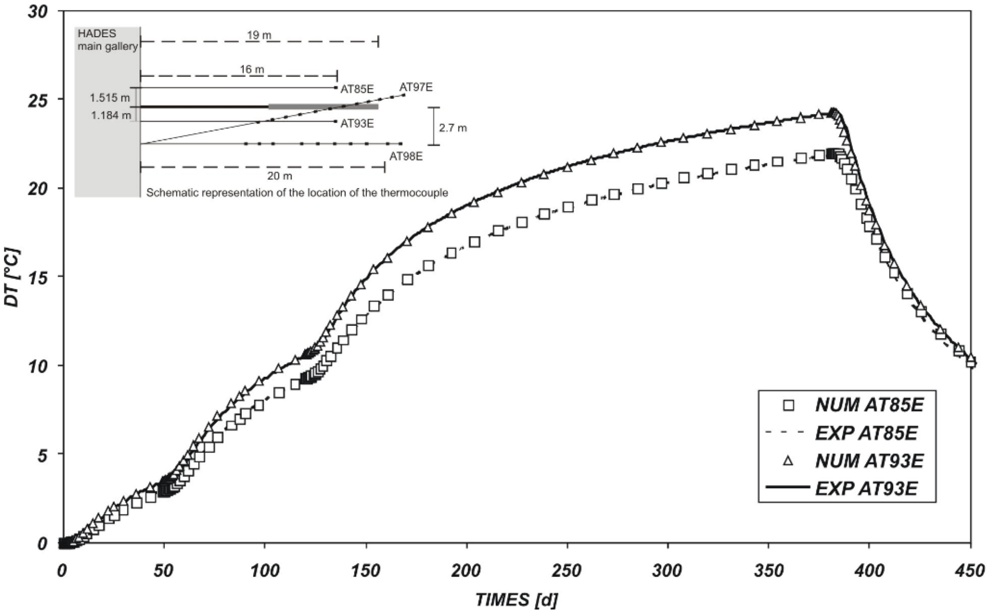

Figure 67: Comparison between the experimental and numerical data for AT85E and AT93E

Figure 66 presents a comparison between the experimental data and the numerical results for the sensor AT97E. We can observe that the comparison between experimental and numerical results is quiet good for these sensors. The anisotropic parameters of the thermal conductivity permits to better reproduce the observed evolution as compared with the isotropic case (Figure 58).

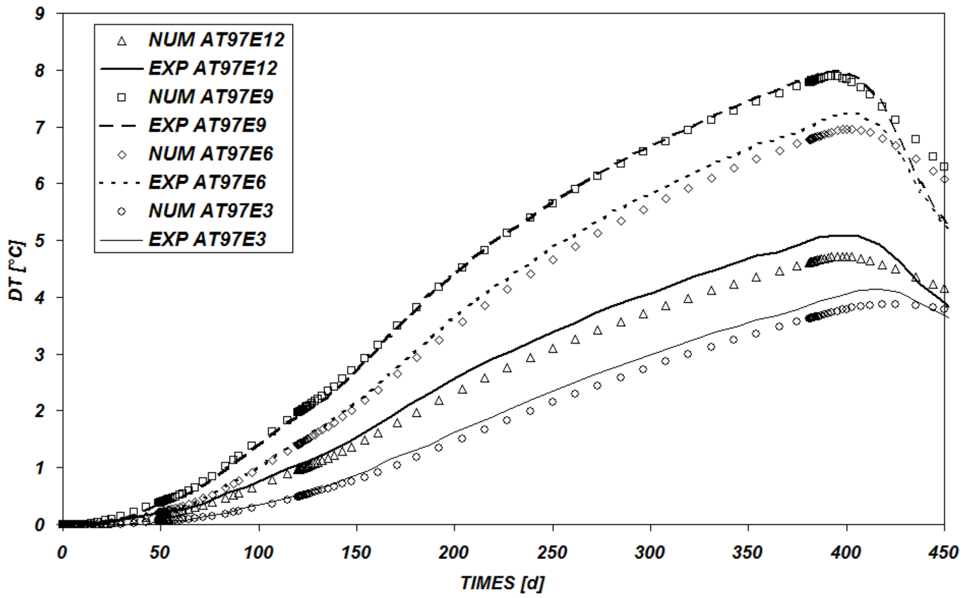

Figure 68: Comparison between the experimental and the numerical data for some sensors of AT97E

Figure 67 presents a comparison of thermal evolution for the sensors of AT98E10. The numerical results are good except for AT98E10 and AT98E5. There is a slight difference between the numerical and the experimental evolution of the AT98E2 and AT98E8.

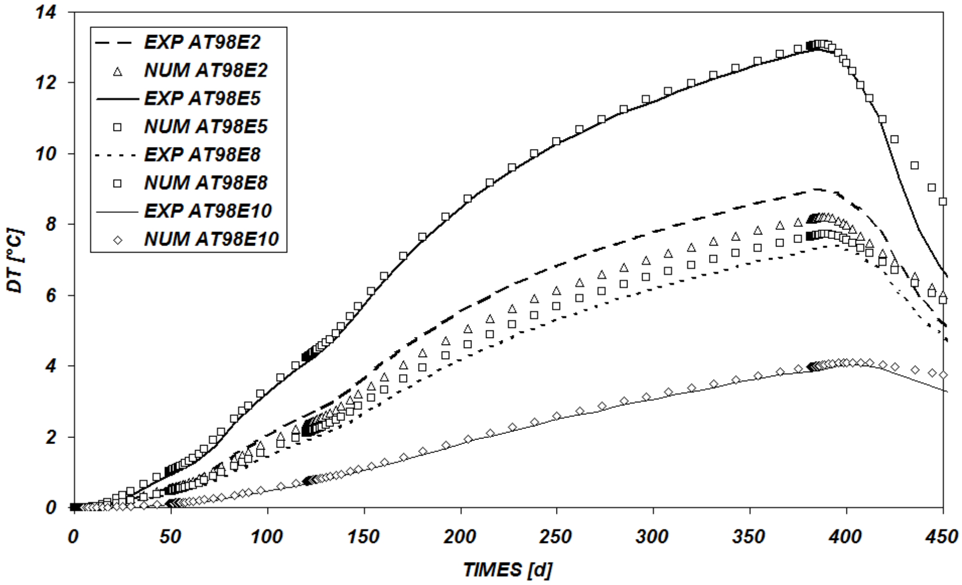

Figure 69: Comparison between the numerical and the experimental results

Concerning the evolution of the pore water pressure, the shape is the same but the numerical results underestimate the observed evolution. This comparison is done in Figure 68 for the sensors AT85E and AT93E. We can observe that the evolution of the pore water pressure is very underestimate. The same conclusion is done for the piezometers located in the borehole AT98.

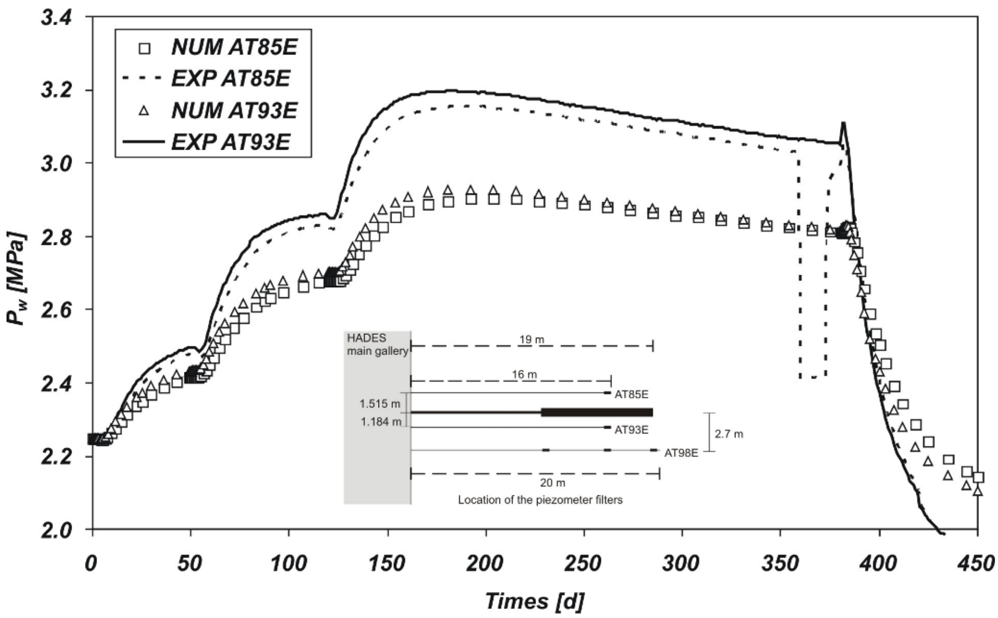

Figure 70: Comparison of the observed excess pore water pressure and the numerical result

6 Comparison of the results from the different teams

This section deals with the comparisons between all the partners who have realised this benchmark. Table 10 summarises the teams who have realised this benchmark and which modelling they have realised.

	1D	2D	3D
EURIDICE		X	X
EPFL	X	X	
NRG		X	
ULg	X	X	X
UPC		X	X

Table 10: List of participants and work they have realised within this benchmark

6.1 Results of the 1D model

EPFL and ULg have realised a one-dimensional axisymmetric modelling of the experiment. In order to realise this modelling, EPFL have used ACMEG-T law, implemented in the LAGAMINE code developed at ULg, which is a thermo-plastic model with non-linear elasticity. ULg has used a thermo-elastic model. Principal differences between the two teams come from these different constitutive laws. Only few figures will be given as illustration.

The spatial and temporal evolution of the temperature is the same for both teams. The main differences are in the evolution of the pore water pressure and thus in the evolution of the stress field. These differences are mainly due to the non-linear elasticity and the thermo-plasticity of the ACMEG-T model. The bulk modulus depends on the mean effective stress in this law and, its initial value is equal to 180 MPa. In comparison with ULg who uses a linear thermo-elastic model with K=133.333 MPa, the increase of rigidity with the ACMEG-T is one of the reason for the differences in excess pore water pressure obtained by both teams. Another difference comes from that a progressive plasticity induced by heating is produced with ACMEG-T. This plasticity is mainly contractive and tends to increase the generation of excess pore water pressure.

Figure 69 presents the radial evolution of the pore water pressure at 25 days for ULg and EPFL. Some differences are observed. The evolution of the pore water is more important with the ACMEG-T law than with a thermo-elastic model (ULg). So this difference will have consequences in the evolution of the stress field as exhibit in Figure 70.

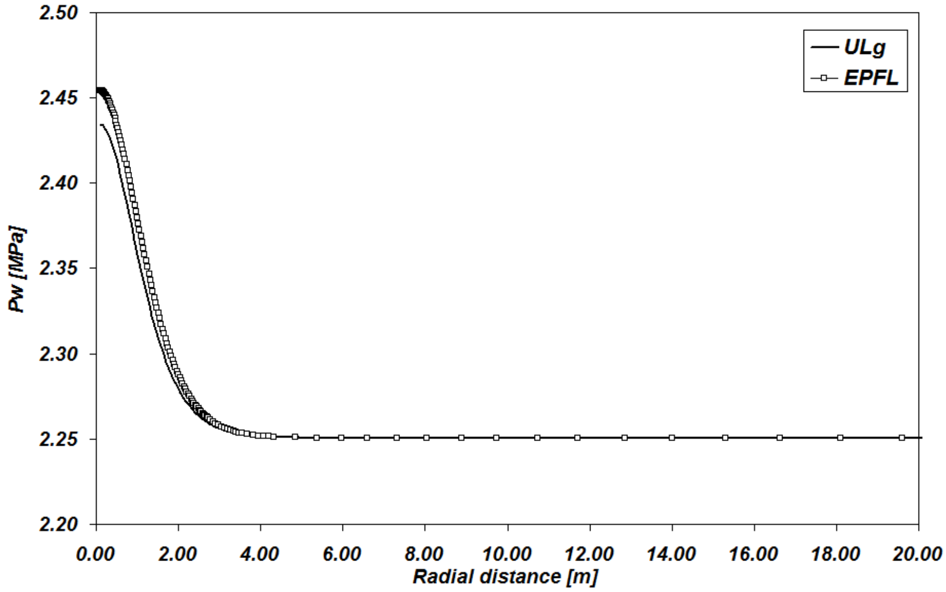

Figure 71: Comparison of the radial profiles of pore water pressure for ULg and EPFL at 25 days

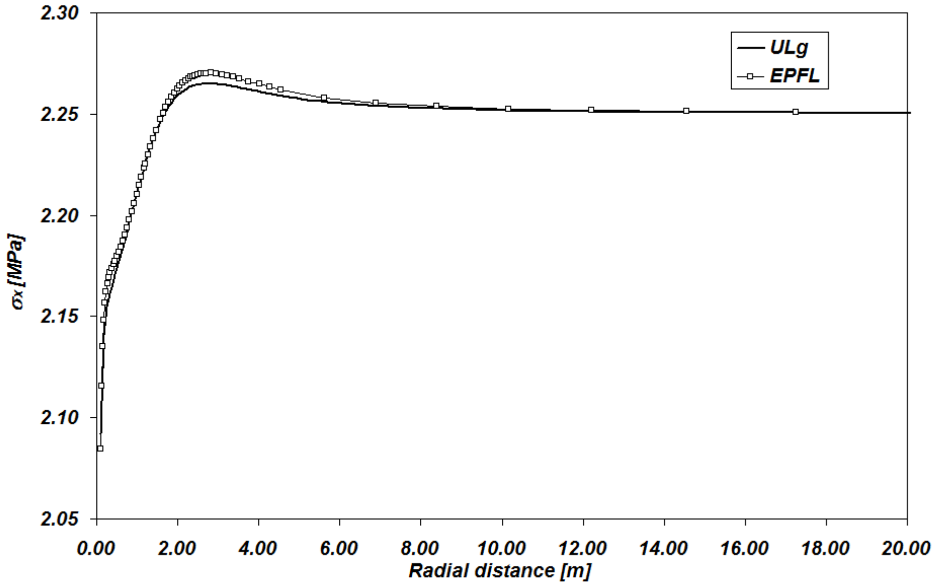

Figure 72: Radial profiles of the radial stress for both teams at 25 days

Concerning the temporal evolution, the same fact is observed that is to say, the evolution of the temperature is same but there is differences between the evolution of the pore water pressure and thus of the evolution of stresses.

Figure 71 shows the evolution of the temperature for a sensor located at 1.5 m from the heater. No difference is observed between the two modellings.

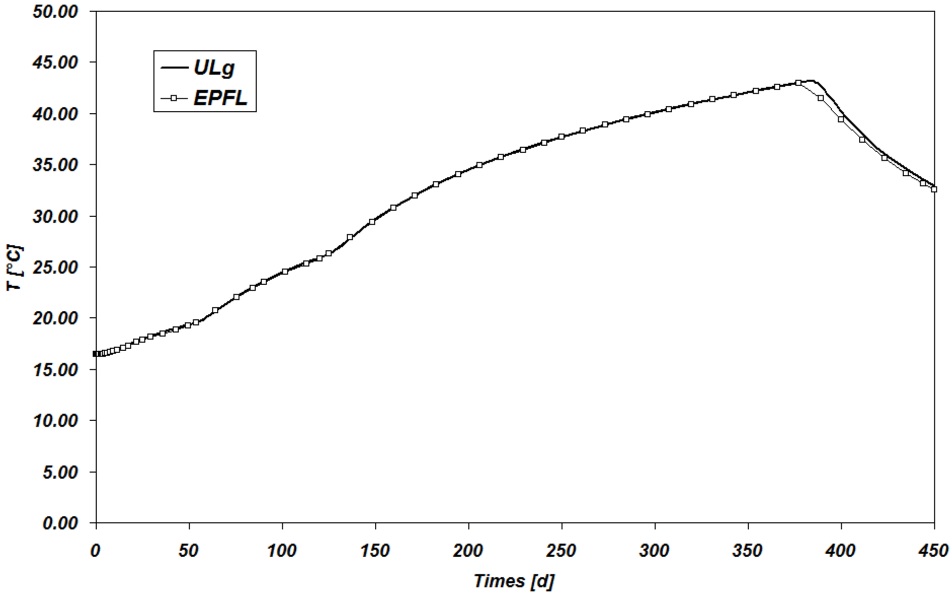

Figure 73: Temporal evolution of the temperature for a sensor

Figure 72 presents the evolution of the pore water pressure for both teams. The evolution is not the same and might be attributed to the different mechanical laws used by the different teams.

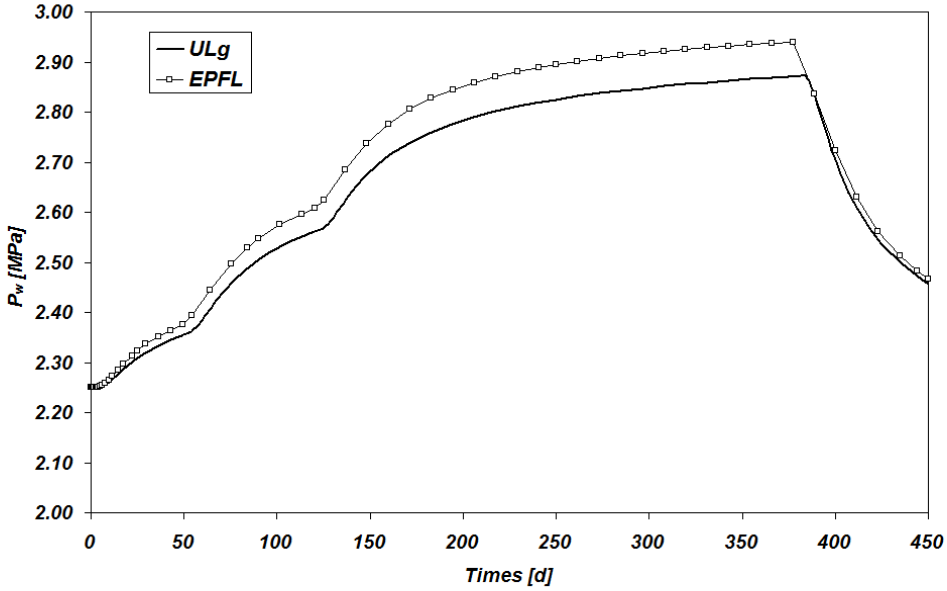

Figure 74: Evolution of the pore water pressure for both teams

6.2 Results of the 2D model

This section will present a comparison between all the partners. As referred to Table 10, all teams have realised this modelling. As the 1D model, ULg and EPFL used the finite element code LAGAMINE. ULg considers a classical thermo-elasticity and EPFL uses ACMEG-T. UPC and EURIDICE use the code CODE-BRIGHT and NRG uses FLAC2D. EURIDICE has considered a Drucker-Prager elasto-plastic model with thermo-elasticity, while NRG and UPC use a thermo-elastic model.

The results show some differences between all the teams and especially with EPFL which uses a thermo-plastic model with a non-linear elasticity. Figure 73 presents an axial profile of the pore water pressure evolution. NRG, ULg and EURIDICE have the same results while EPFL obtained higher pore water pressure due to ACMEG-T model. Finally, UPC obtains a result between EPFL and the other teams.

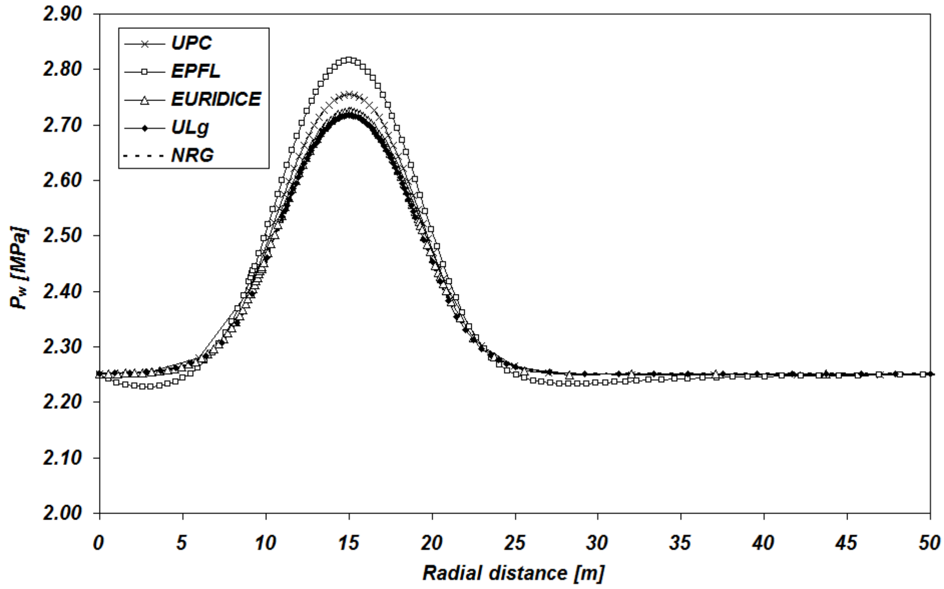

Figure 75: Evolution of the pore water pressure along the axial profile for all teams

Figure 74 represents the temporal evolution of temperature for all teams for the sensor (AT85E). The comparison shows that all the teams are in the same range and the differences are very small.

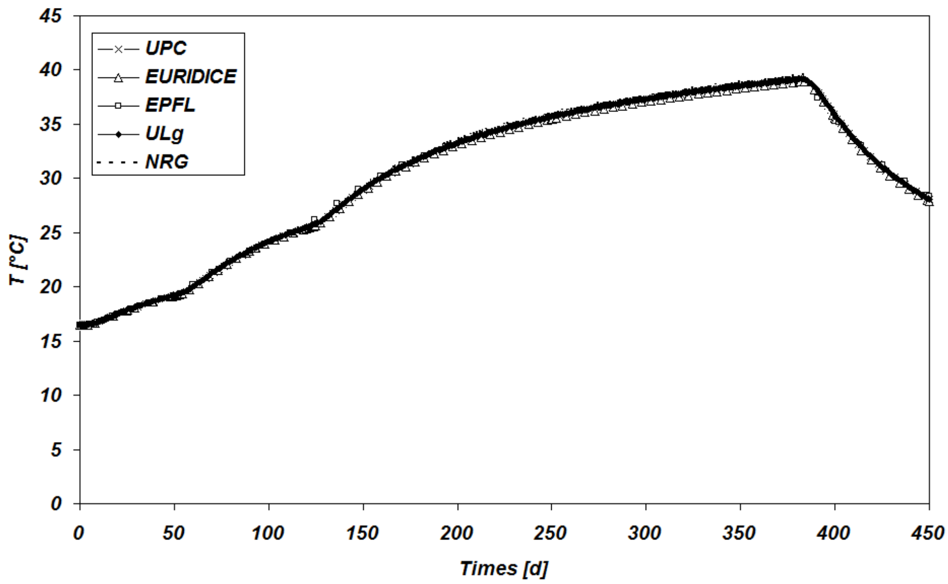

Figure 76: Comparison of temporal evolution of temperature for all the teams

Figure 75 presents the comparison of the evolution of the pore water pressure for all teams at AT85E. The same conclusion as the axial profile might be done. The teams which use thermo-elasticity are in good range while the evolution obtained by EPFL team is different for the reason explained previously.

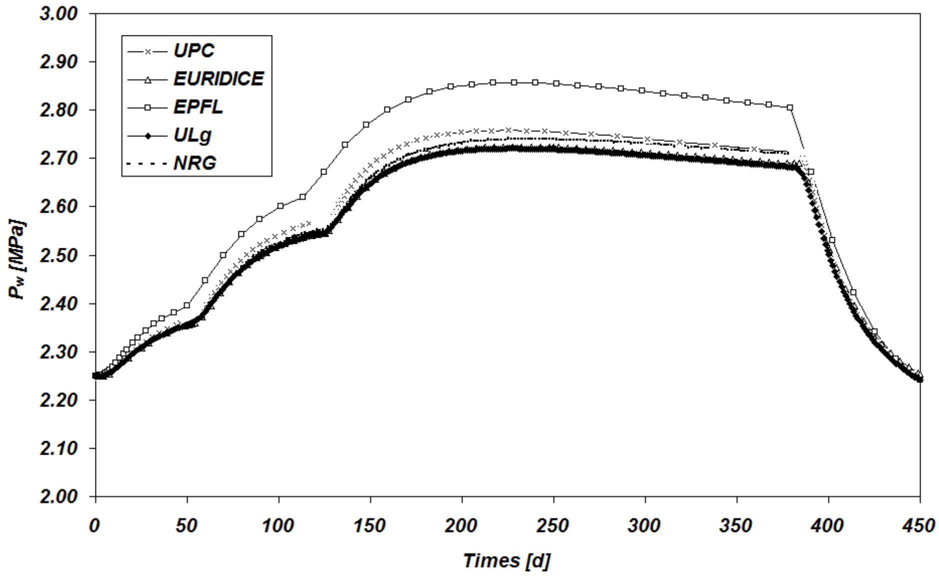

Figure 77: Comparison of temporal evolution of pore water pressure for all the teams

6.3 Results of the 3D model

The comparisons for the 3D concern ULg and EURIDICE. UPC has also realised a 3D modelling but does not used the same boundary conditions. UPC considers the drainage of the main gallery HADES and the drainage of the borehole. As a consequence, the distributions of pore water pressure and stresses are very different from ULg and EURIDICE. Thus, the comparison between UPC and the two others teams will not be presented.

The comparisons between ULg and EURIDICE of the profiles exhibit some differences in term of spatial evolution of stresses. But in term of pore water pressure and temperature the differences are slight. Figure 76 illustrates a comparison between the distributions of the temperature at 250 days according the profile 1. The results are the same and only minor differences exist.

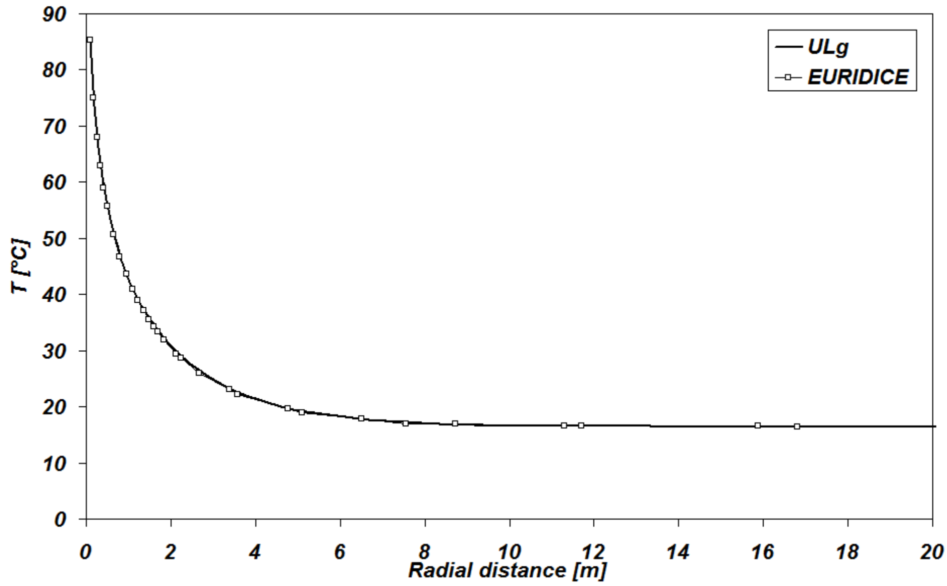

Figure 78: Comparison of the evolution of temperature for profile 1

Figure 77 presents the spatial evolution of the pore water pressure according to the profile 1 at 250 days. There exits some differences between the two teams which are not very important.

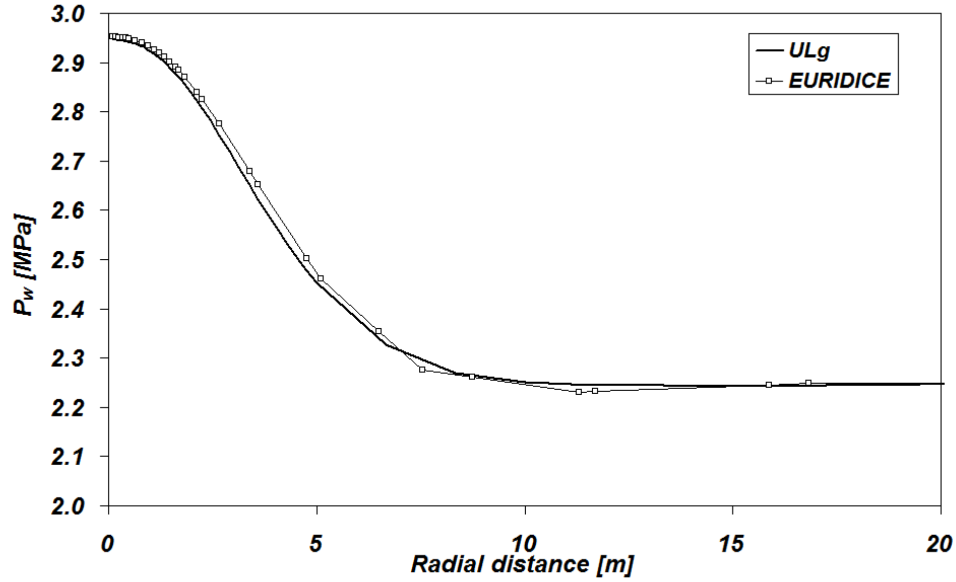

Figure 79: Comparison of the evolution of pore water pressure for profile 1

The evolution of the stress is different for both teams. Indeed, the profiles have the same shape but the influence of the temperature is very important for EURIDICE. The spatial evolution of the stresses is presented in the following figures. Figure 78 presents the stress according the x axis for the two teams. The temperature has an influence over a few meters for ULg while the whole domain seems to be affected by the temperature for EURIDICE.

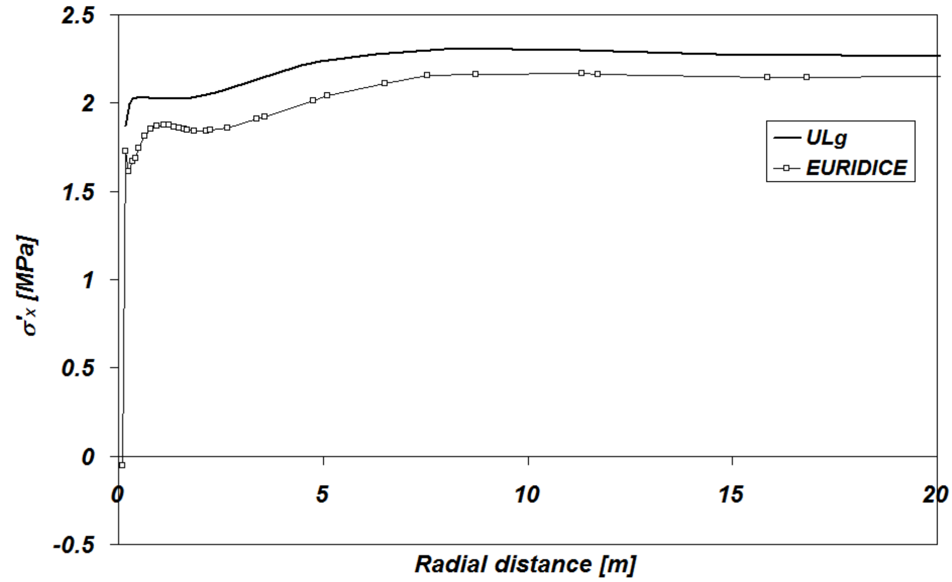

Figure 80: Comparison of the spatial evolution of the x stress according the profile 1 at 250 days

Figure 79 presents the distribution of the y-stress according the profile 1 at 250 days. As seen previously, the whole model is affected by the heating in the case of EURIDICE while only few meters of the clay seems affected by the temperature for ULg.
The difference between ULg and EURIDICE shown in Figure 78 and Figure 79 could be partly due to the difference of some boundary conditions: (1) In modelling by ULg, radial displacement is fixed on the inner surface of the borehole AT89E; while in modelling by EURIDICE, the borehole AT89E is cased with 1.5 cm-thick steel tube, therefore the radial displacement at the interface between Boom clay and steel tube is not fixed, and the thermal expansion of steel tube also contributes to such radial displacement. (2) On surface CDF, fixed normal displacement boundary condition is set by ULg, while fixed normal stress boundary condition is set by EURIDICE.

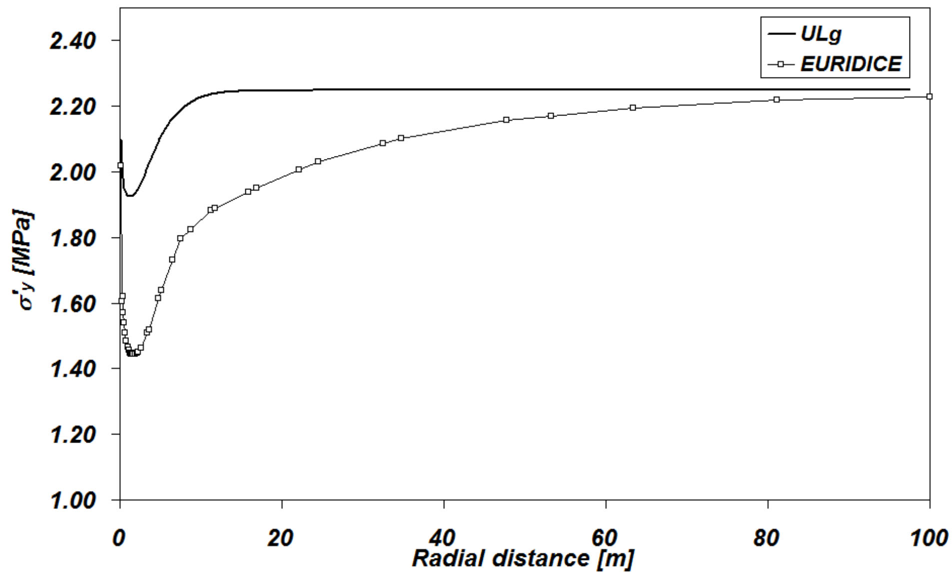

Figure 81: Profile of the y-stress for the two teams according to the profile 1 at 250 days

Figure 80 presents the evolution of the pore water pressure for both teams. This comparison shows that the evolution is quite the same. In general way, the evolution of the pore water pressure is the very similar for both teams.

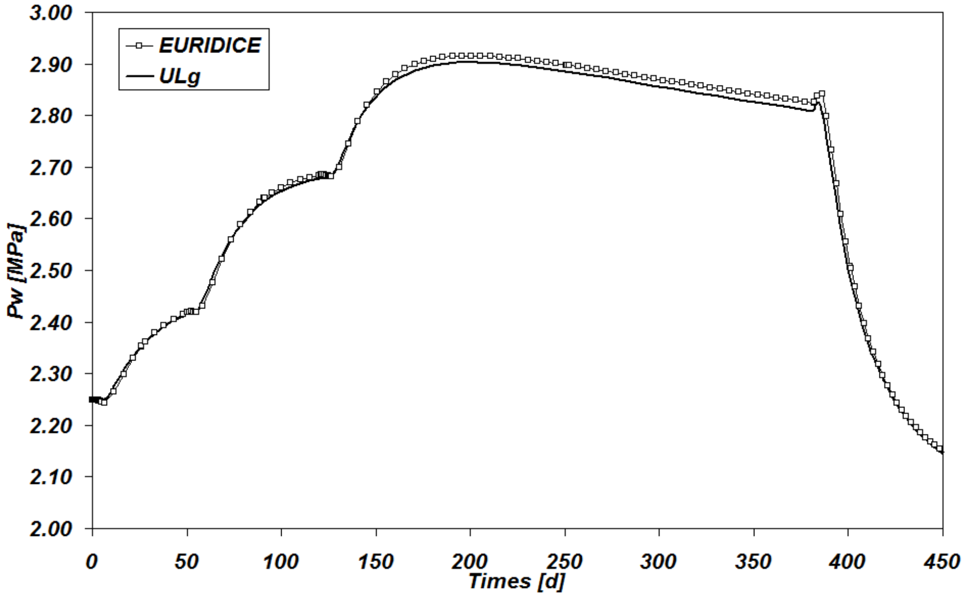

Figure 82: Comparison between the evolutions of the pore water pressure for the two teams

Figure 81 presents the evolution of the temperature for the sensor AT85E. The difference between both teams is slight and is in good agreement.

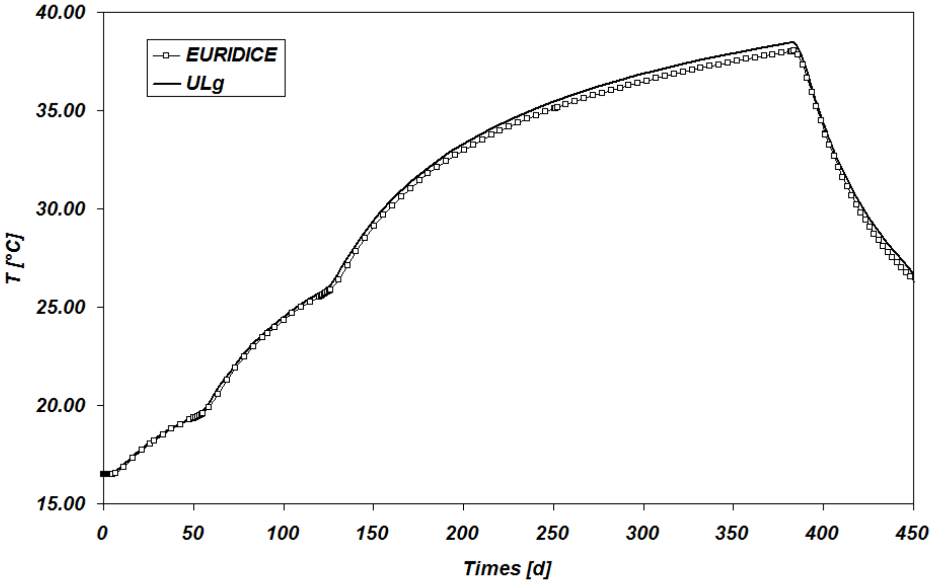

Figure 83: Comparison between the evolutions of the temperature for the two teams for AT85E

7 Additional computations by ULg

During this benchmark exercise, ULg has realised different 3D modellings considering different cases of anisotropy. Indeed, the anisotropy can be considered in the mechanic, the hydraulic or thermal problem. For this exercise, each case of anisotropy is studied separately to better understand their influence on the results and especially on the excess pore water pressure and on the thermal dissipation.

This section presents principal results of these calculations. The results of the calculation where all sources of anisotropy are taken into account have already been presented in section 5.3.

Table 11 below presents the different calculation realised within the 3D model.

CASE	THERMAL ANISOTROPY	HYDRAULIC ANISOTROPY	MECHANICAL ANISOTROPY
ISOTROPIC	NO	NO	NO
ANISO THERM	YES	NO	NO
ANISO HYDRO	NO	YES	NO
ANISO MECA	NO	NO	YES
ANISO THM	YES	YES	YES

Table 11: Different cases of anisotropy considered within the 3D model

7.1 Mechanical anisotropy

From a mechanical point of view, the soft rock is supposed to have a transversely isotropic behaviour due to its mode of deposit. Five independent parameters are needed to describe the mechanical behaviour. In this modelling, the horizontal Young modulus (700 MPa) is greater than the vertical Young modulus (350 MPa). The other parameters are listed in Table 8. Figure 82 shows a comparison between the isotropic case and the anisotropic case along the profile 1 (see Figure 60). These results show that higher pore water pressures are obtained considering the anisotropy of the mechanical parameter. This greater pore pressure is due to the rise of rigidity of the medium. Indeed, the dilation of the pore water pressure generates stresses, and thus strains in the medium. These strains depend on the rigidity of the medium. The induced strain will be more important with a less rigid material. So the volume of the water will take more space and thus, the excess pore water pressure will be less important than for a more rigid material.

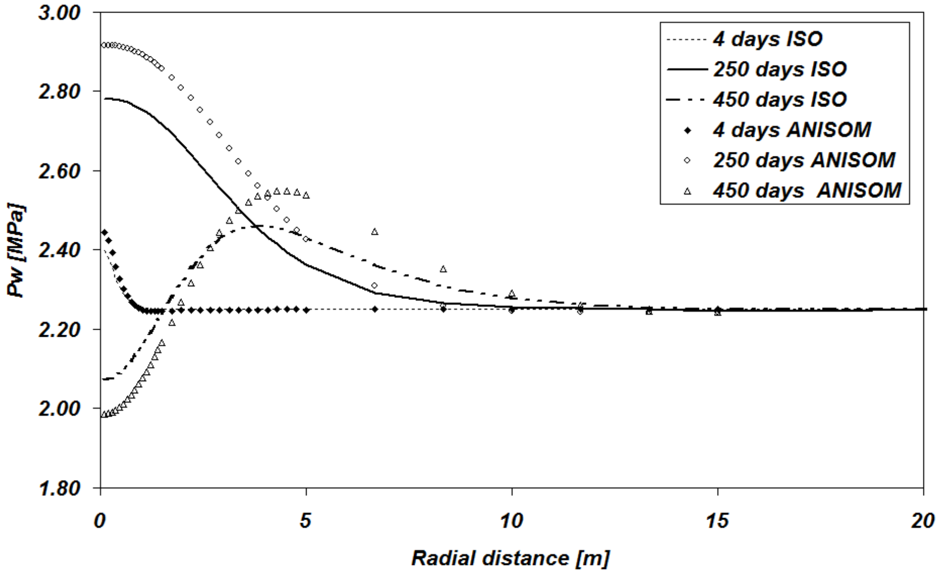

Figure 84: Comparison between the distribution of the pore water pressure for the isotropic case and the mechanical anisotropic case

Figure 83 shows the different evolution of the pore water pressure for the AT85E. The same conclusion as previously might be done. This higher pore water pressure obtained with the anisotropic mechanical law is due to a higher value of the moduli. It is important to note that, only with the anisotropic mechanical model, an increase of pore pressure is observed when decreasing the heat power. The same observation has been made based the in situ measurements. The phenomenon is also observed when increasing the heat power. But the numerical increase is less large than that of the in situ measurements.

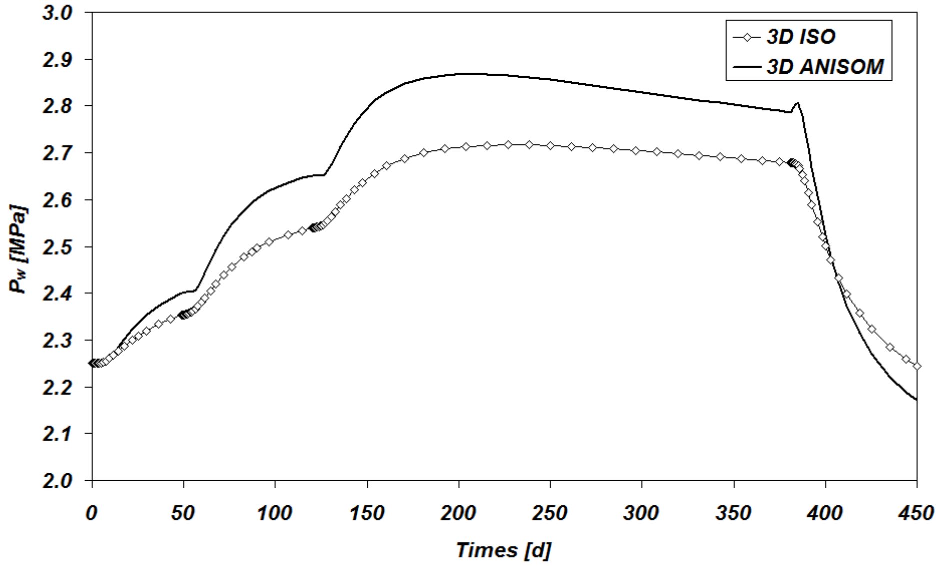

Figure 85: Comparison of the evolution of the pore water pressure for the senor AT85E between the isotropic case and the mechanical anisotropic case

Figure 84 shows a comparison between the distributions of the pore water considering the profile 1 (horizontal plane) and the profile 4 (vertical plane). The evolution of the pore water pressure is the same in the near field but is different in the far field.

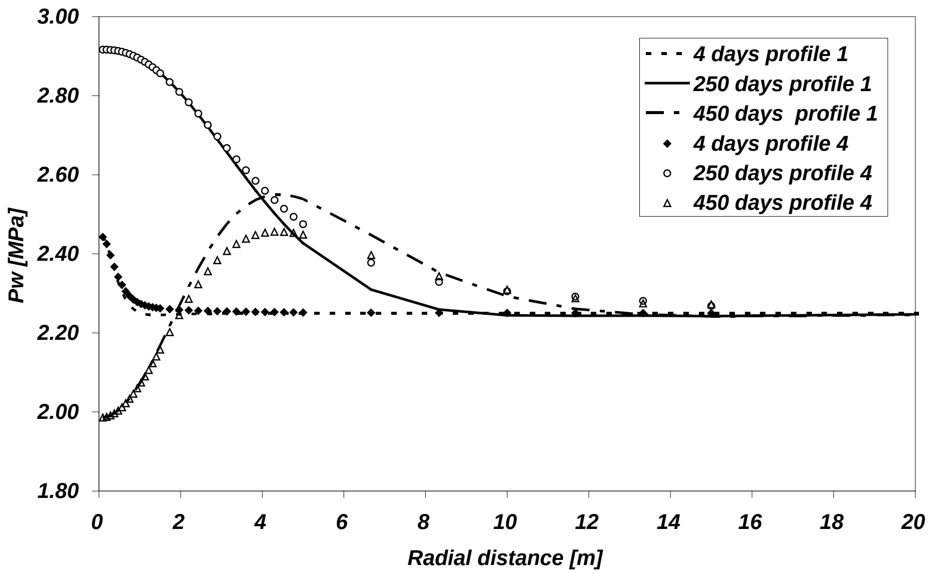

Figure 86: Comparison between the pore water field in according the profile 1 and the profile 4 in the mechanical anisotropic case

7.2 *Hydraulic anisotropy*

For the hydraulic anisotropy, the vertical permeability (4.10^{-19} m²) is lower than the horizontal (2.10^{-19} m²). Figure 85 shows a comparison of the pore water pressure field between the isotropic case and the hydraulic anisotropy case. The effect observed is an increase of the excess pore water pressure when considering the anisotropy of the permeability. This increase might be observed in all profiles and might be explained by a lower dissipation of the excess pore water pressure during heating due to a lower permeability in the horizontal direction as compared with the isotropic case.

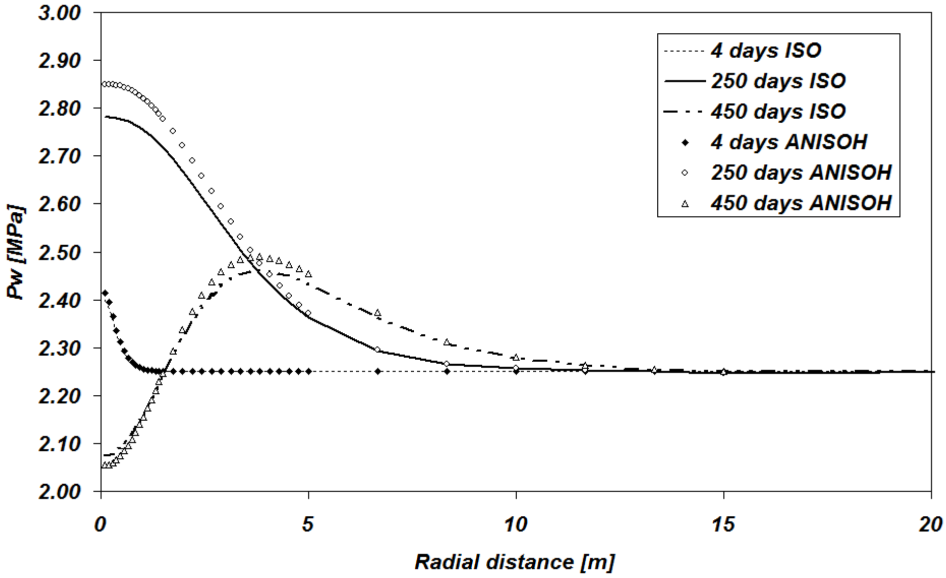

Figure 87: Comparison between the isotropic and the anisotropic hydraulic case concerning the evolution of the pore water pressure along profile 1

Figure 86 shows the temporal evolution of the pore water pressure considering the anisotropic and the isotropic case. The same conclusion as previously might be done. Due the lower permeability in the horizontal direction, the dissipation of the excess pressure is less important than in the isotropic case. As a consequence, higher pore water pressures are generated.

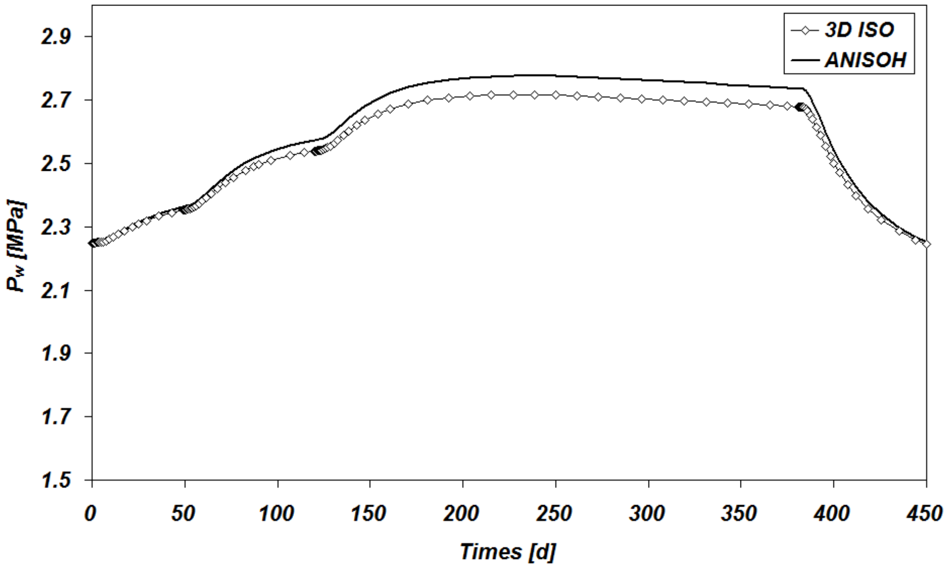

Figure 88: Comparison of the evolution of the pore water pressure for the senor AT85E between the isotropic case and the hydraulic anisotropic case

Figure 87 shows a comparison between the profile 1 and the profile 4 of the distribution of the pore water pressure. This comparison shows that the evolution of the water pressure is quiet the same for the two profiles.

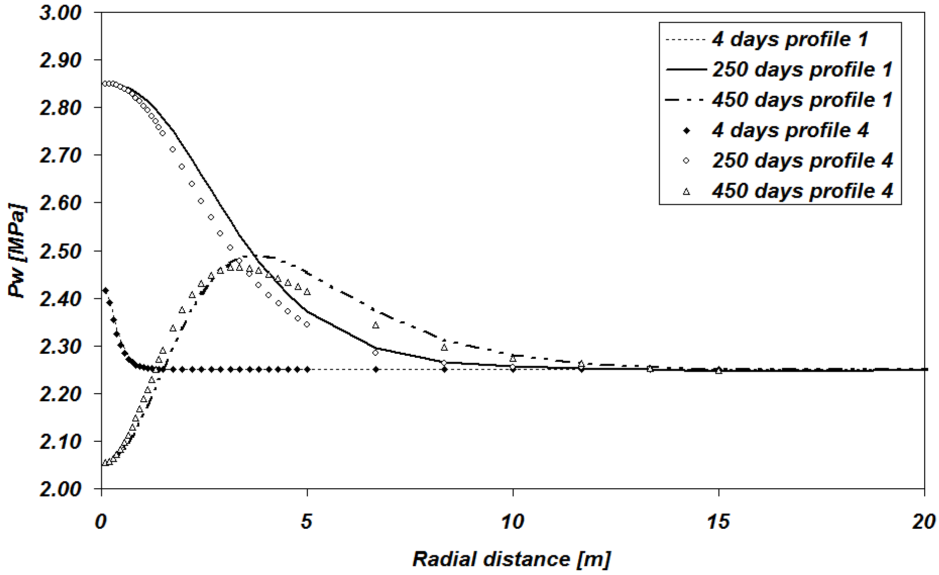

Figure 89: Comparison between the distribution of the pore water pressure according the profile 1 (horizontal plane) and the profile 4 (vertical plane)

7.3 Thermal anisotropy

The thermal anisotropy is characterised by a vertical thermal conductivity (1.25 W/(mK)) which is smaller than the horizontal conductivity (1.7 W/(mK)). As a consequence, the dissipation of the heat in the horizontal direction is more important than in the vertical direction. To highlight this behaviour, Figure 88 illustrates the evolution of the temperature for two points situated at the same distance from the heater (2.75 m) but one in the vertical plane and one in the horizontal plane. The results show that the temperature is higher in the horizontal direction than in the vertical due to this difference of thermal conductivity coefficient.

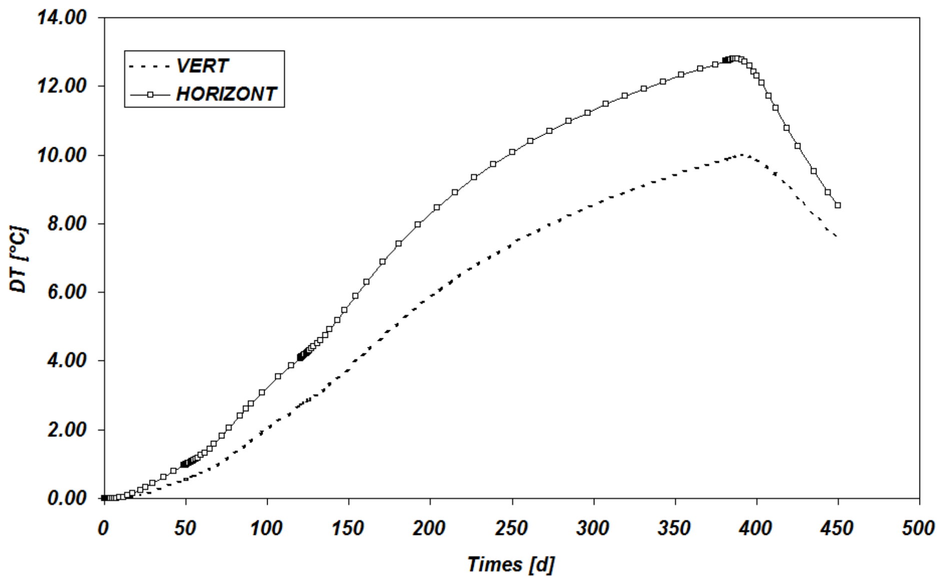

Figure 90: Evolution of the temperature for two points located at a distance of 2.75 m from the heater

The comparison with the isotropic case is realised in Figure 89 which compares the temperature field in the horizontal plane according the profile 1. The result of this comparison seems indicate that the difference is light in the horizontal plane for the two modellings.

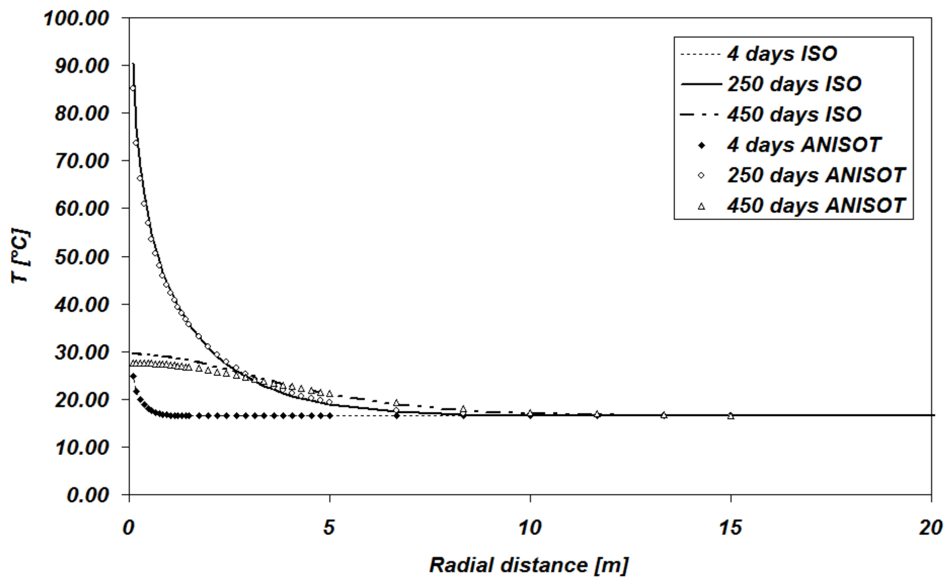

Figure 91: Comparison between the temperature field for the isotropic case and for the anisotropic thermal case

A comparison with the temporal evolution of the temperature at sensor AT85E is given in Figure 90. This comparison shows that in the anisotropic thermal model, lower temperatures are obtained in comparison with the isotropic case.

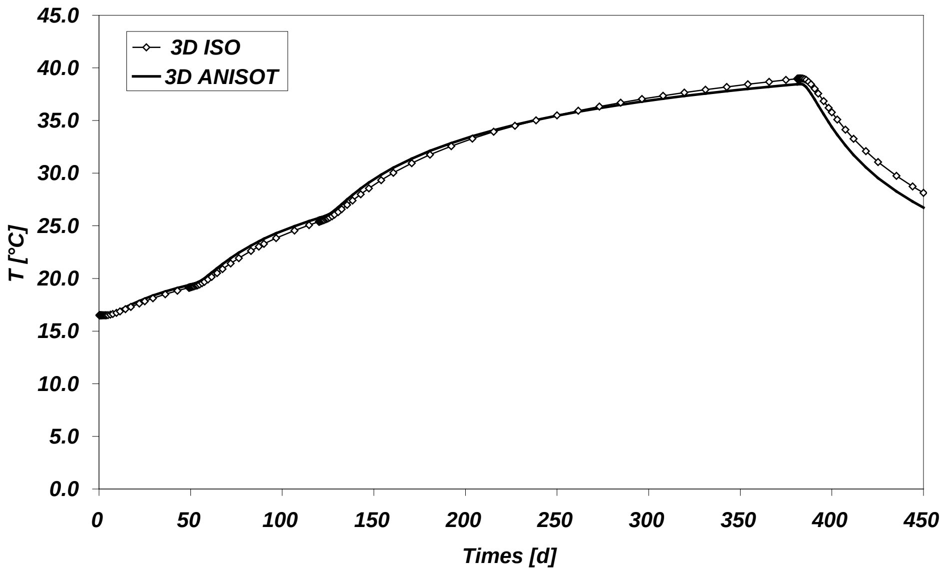

Figure 92: Temporal evolution of the temperature for AT85E for the two cases (isotropic and thermal anisotropic)

A comparison between the profile 1 and the profile 4 of the temperature field is presented in Figure 91. Due to the higher dissipation of heat in the horizontal direction, the temperature in the far field is greater in the horizontal plane than in the vertical plane.

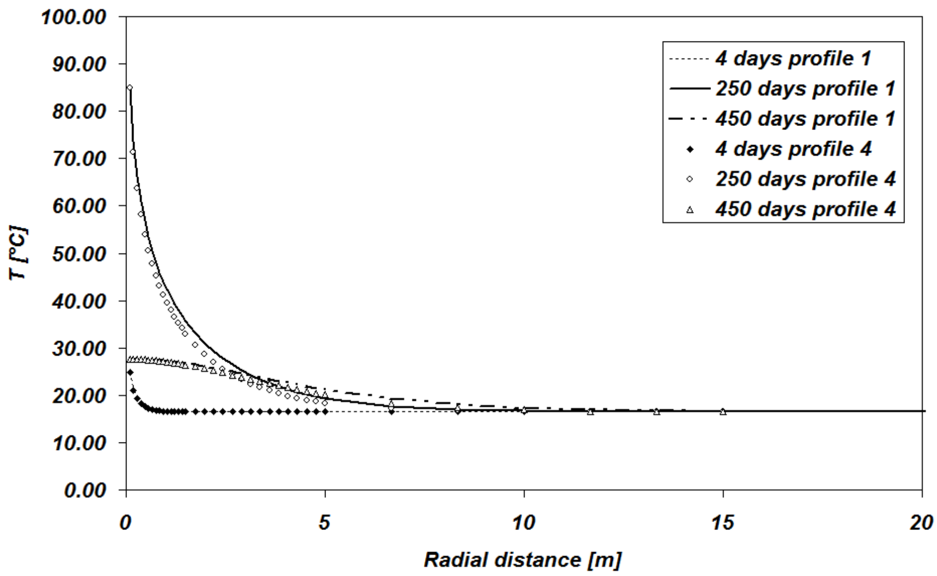

Figure 93: Comparison between the distributions of the temperature along two radial profiles

Figure 92 presents the distribution of the temperature along two axial profiles, one in the horizontal plane and one in the vertical plane. The comparison shows that the temperature evolves more in the horizontal than in the vertical plane as explained previously.

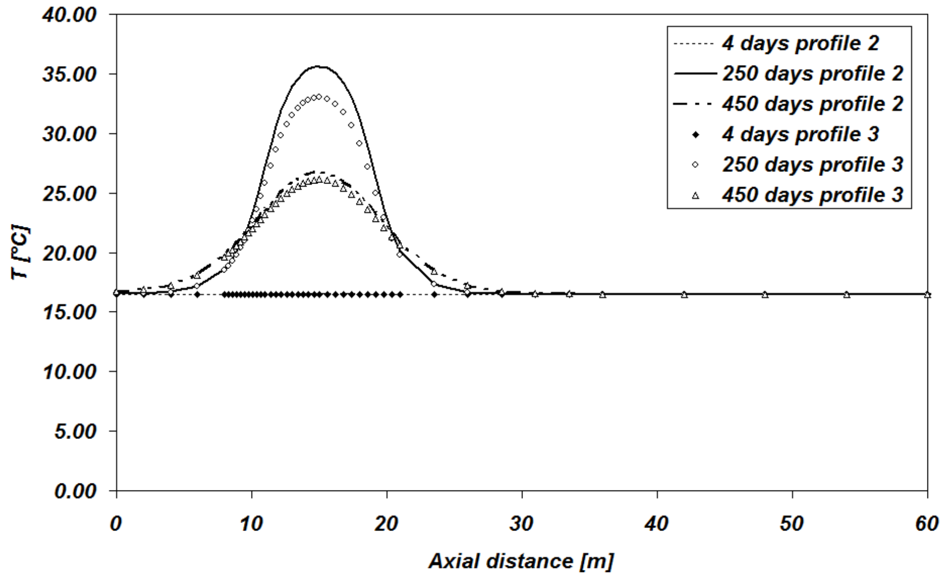

Figure 94: Comparison between the distributions of the temperature along two axial profiles

Figure 93 presents the distribution of the pore water pressure according to the profile 1 and the profile 4. The evolution of the pore water pressure is more important according to the profile 1 due to higher temperature obtained in this direction as seen in Figure 91.

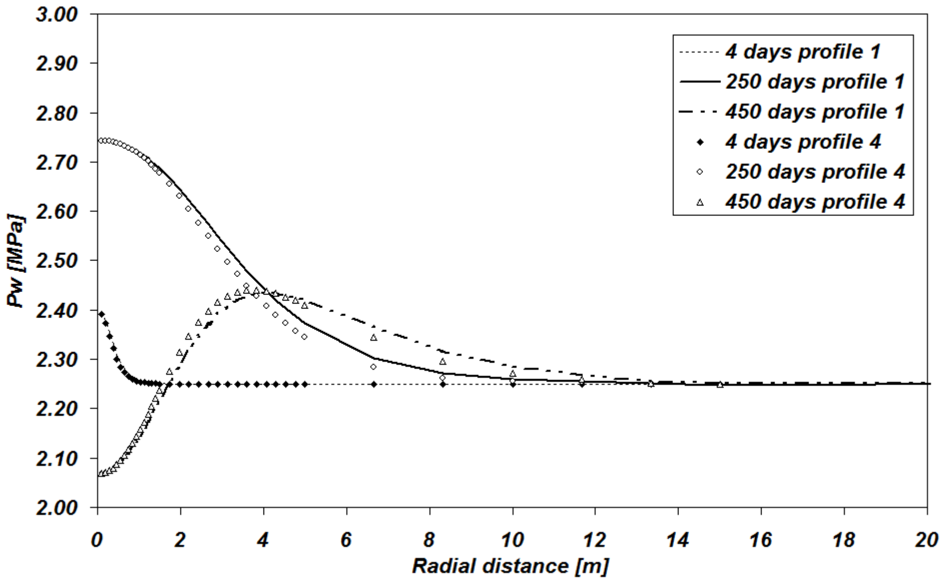

Figure 95: Comparison between the distribution of the pore water pressure according the profile 1 and the profile 4

7.4 Comparisons

Finally, a comparison between all these calculations gives the following evolution of the pore water pressure and the evolution of temperature. Figure 94 represents a comparison of the evolution of the temperature in each case of the 3D modelling. As seen previously the cases where the thermal anisotropy is consider gives lower temperature than the problem where the evolution of temperature is consider isotropic.

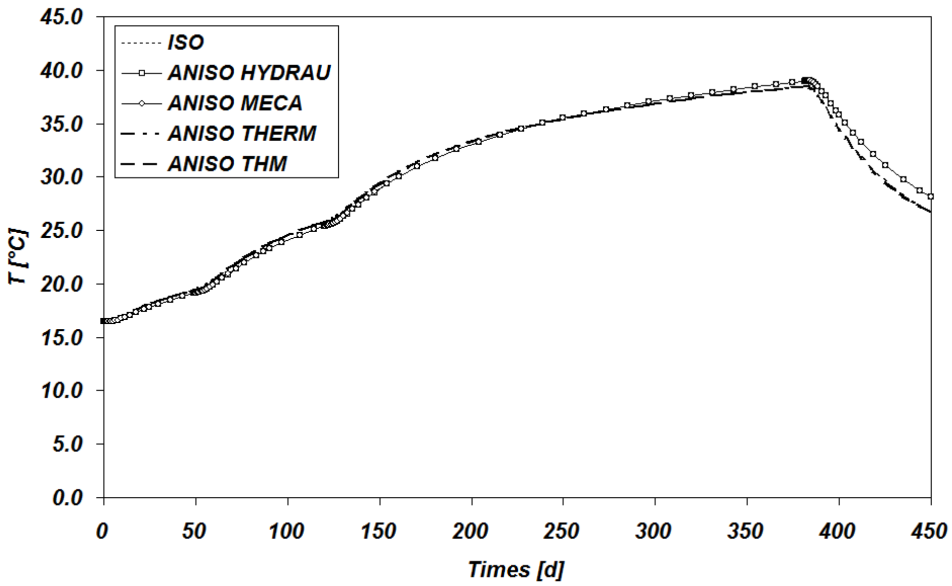

Figure 96: Evolution of the temperature for the sensor (AT85E) for all calculations

Figure 95 exhibit the different evolution of the pore water pressure for the different calculation concerning the 3D model. The mechanical anisotropy seems to play a key role in the evolution of the pore water pressure. The coupling between the different anisotropy gives higher excess pore water pressure than with each kind of anisotropy taken separately. The pore water pressure obtained considering the thermal anisotropy is lower in comparison with the other cases. This is due to the fact that the temperature increases less than in the isotropic case.

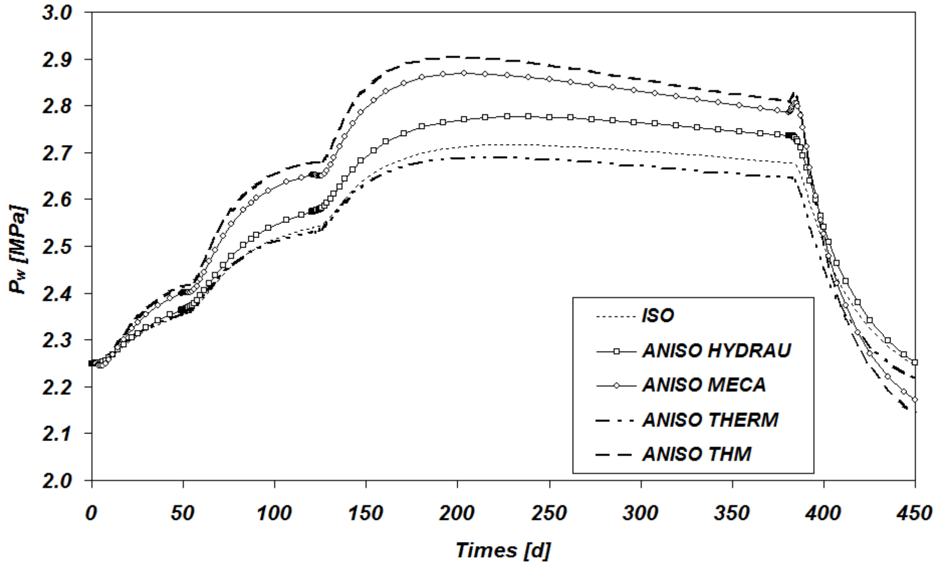

Figure 97: Evolution of the pore water pressure for the first sensor

8 Additional computations by EPFL

The EPFL team carried out the computations with an additional objective in mind; to assess the influence of non-linear thermo-elasticity and thermo-plasticity on the THM response of the repository.

8.1 Mechanical model

The ACMEG-T constitutive model accommodates non-linear thermo-elasticity coupled with a multi-dissipative thermo-plasticity in order to reproduce most thermo-mechanical features. The elastic part of the deformation increment $d\boldsymbol{\varepsilon}^e$ is expressed as following:

$$d\boldsymbol{\varepsilon}^e = \mathbf{D} d\boldsymbol{\sigma}' - \boldsymbol{\beta}'_T \, dT \qquad (8.1)$$

$\mathbf{D}$ is the mechanical elastic tensor defined by the non-linear bulk and shear modulus, K and G, respectively,

$$K = K_{ref}\left(\frac{p'}{p_{ref}}\right)^{n^e} \; ; G = G_{ref}\left(\frac{p'}{p_{ref}}\right)^{n^e} \qquad (8.2)$$

where p' is the mean effective stress, n^e the non-linear elasticity exponent, p'_{ref} the reference pressure, K_{ref} and G_{ref} the bulk and shear modulus at the reference pressure, respectively. $\boldsymbol{\beta}'_T$ is the thermal expansion tensor. Considering an isotropic thermal dilatation, one can express the thermal expansion tensor as $\boldsymbol{\beta}'_T = 1/3\beta'_s \mathbf{I}$ with β'_s being the volumetric thermal expansion coefficient of the solid skeleton.

Using the concept of multi-mechanism plasticity, the total irreversible strain increment $d\boldsymbol{\varepsilon}^{p}$ is induced by two coupled dissipative processes: an isotropic and a deviatoric plastic mechanism. Each of them produces plastic strain increment, $d\boldsymbol{\varepsilon}^{p,iso}$ and $d\boldsymbol{\varepsilon}^{p,dev}$, respectively. The yield limit of each mechanism, restricting the elastic domain in the effective stress space, takes the following expressions:

$$f_{iso} = p' - p'_c r_{iso} = 0;\ f_{dev} = q - Mp'\left(1 - b\ln\frac{p'd}{p'_c}\right) r_{dev} = 0 \tag{8.3}$$

where q is the deviatoric stress. The variables b and d govern the shape of the deviatoric yield limit and M is the slope of critical state line in the $(p'-q)$ plane, which may depend on temperature:

$$M = M_0 - g\left(T - T_0\right);\ M_0 = \frac{6\sin\phi'_0}{3-\sin\phi'_0} \tag{8.4}$$

where ϕ'_0 is the friction angle at critical state at reference temperature T_0 and g defines the linear evolution of M with temperature, M_0 being the value of M at initial temperature.

Each of the yield limits evolves through the generation of plastic strain which is the hardening variable. During loading, the volumetric plastic strain governs the evolution of p'_c and r_{iso}, while deviatoric plastic strains control the evolution of r_{dev}. The preconsolidation pressure, p'_c, depends on the volumetric plastic strain ε_v^p and temperature..

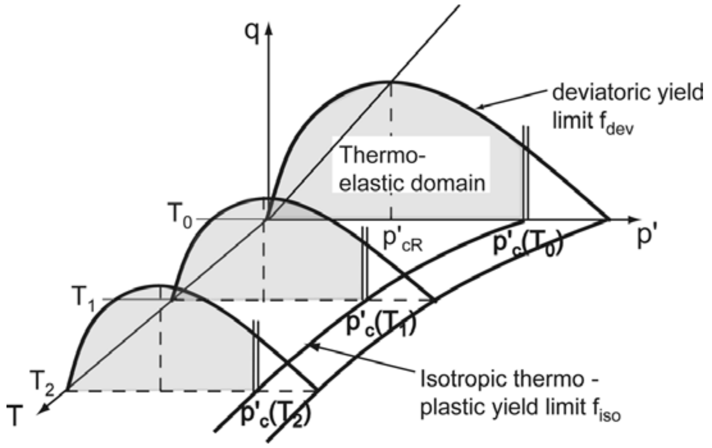

Figure 98: Yield limits for the ACMEG-T thermo-mechanical elasto-plastic framework

$$p'_c = p'_{c0T_0}\exp\left(\beta\varepsilon_v^p\right)\left(1 - \gamma_T\log\frac{T}{T_0}\right) \tag{8.5}$$

where p'_{c0T_0} is the initial value of the preconsolidation pressure at the reference temperature, T_0, while β and γ_T are material parameters.

According to the bounding surface theory, r_{iso} and r_{dev} correspond to the degree of plastification (mobilised hardening) of the isotropic and deviatoric yield limits, respectively. This enables a progressive evolution of the isotropic yield limit during loading and a partial comeback of this limit during unloading. The evolution of r_{iso} during loading is linked to the volumetric plastic strain induced by the isotropic mechanism $\varepsilon_v^{p,iso}$:

$$r_{iso} = r_{iso}^e + \frac{\varepsilon_v^{p,iso}}{c + \varepsilon_v^{p,iso}} \text{ and } dr_{iso} = \frac{(1-r_{iso})^2}{c} d\varepsilon_v^{p,iso} \tag{8.6}$$

where c and r_{iso} are material parameters. In the same way, the evolution of r_{dev} during loading is linked to the deviatoric plastic strain ε_d^p:

$$r_{dev} = r_{dev}^e + \frac{\varepsilon_d^p}{a + \varepsilon_d^p} \text{ and } dr_{dev} = \frac{(1-r_{dev})^2}{a} d\varepsilon_d^p \tag{8.7}$$

where a and r_{dev} are material parameters.

The flow rule of the isotropic mechanism is associated, while the deviatoric one is not and assumes the following forms:

$$d\boldsymbol{\varepsilon}^{p,iso} = \frac{\lambda_{iso}^p}{3}\boldsymbol{I} \tag{8.8}$$

$$d\boldsymbol{\varepsilon}^{p,dev} = \lambda_{dev}^p \frac{1}{Mp'}\left[\frac{\partial q}{\partial \boldsymbol{\sigma}'} + \alpha\left(M - \frac{q}{p'}\right)\frac{1}{3}\boldsymbol{I}\right] \tag{8.9}$$

The plastic multipliers, λ_{iso}^p and λ_{dev}^p, are determined using Prager's consistency equation for multi-dissipative plasticity. α is a material parameter.

8.2 Parameters

Specific thermo-mechanical parameters were determined to accommodate ACMEG-T.

Thermo-mechanical characteristics		Boom Clay
Bulk modulus at the reference pressure [MPa]	K_{ref}	130
Shear modulus at the reference pressure [MPa]	G_{ref}	130
Non-linear elasticity exponent [-]	n_e	0.4
Volumetric thermal expansion coefficient of the solid skeleton [-]	β'_s	1.3.10-5
Material parameter [-]	β	18
Material parameter [-]	γ_T	0.55
Material parameter [-]	c	0.015
Material parameter [-]	r_{iso}	0.001
Material parameter [-]	b	0.8
Material parameter [-]	d	1.3
Friction angle at critical state at reference temperature [°]	ϕ'_0	16
Slope of the linear evolution of M with temperature [°C^{-1}]	g	0.0085
Material parameter [-]	α	0.1
Material parameter [-]	a	0.007
Material parameter [-]	r_{dev}	0.3

Table 12: Thermo-mechanical parameters used for the ACMEG-T model (after François et al., 2009)

8.3 Results

In the following, the 2D results of EPFL will be briefly presented to highlight the influence of non-linear thermo-elasticity and thermo-plasticity on the THM response of the repository.

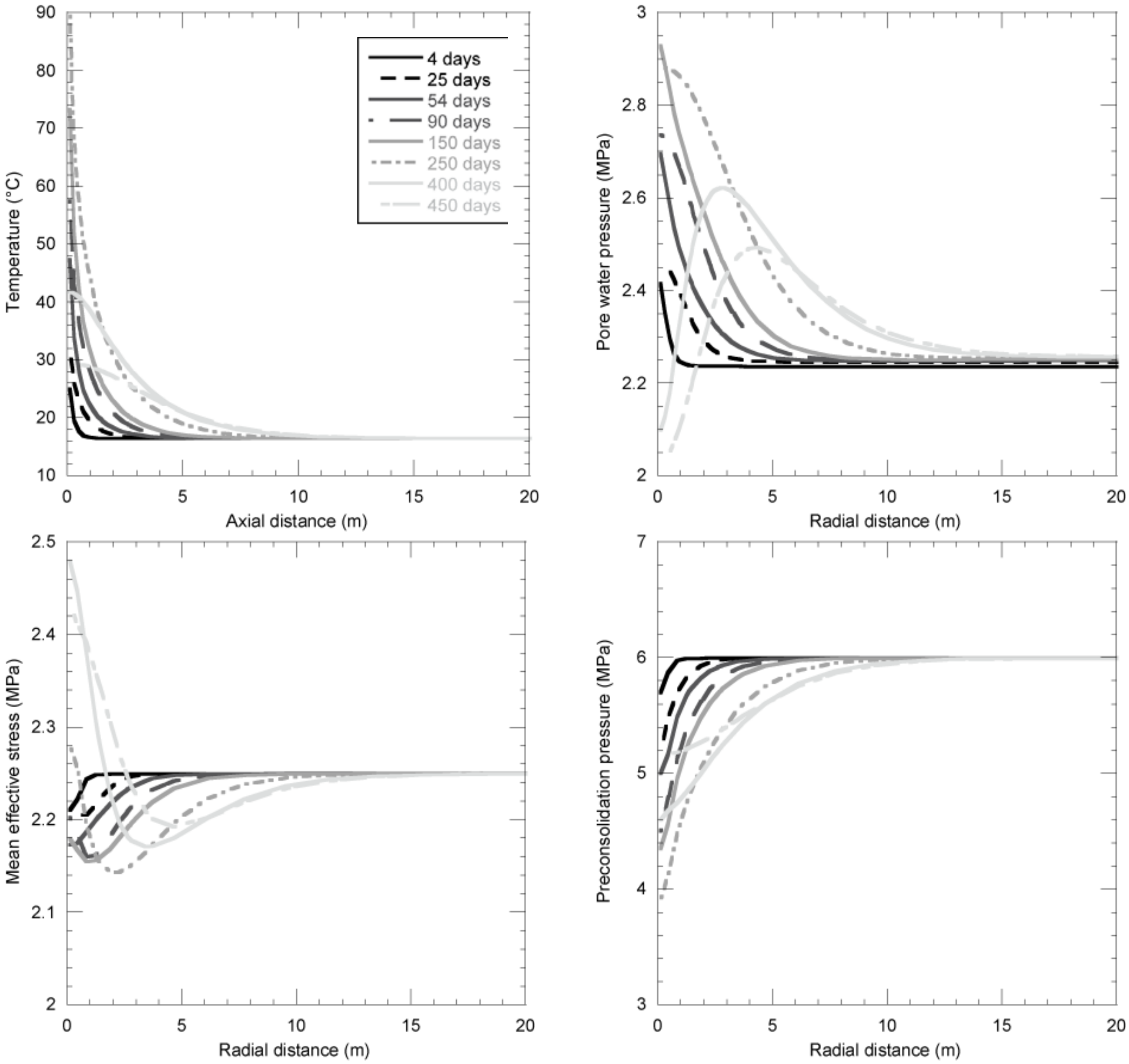

Figure 99: Profile 1 of temperature, pore water pressure, mean effective stresses and preconsolidation pressure in the 2D modelling

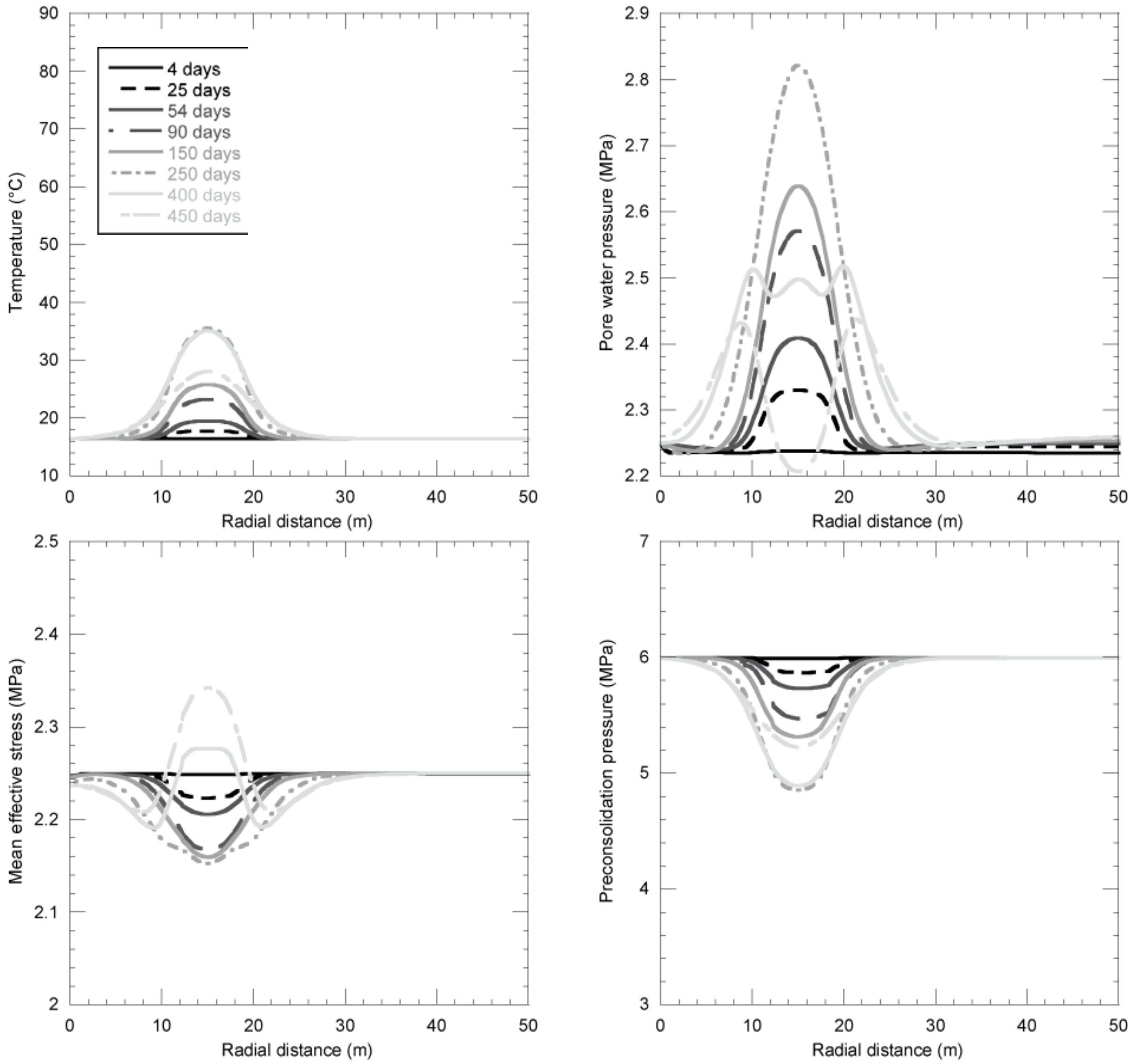

Figure 100: Profile 2 of temperature, pore water pressure, mean effective stresses and preconsolidation pressure in the 2D modelling

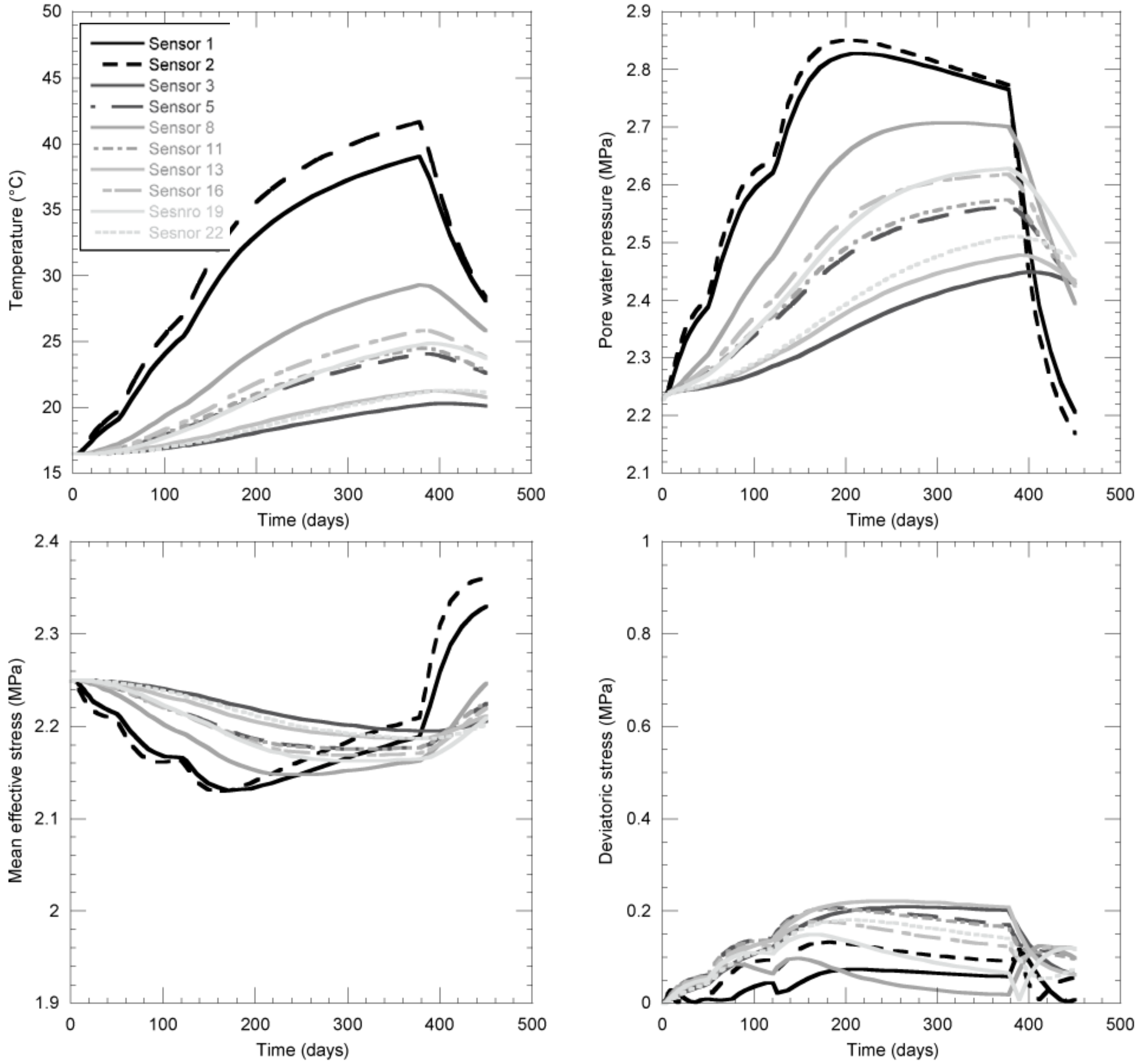

Figure 101: Time evolution of temperature, pore water pressure, mean effective stresses and deviatoric stresses in the 2D modelling

The obtained pore pressures and stress fields differ from those obtained by the other teams. The differences are mainly due to the non-linear elasticity and the thermo-plasticity of the ACMEG-T model. An increase in rigidity as well as progressive plasticity induced by heating, causing an increase of the preconsolidation pressure, is considered in ACMEG-T. This causes an increase in excess pore water pressures, and consequently in effective stresses.

8.4 Conclusion

Modelling of the ATLASIII experiment in 1D and 2D configurations enables visualizing the main characteristics of the soil response under the imposed loading. These results should be analysed in light of results obtained with different constitutive models and in different configurations.

9 Additional computations by EURIDICE

Several additional cases of three dimensional coupled THM modelings were performed for ATLAS III test in order to interpretate the field data of pore water pressure.

9.1 Geometry and mesh

The geometry and mesh of the 3D modeling are illustrated in Figure 100. The computational domain (which could probably be smaller without adverse effect on the numerical accuracy of the computations) covers 100 m in the direction parallel to the axis of main gallery, 119 m along the axis of the central steel tube with heater, and 100m-radius domain rotating along the heater axis is considered. The steel tube with 19 m length, 95 mm external radius and 15 mm thickness is included in the geometry, and the heater is attached to its innermost 8m-long part. The geometry is meshed with 10738 nodes and 9215 hexahedral elements. The Test Drift from which the boreholes were drilled is not included in the geometry.

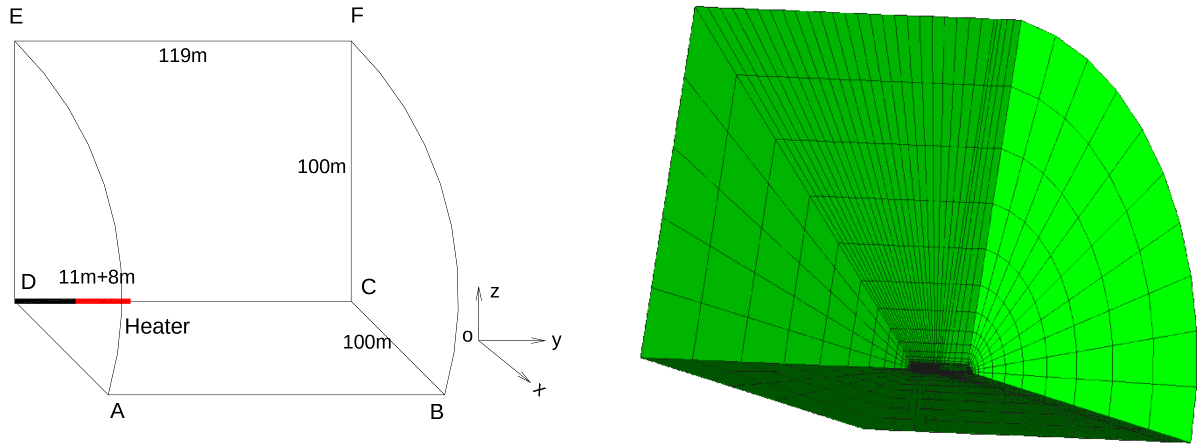

Figure 102: 3D Geometry and mesh

9.2 Initial and boundary conditions

The initial thermo-hydro-mechanical conditions are summarized in Table 13. Anisotropic initial stresses with lateral total stress coefficient $K_0 = 0.85$ are considered in the modeling.

Temperature T_0	Pore water pressure P_{l0}	Porosity n_0	Horizontal stress σ_{h0}	Vertical stress σ_{v0}
$16.5^\circ C$	2.25MPa	0.39	3.825 MPa	4.5MPa

Table 13: Initial thermo-hydro-mechanical conditions

Thermal boundary conditions: All boundaries except the surfaces where heater is located are adiabatic; and the total heat flux along the innermost 8m-long steel tube is presented in Table 3.

Hydraulic boundary conditions: Pore water pressure with value 2.25 MPa is fixed on the boundaries ABFE and BCF; the steel casing and all the other boundary surfaces are impervious (see Figure 100).
Mechanical boundary conditions are defined as follows: Displacement in Z-direction is fixed on the surface ABCD; Displacement in X-direction is fixed on the surface CDEF; Displacements in both X and Z directions are fixed on the surface ABFE; Displacement in Y-direction is fixed on the surface ADE; and on surface BCF normal boundary stress with value 3.825 MPa is applied.
Note that in this modelling, the excavation and drainage-induced perturbations due to the presence of the underground laboratory are not represented. It is believed that these do not affect much the results of simulations focusing on the specific effects of the heater test, as the relevant time scale and spatial scales involved are significantly different. For example, the steel-cased borehole AT89E has been drilled for nearly 20 years when ATLAS III test started, the system was initially at quasi-equilibrium, so it is quite reasonable not to consider the excavation process in the modelling.

9.3 THM parameters

The main THM parameters of the numerical modelling for the Base case are presented in Table 14. Higher thermal conductivity, hydraulic conductivity and Young's modulus in the horizontal plane than those in the vertical plane are employed.

Horizontal Young's Modulus	E_h	MPa	1400
Vertical Young's Modulus	E_v	MPa	700
Shear Modulus	G_v	MPa	280
Poisson's ratio in the horizontal plane	ν_{hh}		0.25
Poisson's ratio for the effect of horizontal strain on vertical strain	ν_{vh}		0.125
Internal cohesion	c	MPa	0.3
Initial friction angle	ϕ_0	°	5
Final friction angle	ϕ_f	°	18
Dilation angle	ψ	°	0
Hardening parameter	β_ϕ		0.01
Thermal expansion coefficient	β_s	$° C^{-1}$	1.0×10^{-5}
Horizontal intrinsic permeability [5]	K_h	m^2	4×10^{-19}
Vertical intrinsic permeability [5]	K_v	m^2	2×10^{-19}
Horizontal thermal conductivity	λ_h	W/(mK)	1.65
Vertical thermal conductivity	λ_v	W/(mK)	1.31
Solid phase specific heat	C_s	J/(kgK)	740

Table 14: Main THM parameters for 3D THM modeling for Base case

9.4 Main results and discussion

Based on the above THM parameters, especially the thermal conductivity, the best comparison of temperature between measurement and modeling we obtained is selected and presented in Figure 101 and Figure 102, and the comparison can be considered excellent.

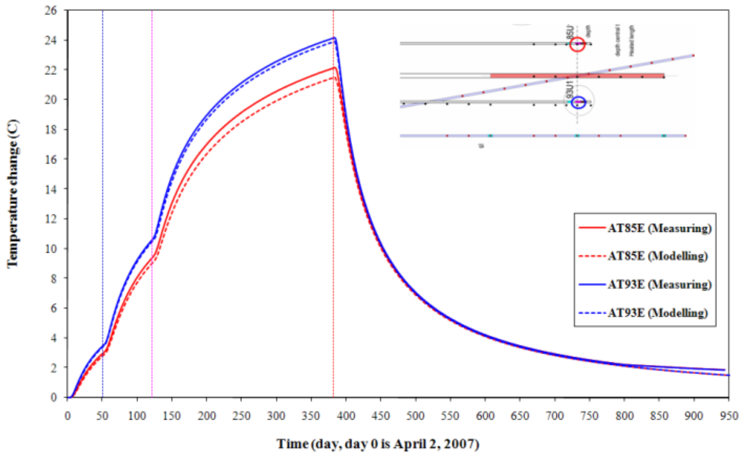

Figure 103: Comparison between modeling and measurement of temperature in sensors AT85E and AT93E

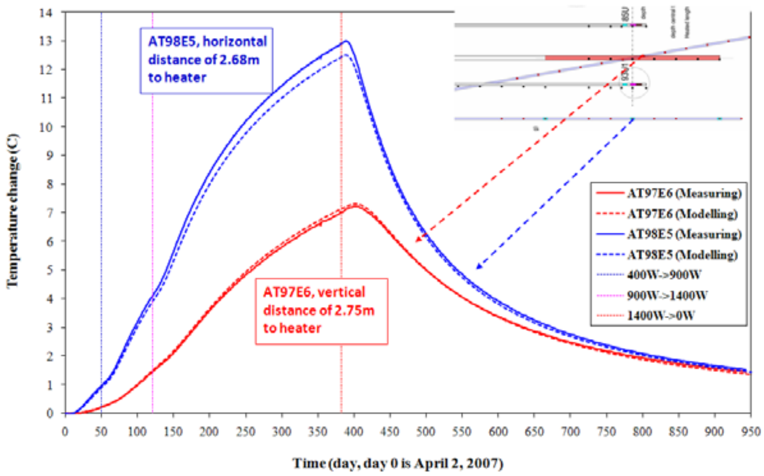

Figure 104: Comparison between modeling and measurement of temperature in sensors TC-AT98E5 and TC-AT97E6

To reproduce the measured pore water pressure by modeling, many cases have been calculated. The thermal conductivity can well model the measured temperature, and the hydraulic conductivity is obtained by two multi point interference tests around the Test Drift, with the values being consistent to the long-term hydromechanical measurement around HADES URF [5]. Therefore it is not necessary to perform parametric study on these parameters. Two cases with different parameters of elasticity are calculated:

For case 1, isotropic elasticity with E=300 MPa, ν=0.125 [6-8] is used, the measured pore pressure increase is nearly 50% underestimated by modeling, and the temporary pore pressure decrease (increase) after increasing (switching off) the power can not be reproduced. For case 2 with anisotropic elastic parameters E_h=700 MPa, E_v=350 MPa, G_v=140 MPa being used, the temporary pore pressure decrease (increase) after increasing (switching off) the power can be reproduced, but the measured pore pressure change is still around 30% underestimated by modeling. Both cases indicate that the plastic zone is very limited to a thin region surrounding steel tube, and elasticity plays major role in the hydromechanical response.

Case 3 employing Cam-clay model [6] is also studied to check if the nonlinear elasticity can improve the modeling of the pore water pressure. The modeling results show that the changes of mean effective stress p' and void ratio e in the main disturbance domain are very limited, so the corresponding change of bulk modulus $K = p'(1+e)/\kappa$ (κ is the elastic stiffness for mean effective stress change) is very small, resulting in very similar behavior to linear elasticity. Therefore modeling employing Cam-clay model can not improve the modeling.

In the previous three cases of modeling, the drainage-induced hydraulic perturbation in the test domain (Figure 24) is not simulated. Case 4 is investigated with the pore water pressures in the positions of the five sensors being dissipated to be as close as possible to the measured values before starting the test. It is found that the consideration of this drainage period has almost no influence on the modeled pore water pressure change.

Besides, parametric study on the influence of Poisson's ratios on the pore water pressure has also been made, and if all the three Poisson's ratio (ν_{hh}, ν_{vh}, ν_{hv}) fall in the range of 0~0.5, the influence is not important.

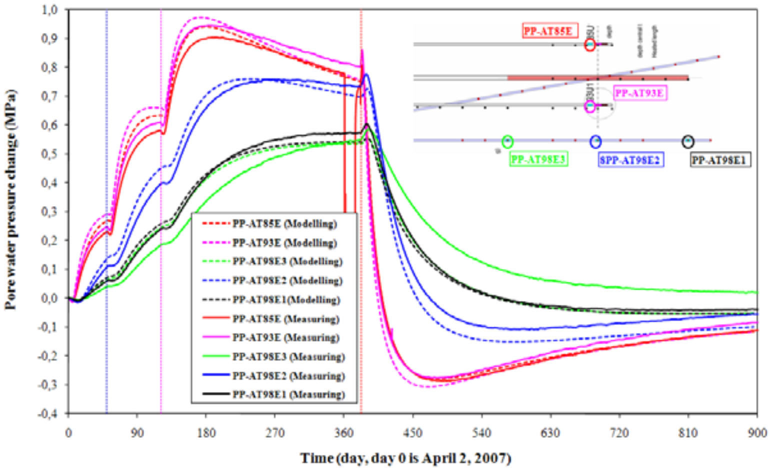

Figure 105: Comparison of pore pressure change between measurement and modeling

The comparison with good match between measured pore water pressure and modeled one displayed in Figure 103 is obtained especially by using the doubled modulii in case 2 (i.e. Base case, see for THM parameters). The modeling can not only well reproduce the temporary pore water pressure decrease after increasing power and temporary pore water pressure increase after cooling in all the five piezometers, but also it gives the close magnitude of the pore water pressure change to the measured one.

Young's modulus was taken as E=300 MPa in previous numerical modeling for interpretation of data around Connecting Gallery [6-7] in HADES. External diameters of both Connecting gallery is around 4.8 m, and excavation disturbance is significant. But the heated borehole AT89E in the ATLAS III test has been drilled for nearly 20 years, the borehole has small diameter of 230 mm, and the deformation of host Boom clay is restricted by the steel tube. Therefore, much less disturbance is induced in ATLAS III test domain, and small elastic strain should be predominant in the test. The above interpretation could justify the use in the simulations of a higher Young's modulus (see Table 14) than that derived from lab tests and back-analysis data collected during excavation works. In fact, the magnitude of the used Young's modulus is close to the one that obtained from the wave velocities of seismic tests on undisturbed Boom clay in HADES [9].

The in-situ measured velocities of P-wave and S-wave are $V_p = 1900\, m/s$, $V_s = 490\, m/s$ respectively. Based on the following analytical relationship between modulus and both wave velocities for saturated and poroelastic medium [9-10]

$$V_p = \sqrt{\frac{E(1-\nu)}{(1+\nu)(1-2\nu)\rho} + \frac{1}{\rho}\left(1-\frac{K_b}{K_s}\right)^2 \frac{K_s^2}{K_s\left[1+n\left(\frac{K_s}{K_f}-1\right)\right]-K_b}} \tag{8.1}$$

$$V_s = \sqrt{\frac{E}{2(1+\nu)\rho}} \tag{8.2}$$

where E is drained Young's Modulus, ν is drained Poisson's ratio, ρ is soil density, K_b, K_s, K_f are bulk moduli of the soil skeleton, soil particle, and pore liquid respectively, we obtain the drained Young's modulus E=1350 MPa, ν=0.39, where the drained Young's modulus is very close to the horizontal Young's modulus shown in Table 14. It should be noted that the above seismic test is also in-situ test reflecting the small strain behaviour of Boom clay, and the eqns (8.1) and (8.2) are derived based on isotropic elasticity.

From the above several cases, it could be found that (1) only when anisotropic mechanical parameters are used, the modelling can reproduce the temporary pore water pressure decrease after increasing power and temporary pore water pressure increase after cooling observed in all the five piezometers, which provides the indirect evidence of the mechanical anisotropic behaviour of Boom clay; (2) Higher Young's moduli could be reasonably employed to obtain better comparison of pore water pressure between modelling and measurement.

10 Additional computations by CIMNE

CIMNE did a number of additional 3D THM computations to analyse the temperature and pore water pressure measurements registered in the third phase of the ATLAS experiment.

10.1 Features

The code used is Code_Bright and a description of the Thermo-Hydro-Mechanical formulation may be found in [11]. The reference parameters in-situ initial conditions for Boom clay are listed in Table 15. They were deduced from the benchmark description and from [12].

			Boom Clay
INITIAL CONDITIONS	Total Stresses [Mpa]	σ_{xx}	4.5
		σ_{yy}	4.5
		σ_{zz}	4.5
		σ_{xy}	0
		σ_{yz}	0
		σ_{zx}	0
	Water Pressure [MPa]	p_w	2.25
	Temperature [ºC]	T	16.5
MAIN PARAMETERS	Young modulus [MPa]	E_h	700
		E_v	350
	Poisson ratio [-]	ν_{hh}	0.25
		ν_{vh}	0.125
	Shear Modulus [MPa]	G_{vh}	140
	Biot's coefficient [-]	b	0.6
	Porosity	φ	0.39
	Equivalent intrinsic permeability [m²]*	k_0	$3.17\ 10^{-19}$
	α is the anis. ratio	α	2
	Thermal conductivity [W/(mK)]	λ_v	1.3
		λ_h	1.7
	Heat capacity of the solid [J $kg^{-1}.K^{-1}$]	C_s	820
	Linear solid thermal expansion coefficient [K^{-1}]	b_s	-1.10^{-5}

* Equivalent: geometric mean in the three directions.

Table 15: Reference parameters used by CIMNE for Boom clay

The mesh used is shown in Figure 104. As Boom clay presents a bedding plane structure due to its sedimentary origin, some anisotropic features had to be considered and a 3D configuration was adopted. Anisotropic thermal conduction law, anisotropic water flow and anisotropic elastic constitutive law were used. The gallery from where the heating borehole was drilled and the heater itself are discretized explicitly. 0 normal displacement and null water and heat flux are prescribed on all external faces. Initial pore water pressure and temperature are prescribed on the bottom face. The excavation of the gallery is reproduced by prescribing atmospheric pressure and ambient temperature on the gallery face from the time of excavation. The heat flux applied in the experiment (Figure 29) was applied on the heater walls. It should be noted that, in contrast with other teams, a draining boundary condition was applied on the heater walls. This choice was shown to influence the determined water permeability [13].

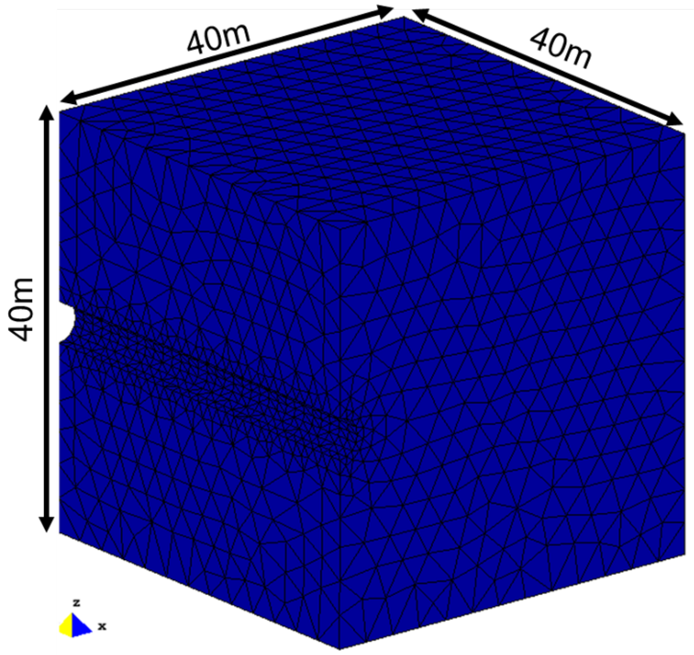

Figure 106: Mesh used to simulate the ATLAS experiment.

10.2 Modelling steps

In general, when one thinks of heat transport in porous media, two modes may appear as candidates: convection and conduction. In fact, in materials as Boom Clay, convection may be neglected because of the low permeability of the medium [14]. Moreover, considering that the soil remains saturated throughout the experiment and that changes in porosity are minor (because of the high rigidity of the medium), couplings from the hydro- and mechanical component to the thermal problem are likely to be very weak. On the basis of these assumptions, the thermal conduction problem can thus be resolved independently.

10.2.1 Thermal problem

The thermal problem was solved for any possible combination of thermal conductivity couple considering values of [0.6, 0.7, … , 2.5] for the perpendicular thermal conductivity and values of [0.6, 0.7, … , 3.5] for the parallel thermal conductivity, using an equivalent medium with a specific heat of 1465 J/kg/K. This amounts to a total number of 600 3D thermal computations. The best fitting thermal conductivity couple was determined for each sensor and each heating stage according to a method developed in [15]. The results are summarized in Figure 105. The average obtained from all the sensors is very close to the reference values. In [15], the authors showed that the observed discrimination in Figure 105 between perpendicular (blue dots) and parallel (orange dots) sensors is typical of an experiment in which the injected heating power is overestimated.

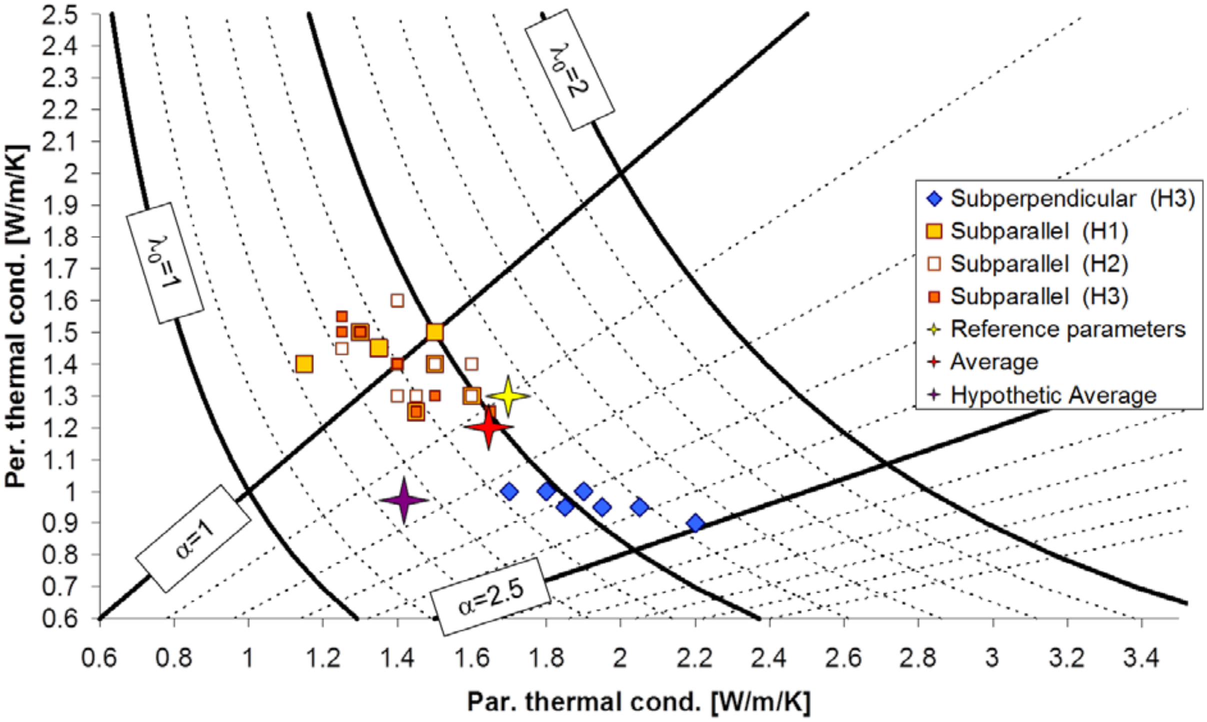

Figure 107: Thermal conductivity values determined for each sensor and each heating period in the ATLAS experiment. The yellow four branches star indicates the reference thermal conductivity values and the red four branches star the average thermal conductivity from this study.

The same exercise was repeated using a power loss coefficient of 95%, 90% and 85% (1800 additional 3D T computations). For a power loss coefficient of 85%, the bestfitting thermal conductivity couple converges 1.4-0.9W/m/K for all sensors as shown in Figure 106.

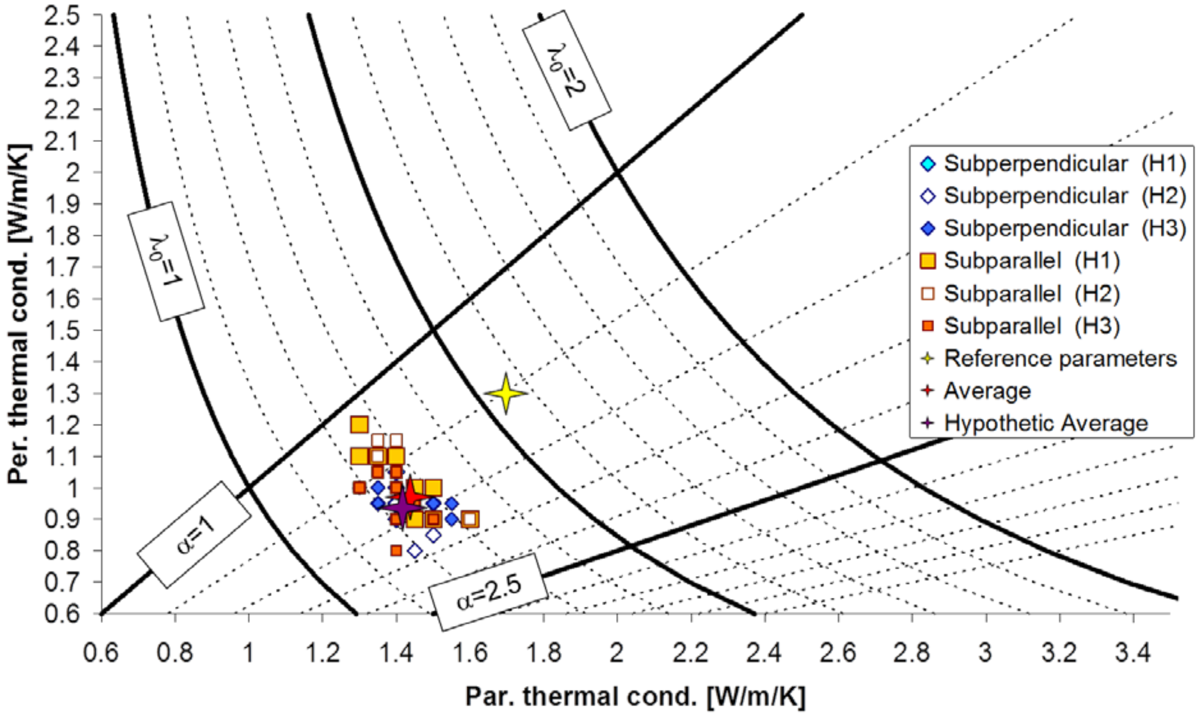

Figure 108: Thermal conductivity values determined for each sensor and each heating period in the ATLAS experiment using a power loss coefficient of 85%. The yellow four branches star indicates the reference thermal conductivity values and the red four branches star the average thermal conductivity from this study.

Using the proposed values, a perfect agreement is reached (Figure 107) for almost all sensors.

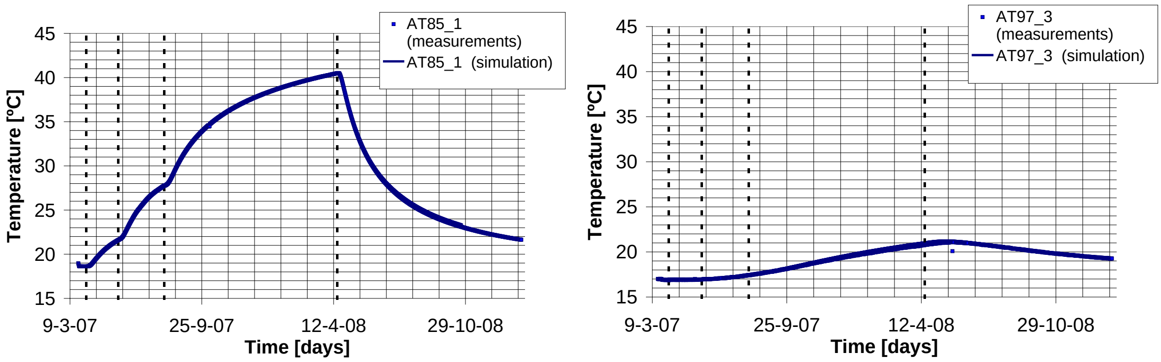

Figure 109: Comparison of measured and simulated temperature in a sensor close to the heater (AT85_1) and a farther one (AT97_3).

Error! Objects cannot be created from editing field codes.	Nr of sensors
0	16
2	1
4	2
6	2
10	2
25	1

Table 16: Distribution of the relative error among the sensors for the bestfitting thermal conductivity using a power loss coefficient of 85% (T* is the measured temperature increment and T the simulated one)

Some conclusions and observations from the thermal problem are drawn:

- Thermal conductivity is thought to be higher in the bedding plane than in the direction perpendicular to it (**1.7-1.2W/m/K** in the case 100% of the thermal power was injected in the experiment or 1.4-0.95W/m/K if a power loss coefficient of 85% is considered).

- After heating power is switched on, a certain time delay is necessary to register the first temperature increase at some distance from the heat source. We have thus a rock volume around the heater with increased temperature and a second constant temperature volume farther from the heater. The limit between both volumes is time dependent (the volume with increased temperature grows in time during heating). The delay was found to be inversely proportional to the thermal conductivity of the medium and proportional to the square of the distance between the heat source and the point.
- As a consequence, at equal distance from the heater, points in the same bedding plane as the heater will experience a shorter delay before the first temperature increase than points perpendicular to the bedding plane.
- Once temperature increases, it occurs faster and reaches a higher value in the bedding plane than in the perpendicular direction (for equidistant points from the heater).

10.2.2 Thermo-Hydro-Mechanical problem

The applied thermal load triggers a Hydro-Mechanical response of the rock as both, the rock skeleton and the water in the rock pores expand when heated. The hydro- and the mechanical response are tightly coupled. The mechanical response is discussed first.

The heated volume around the heater undergoes an expansion as a consequence of the temperature increase. The constant temperature rock volume reacts mechanically to the expansion of the heated volume: the non-heated volume has a tendency to radial compression and circumferential expansion (relative to the heater). We prefer to speak about tendency to compress/expand, because the response of this low permeability material is nearly undrained for the time scale in consideration.

The hydraulic response of the rock depends also whether the considered point is located in the heated or in the constant temperature volume. In the zone with constant temperature, the tendency of the material to expand/compress generates excess pore water pressure. In points located in the same bedding plane as the heater, radial compression is smaller than the circumferential expansion because of the mechanical cross-anisotropic behaviour of the material (sedimentary rocks are believed to have a larger stiffness in the bedding plane than in the perpendicular direction) and in such a point, the material has a tendency to undergo a volumetric expansion. This tendency results in a pore water pressure decrease. In points in the direction perpendicular to the bedding, we have positive excess pore water pressure during the constant temperature phase.

As soon as the temperature starts to increase, two processes are in competition: compression of the water because thermal expansion of the water is larger than that of the rock skeleton and dissipation of the generated excess pore pressure. In a first stage, pore water pressure will increase: compression of the water is stronger than the dissipation. It should be noted that the pore water pressure increase rate depends on 1) the temperature increase rate and 2) the permeability of the medium. After some time, temperature increase rate decreases and excess pore water pressure starts to dissipate faster than they are generated by the temperature increase. Note that the dissipation of high pore pressures in the near field may also trigger an increase of pore water pressure in the far field.

Pore water pressure changes generated by temperature changes also contribute to the deformation of the medium through the effective stress concept.

The previous observations are illustrated in the next figures in which we compare the measured and simulated pore water pressure evolution.

Excess pore water pressure measured in the five sensors of the ATLAS experiment is plot against simulation results in Figure 108. The good agreement between measurements and simulation was achieved by introducing one change in the Boom clay reference parameter set: the equivalent water permeability was decreased from 3.2 $10^{-19} m^2$ to 1.1 $10^{-19} m^2$ (anisotropy ratio was kept constant). A similar agreement may have been reached by an increase of the stiffness.

When temperature starts to increase at the location of the sensor, a pore water pressure rise is generated. This pore water pressure response may be understood as follows. The temperature increase causes a thermal expansion of the water and the solid grains and a thermal expansion of the solid skeleton. Albeit the thermal expansion coefficient of the grain and of the skeleton is equal, the balance of all the terms is negative because the thermal expansion coefficient of water is larger than that of the solid. Moreover, the pore volume changes are also affected by the material stiffness that have to be taken into account because of the effective stress changes. The combination of all these effects is known as the differential thermal expansion of solid and water [14]. The differential thermal expansion is first balanced by water and solid compression, resulting in a compression of the water and thus a rise of the pore water pressure. The different temperature evolution at different distances from the heater establishes a water pressure gradient, generating water flux. According to the local gradient, this water flux may cause pore water pressure to increase or decrease. In the long term the excess pore water pressure dissipation will overrule the pore water pressure rise generated by compression of water (when temperature increase rate is small in comparison to the drainage velocity). This competition is reflected by a peak in the pore water pressure evolution curves.

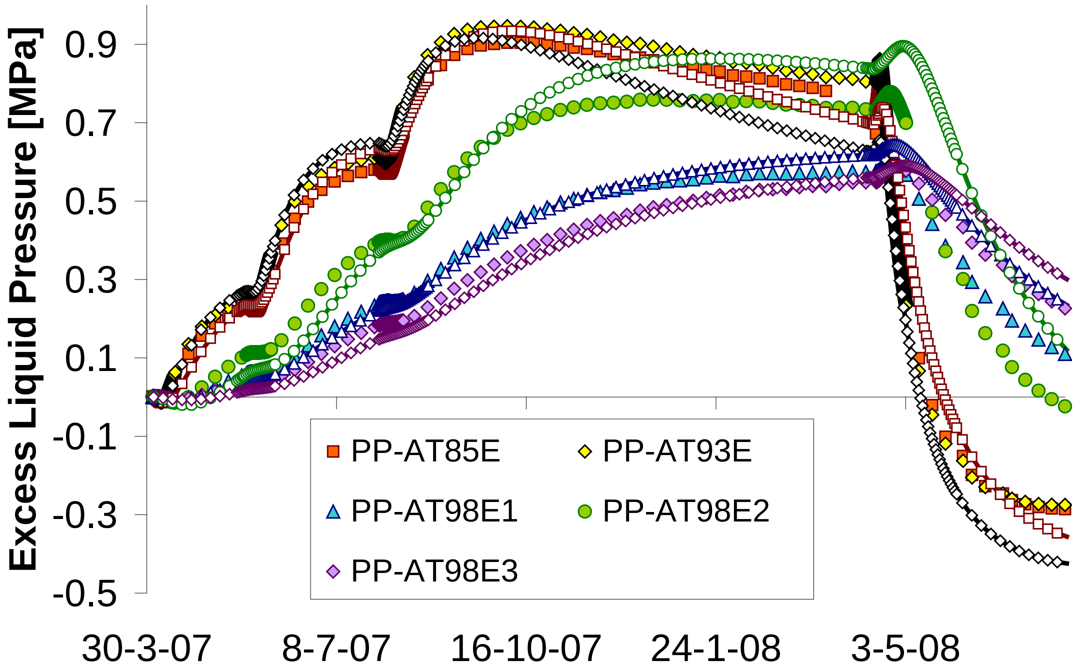

Figure 110: Measured (filled symbols) and simulated (white symbols) excess pore water pressure generated by heating in the ATLAS experiment from 30/03/07 to 26/07/08.

Figure 109 is a zoom on the first days of heating when (almost) no temperature changes are registered at the sensors locations. Temperature evolution of sensor AT93 was added on a small range secondary axis. When heating starts, temperature is increased in the zone near the heater. This temperature increase reaches the position of the two nearest sensors (AT93 and AT85) about 3 days after the start of heating and somewhat later in the three farther sensors. During those 3 days, pore water pressure decrease is registered and reproduced quite well by the simulation. The pore water pressure decrease may be explained as follows. Temperature increase in the zone between the sensor and the heater generates an expansion of the heated zone. In reaction to this expansion, points located in the non heated zone undergo a radial compression and a circumferential expansion. According to the stiffness anisotropy of the medium, in the horizontal direction the radial compression will be less than the circumferential expansion, resulting in a net volumetric expansion compensated by a decrease of the pore water pressure.

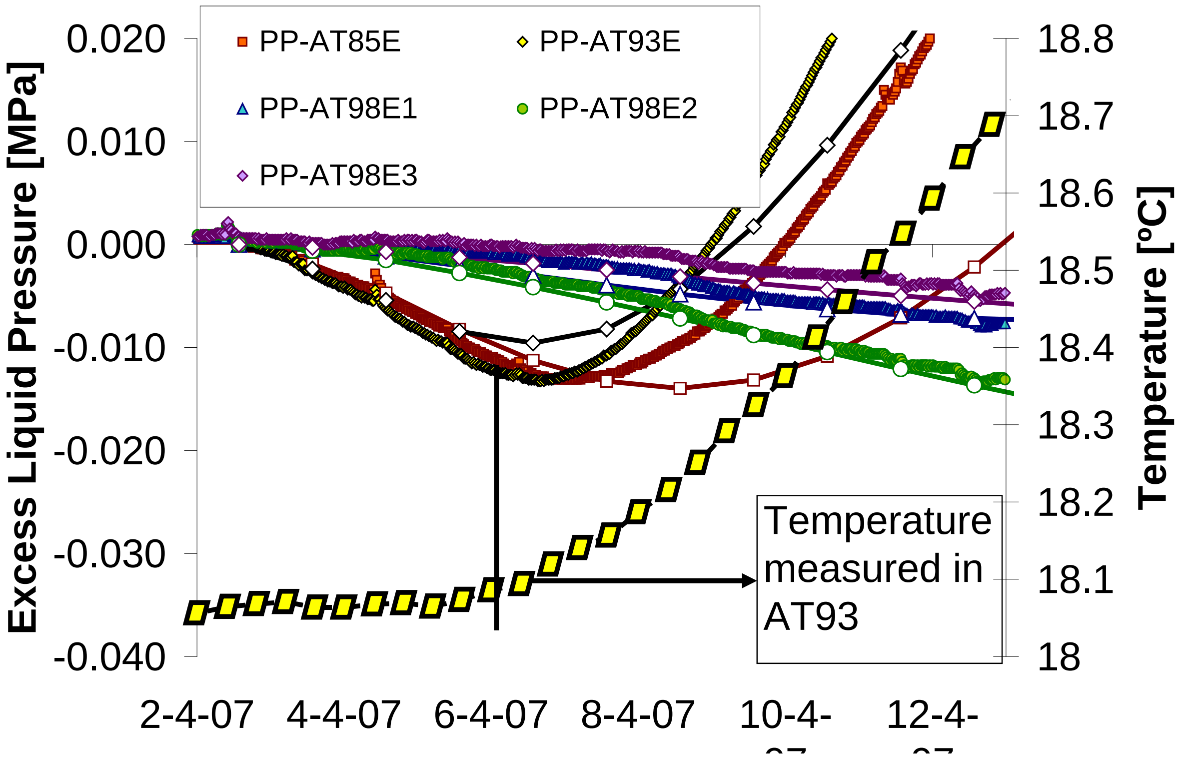

Figure 111: Measured (filled symbols) and simulated (white symbols) excess pore water pressure generated by heating in the ATLAS experiment from 2/04/07 to 13/04/07.

The results of a sensibility analysis of the water permeability are illustrated in Figure 110 and Figure 111 in which we compare measurements and simulation results in a sensor near the heater (AT85) and a farther sensor (AT98-3). Three permeability values are analysed: a large one, corresponding to the reference value for Boom Clay, an intermediary value, corresponding with our best estimate for the rock permeability, and a low value, equal to the reference value divided by nine. In a medium with a larger permeability the pore water pressure increase is initially faster than in a low permeability medium and the pressure rise may even occur before the temperature increase because the generated excess pore pressure between the heater and the sensor is drained faster toward the non-(or less-)heated zone.

The sensitivity analysis of the permeability allows also for estimating the importance of this parameter. A difference of one order of magnitude between the two extreme cases indicates a non-negligible difference of 0.5MPa and 1.5MPa excess pore pressure. Obviously, the maximum excess pore pressure is reached in the less permeable medium. This high sensitivity brings heating tests forward as possible candidates for the determination of permeability. Finally we would like to highlight the very similar pore water pressure evolution simulated in the farther sensor for the two lower permeability values. This similarity is due the fact that at this distance from the heater and for these low permeability values, the drainage term is negligible throughout the experiment duration.

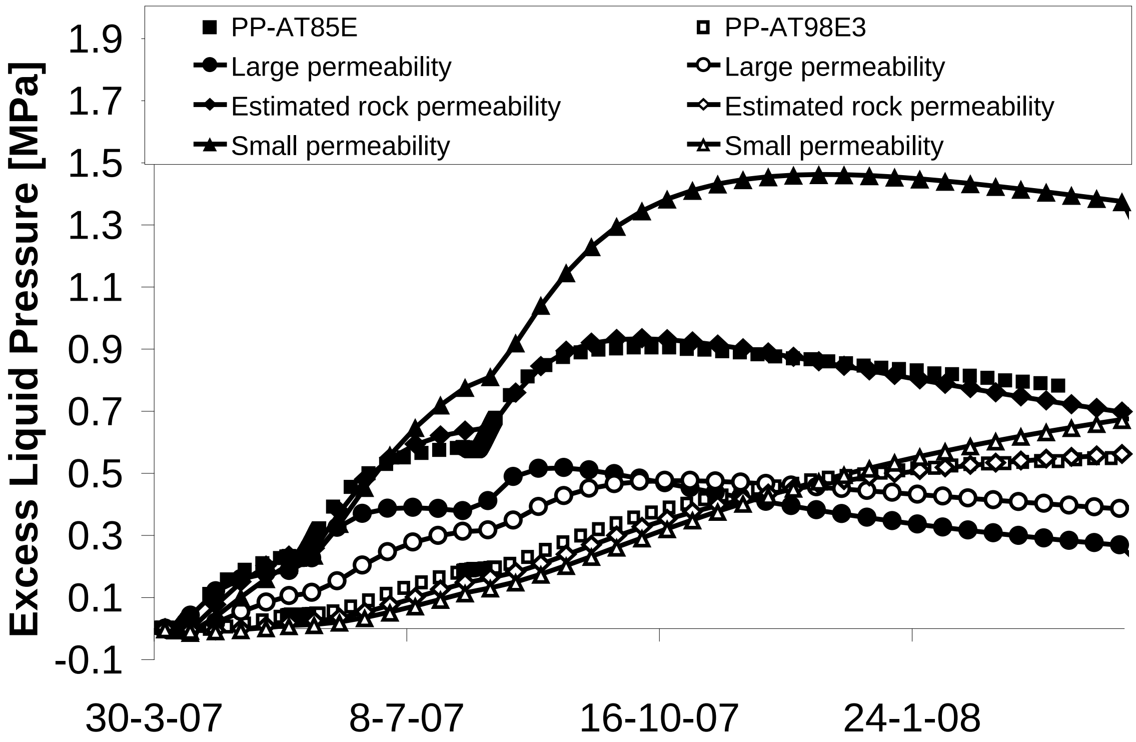

Figure 112: Measured and simulated excess pore water pressure at 1.5m (PP-AT85E, filled symbols) and at 2.5m (PP-AT98E3, white symbols) in the ATLAS. The simulations were run for three different permeability values: 1) k//=4E-19m2, k┴=2E-19m2; 2) k//=1.3E-19m2, k┴=6.6E-20m2 and 3) k//=4.4E-20m2, k┴=2.2E-20m2

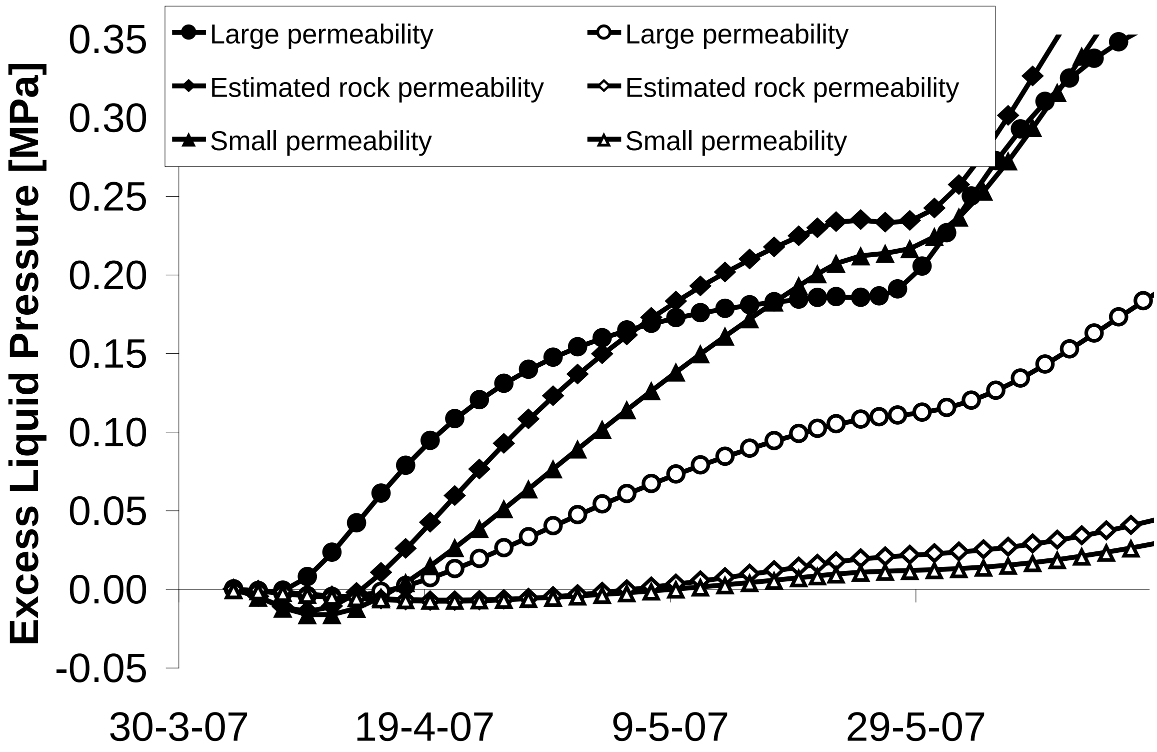

Figure 113: Measured and simulated excess pore water pressure at 1.5m (PP-AT85E, filled symbols) and at 2.5m (PP-AT98E3, white symbols) in the ATLAS. The simulations were run for three different permeability values: 1) k//=4E-19m2, k┴=2E-19m2; 2) k//=1.3E-19m2, k┴=6.6E-20m2 and 3) k//=4.4E-20m2, k┴=2.2E-20m2

11 References

[1] Knowles NC, Jeffries RM, Come B. Benchmarking the thermomechanical behaviour of clays—a progress report—the CEC interclay project. Engineering Geology 1996; 41(1-4): 65-71.

[2] Didier De B, Serge L. The second phase of ATLAS: the continuation of a running THM test in the HADES underground research facility at Mol. Engineering Geology 2002; 64 (2-3): 309-316.

[3] Bernier F, Neerdael B. Overview of in-situ thermomechanical experiments in clay: Concept, results and interpretation. Engineering Geology 1996; 41 (1-4): 51-64.

[4] Francois B., Laloui L., and Laurent C., 2009. Thermo-hydro-mechanical simulation of ATLAS in situ large scale test in Boom clay. Computers and Geotechnics, Vol. 36, pp 626-640.

[5] Bastiaens W, Bernier F, Li XL. An overview of long-term HM measurements around HADES URF. In: EUROCK 2006-Multiphysics Coupling and Long Term Behavior in Rock Mechanics, edited by Van Cotthem, Charlier, Thimus and Tshibangu, Taylor & Francis Group, London, ISBN 0415410010, 2006.

[6] Bernier F, Li XL, Verstricht J, Barnichon JD, Labiouse V, Bastiaen W, Palut JM, Slimane B, Ghoreychi K, Gaombalet M, Huertas J, Galera JM, Merrien K, Elorza, Davies FJ. CLIPEX: clay instrumentation programme for the extension of an Underground Research Laboratory. Luxembourg: Commission of the European Communities; 2002. EUR20619.

[7] Bernier F, Li XL, Bastiaens W. Twenty-five-years' geotechnical observation and testing in the tertiary Boom Clay formation. Geotechnique 2007; 57(2): 229-37.

[8] TIMODAZ. Thermal impact on the damaged zone around a radioactive waste disposal in clay host rocks. Deliverable 2. State of the art on THMC. Euratom European Project, 2007.

[9] Yang J: Pore pressure coefficient for soil and rock and its relation to compressive wave velocity, Geotechnique, 55 (3), 251-256, 2005.

[10] Yang J, Sato T. Interpretation of seismic vertical amplification observed at an array site. Bulletin of the Seismological Society of America 2000; 90(2): 275-285.

[11] Olivella, S., Carrera, J., Gens A., Alonso, E.E. 1994. Non-isothermal Multiphase Flow of Brine and Gas through Saline media.Transport in Porous Media, 15, 271-293.

[12] Bernier, F., Li, X.-L. & Bastiaens, W. (2007). Twenty-five years' geotechnical observation and testing in the Tertiary Boom Clay formation. Géotechnique 57, No. 2, 229–237.

[13] Garitte B., Sillen X., Ling X., Armand G., Vaunat J. and Gens A. 2009. Comparative study of three in-situ heating tests in anisotropic media: the HE-D, TER and ATLAS experiments. EC-TIMODAZ-THERESA THMC conference. Luxemburg.

[14] Gens, A., Vaunat, J., Garitte, B. and Wileveau, Y., 2007. In situ behaviour of a stiff layered clay subject to thermal loading. Observations and interpretation. Submitted to the Géotechnique Symposium in Print "Stiff Sedimentary Clays. Genesis and Engineering Behaviour".

[15] Garitte, B., Vaunat J., Gens, A., 2009. Determination of the thermal conductivity of the Callovo-Oxfordian clay stone in TER experiment. ANDRA report D.RP.0UPC.09.0002